DECAY OF La^{142}

DECAY OF La^{142}

by

WILLIAM VERNON PRESTWICH, B.Sc.

A Thesis
Submitted to the Faculty of Graduate Studies
in Partial Fulfilment of the Requirements
for the Degree
Doctor of Philosophy

McMaster University
August, 1963

DOCTOR OF PHILOSOPHY (1963)
(Physics)

McMASTER UNIVERSITY
Hamilton, Ontario

TITLE: Decay of La^{142}

AUTHOR: William Vernon Prestwich, B.Sc. (McMaster University)

SUPERVISOR: Dr. T. J. Kennett

NUMBER OF PAGES: ix, 129

SCOPE AND CONTENTS:

Techniques of beta- and gamma-ray scintillation spectroscopy have been applied to a study of the decay radiations from 92.6-min La^{142}. Several new gamma-ray transitions have been discovered and a gamma-gamma coincidence matrix has been established. Nine beta groups have been identified and evidence is presented substantiating the assignment of a first-forbidden unique character to the ground-state beta transition. Angular correlation studies have been performed on some of the gamma cascades. A decay-scheme based on the experimental results is discussed and some spin assignments are made. Some features of the decay modes are interpreted within the context of contemporary ideas about nuclear structure.

ACKNOWLEDGEMENTS

I wish to thank my Research Director, Dr. T. J. Kennett for his continual encouragement, advice and interest during the course of this work. In addition to his invaluable guidance, I would like to pay tribute to the stimulating enthusiasm with which he has directed this research. With patience and good humour he has demonstrated to me the challenges and traditions of experimental physics.

The completion of this work has been made possible by the aid and constructive criticism of the members of my Supervisory Committee, Dr. M. A. Preston and Dr. T. W. Hoffman, to whom I express my sincerest gratitude. In particular, I would like to thank Dr. Preston for an interesting discussion about a possible interpretation of the results.

I am indebted to Dr. K. Fritze for his many suggestions and his aid involving the preparation of sources. In addition, I would like to thank the members of the Reactor Staff for their co-operation in irradiating the many uranium samples required. Thanks are also extended to Dr. D. Burke for his help with the Gerholm spectrometer.

I would like to thank Miss P. Seigel for her patience and diligence in the face of what must have been a most exasperating task, the preparation of the manuscript.

This work has been supported financially by the National Research Council of Canada.

TABLE OF CONTENTS

LIST OF TABLES

LIST OF ILLUSTRATIONS

CHAPTER I

INTRODUCTION

1.1 Decay-Scheme Studies

The study of the disintegration modes of radioactive nuclei leads to information about nuclear mass differences, nuclear eigenstates and matrix elements. Such information is necessary for an understanding of the structure and behaviour of nuclei. The gross properties of the nucleus, the energy, spin and parity of each quantum state are relatively insensitive to the detailed nature of the associated wave function.

The mass of a nucleus is given by the sum of the masses of the individual nucleons plus the binding energy correction. It is this last term which depends specifically upon the nuclear structure. An unstable nucleonic configuration has a decreased binding energy and may be considered in some respects as an excited state of the stable configuration. From this point of view, a given configuration $A = Z + N$ is described as a system of A nucleons, Z of which are in the proton state and N of which are in the neutron state. The ground state configuration (Z_A, N_A) corresponds to that population of proton and neutron states for which the total mass or energy of the system is a minimum. In this context, configurations (Z,N) are excited states of the isobaric system of mass-number A. By the use of semi-empirical mass formulae, it is possible to describe the energies of these isobaric states as a function of the relative populations (Z,N). The form of this function is based upon a simplified model of nuclear structure. The parameters of the function are determined from experimentally observed masses and energy differences. The decay of an excited isobaric state requires a change in the configuration to one which represents a lower energy state of the system. In those cases for which the energy of the excited state is insufficient for the emission of one or more nucleons, leptonic emission occurs. For neutron-rich nuclides $(N \gg N_A)$ the leptonic decay mode corresponds to the emission of a negatron and anti-neutrino and can be described by $(Z_i, N_i) \longrightarrow (Z_i + 1, N_i - 1)$. Similarly, neutron-deficient isotopes decay by the competing modes of positron emission and electron capture. These processes are commonly referred to as beta decay.

The total disintegration energy Q_β is equal to the difference in energy between the initial and final configurations. These two states correspond to adjacent isobars and are referred to as parent and daughter nuclei. Therefore Q_β is equal to the difference between the binding energies of the parent and daughter nuclei.

A given nucleonic configuration can, of course, exist in any one of several quantum states, each corresponding to a different dynamic structure of the system with energy E_i referred to the ground state of the configuration. Except in the relatively rare case of delayed-neutron emission, the quantum states populated as a result of beta decay are bound states. These states de-excite by the emission of electromagnetic radiation, referred to as gamma radiation in this energy range. When the final state of a beta transition is an excited state of the daughter nucleus of energy E_i, the energy of the beta transition is $E_{\beta_i} = Q_\beta - E_i$. This energy is shared between the negatron and anti-neutrino in the form of kinetic energy. The kinetic energy of each lepton is distributed over the range extending from zero to the maximum, or end-point, energy E_{β_i}. The measurement of the end-point energy of the negatron distribution therefore leads to information about the Q_β value and the energy of the final state.

The beta-decay process directly populates only selected excited states of the daughter nucleus. The transition probability depends upon the change in spin and parity between the initial and final states and the energy of the transitions, as well as upon the detailed structure of the states. The transition probability increases approximately as $E_{\beta_i}^5$. For the same energy the transition probability is highest for allowed transitions defined by a change in spin of 0 or 1 and no change in parity. The next most probable transitions are those for which the change in spin is two or less and there is a change in parity. These transitions are referred to as first forbidden. The experimental parameter which is closely related to the transition probability is the comparative half life, denoted by ft. The comparative half life is the partial half life of the transition corrected for the energy dependence and varies inversely with the square of the lepton matrix element. The observed comparative half lives are distributed over a wide range of values. Generally, the ft values for allowed transitions occur within the range $10^3 - 10^6$, while the ft values for first forbidden transitions extend from $10^7 - 10^9$. If the ground-state spin of the parent nucleus is I, then one expects that the spin of a state populated directly in the decay will lie within the range I ± 2.

Because the lepton interaction is weak, the absolute values of the matrix elements are small and the life time of an excited isobaric state is extremely long compared to the life times of states which de-excite through electromagnetic or nuclear interactions. Of course, the life times extend over a wide range - half lives extending from a few seconds to many millions of years have been observed. In comparison, the life times of the bound excited states of a given nucleus generally lie in the range $10^{-12} - 10^{-8}$ sec. A given isobar therefore normally assumes its ground state configuration before leptonic de-excitation to the daughter nucleus.

Electromagnetic transitions between excited states of a given nucleus occur with energy and angular momentum equal to the difference between the energies and spins of the initial and final states. When the parity of both states is the same, the transition is electric for photons of even angular momenta and magnetic for photons of odd angular momenta. For transitions involving a change of parity, the converse is true. For a transition of multipolarity l and energy E_γ taking place between initial and final states of energy and spin (E_i, J_i) and (E_f, J_f) respectively

$$E_\gamma = E_i - E_f \quad \text{and} \quad |J_i - J_f| \leqq l \leqq |J_i + J_f| \ .$$

The transition probability varies as E_γ^{2l+1} and generally decreases rapidly with multipolarity. For this reason, in most cases the prominent de-excitation mode corresponds to the gamma radiation of lowest multipolarity. Since the transition probability involves the matrix element of the interaction Hamiltonian, it is extremely sensitive to the detailed structure of the eigenstates and departures from this trend are not uncommon. In order to determine the absolute value of the transition probability, it is necessary to measure the life time of the initial state and the branching ratios for each competing de-excitation mode. The relative transition probabilities for these modes may be calculated from the branching ratios alone. Transition probabilities are normally compared to the single particle estimates of Weisskopf (1). Wilkinson (2) has surveyed the distribution of the empirical values for all the observed transitions up to multipolarity E5. For the higher multipolarities the data are sparse. Generally, the distribution for a given type of transition is extremely wide, exceeding a range of five orders of magnitude. This wide distribution reflects the sensitivity of the transition probability to the details of the specific nuclear structure.

Information about the spins of excited states and the multipolarity of the transitions between them may be obtained by a study of the angular correlation between radiations emitted in cascade. Consider the three levels of spins J_i, J and J_f respectively. The transition $J_i \longrightarrow J$ will consist almost exclusively of, at the most, the two multipolarities $L_1 = |J_i - J|$ and $L_1' = L_1 + 1$. Similarly, the transition $J \longrightarrow J_f$ will consist of the multipolarities $L_2 = |J - J_f|$ and $L_2' = L_2 + 1$. The cascade is denoted by

$$J_i(L_1, L_1')J(L_2, L_2')J_f.$$

The calculation of the angular correlation function for such a cascade is reviewed by Biedenharn (3) who shows that

$$W(\theta) = \sum_{\nu} A_\nu(1)A_\nu(2)P_\nu(\cos\theta)$$

where θ is the angle between the directions of the radiations. The coefficients are given by

$$A_\nu(r) = F_\nu(L_r, L_r, J_r J) + 2\delta_r F_\nu(L_r, L_r', J_r J) + \delta_r^2 F_\nu(L_r', L_r', J_r J).$$

The F_ν's are combinations of angular momentum coupling coefficients and are tabulated (4). The mixing coefficient δ_r is the ratio of the reduced matrix elements $(J_r \| L'_r \| J)/(J_r \| L_r \| J)$. The mixing coefficient obviously depends sensitively upon the nature of the eigenstates involved.

1.2 General Properties of Fission Products

Unstable nucleonic configurations are usually obtained as the products of a nuclear reaction. The fission of heavy nuclei is a nuclear reaction which is prolific in the production of highly unstable, neutron-rich isotopes. The production of a particular fission product of mass number A and configuration (Z,N) is followed by a series of beta decays until a stable configuration (Z_A, N_A) is reached. The system of isobars related by such a series is referred to as a mass chain. For odd A nuclei, the energy of a particular configuration is approximately proportional to $(Z - Z_A)^2$ and lies on a parabola* when plotted as a function of Z. The energy difference between successive members of an odd-mass chain increases as the values of Z depart from Z_A. In the case of even-A mass chains, the odd-odd and even-even members lie on separate parabolas displaced by a relatively constant value. The energy differences between adjacent isobars alternate between high and low values according as the parent nucleus is odd-odd or even-even respectively. This alternation is superimposed upon the general trend of increasing energy differences as the value of Z departs from the most stable value. The existing data on energy differences has been analyzed on this basis recently by Dewdney (5).

---

*A more detailed examination reveals that the even-odd and odd-even masses lie on separate, closely-spaced parabolas.

This over-all trend has two important results. Since the transition probability for beta decay increases with disintegration energy, the half life of the isobar generally decreases rapidly as the configuration departs from stability. Secondly, the greater the disintegration energy, the greater the energy of the excited states in the daughter nucleus which may be populated. The number of de-excitation modes possible increases rapidly with the number of levels formed, so that the experimentalist is faced with the compounding difficulties of an increased complexity of the spectra of characteristic radiations together with a shorter time in which to study them.

1.3 Dynamics of Spherical Nuclei

A complete description of the quantum states of nuclei involves the solution of the equations of motion of a many-body Fermion system. In considering the interaction between nucleons in the nucleus it is generally assumed that this interaction may be described as a two-body force. The behaviour of nucleons under the influence of the inter-nucleon interaction within the nucleus is drastically altered from their behaviour under the same interaction when they are isolated. Weisskopf (6) has shown that the nuclear force has the property that the probability for scattering in which momentum transfers exceed the Fermi momentum is low. It is within this context that the internucleon interaction has been referred to as "weak". Since the eigenstates of the individual nucleons below the Fermi level are occupied, the Pauli exclusion principle forbids scatterings in which momentum transfers less than the Fermi momentum occur. For such systems it has been shown (6) that an independent particle description is approximately valid.

Brueckner (7) has shown that the internucleon interaction manifests itself mainly as an average self-consistent field for infinite nuclear matter and has performed Hartree-Fock type calculations of the field for finite nuclei (8). As has been pointed out by Wilkinson (9) in the low-density region near the nuclear surface, the Pauli principle is not as effective in suppressing strong correlations so that it is possible that in the surface region nucleon clusters are continually forming and dissolving. However, the success of the unified model does indicate that a self-consistent field in which the nucleons move independently is a description with some justification. In particular, the eigenstates of the Hamiltonian based on such a potential should provide a good basis of representation for the actual nuclear states - good in the sense that an actual quantum state will be distributed over only a small number of the basic set. The calculations of Brueckner et al (8) show that the eigenstates of the self-consistent field for finite nuclei are not unlike those for the shell model potential with spin-orbit coupling.

There is a large body of experimental facts which indicate that an independent particle field does not completely describe the effects of the nucleon-nucleon interactions. The nucleon motions are correlated to a certain degree so that the nucleus should be pictured as a many-body system of interacting Fermions moving in a self-consistent field. The effects of the internucleon force not taken into account by the self-consistent field are described by a residual interaction. It is fair to say that one of the main tasks before us is to obtain a description of the detailed nature of the residual interactions.

Pines (10) has defined a many-body system of Fermions for which the interactions can be treated by perturbation theory as a normal Fermion system. A comparison of the experimental evidence with the general properties of such systems leads to the conclusion that the nucleus is not a normal Fermion system. This comparison also indicates the nature of that part of the residual interaction which cannot be treated by perturbation theory. As an example, it is a well-known fact that the values of the nuclear inertial parameters lie between the extremes predicted on the basis of rigid body motion and irrotational fluid hydrodynamics. General arguments (11) show that the former value is equal to that of a normal Fermion system, while the latter corresponds to that for a system of non-interacting Bosons. Such a situation can be understood if the nucleus is pictured as a superfluid condensate in which the Boson unit is a quasi-bound Fermion pair. Such systems were investigated theoretically by Bardeen et al (12) who showed that the spectrum of intrinsic excitations is characterized by an energy gap. Bohr, Mottelson and Pines (13) pointed out that such a gap exists in even-even nuclei. In addition, the nuclear masses do exhibit odd-even effects which can be explained as reflecting the increased binding energy due to pairing correlations. The pairing force also provides a fundamental basis for the seniority coupling introduced by Racah (14). The ground-state wave functions corresponding to the bound pairs are of zero spin so that the wave function represents a spherical distribution.

Several mass regions, such as the one corresponding to the heavy rare earths, have been positively shown to consist of nuclei with permanent ground state deformations. In terms of the unified model, the deformation is thought of as resulting from the polarizing influence of the extra nucleons outside of the spherical core corresponding to a major closed shell. The systematics of deformations indicates that a collective deformation does not occur until a critical number of extra-core nucleons is present. This effect is explained in terms of the microscopic description formulated by Mottelson (15). The residual interaction is considered to manifest itself in two distinct forms - the pairing correlation and a field-aligning, long-range correlation. The long-range components of the residual interaction are described by a multipole expansion, the first and largest term of which represents a quadrupole-quadrupole interaction. These two aspects of the residual interaction result in opposing tendencies. The pairing force stabilizes the spherical equilibrium while the quadrupole interaction tends to deform the nucleus. Deformation occurs at the critical number of extra-core nucleons for which the effects of the quadrupole interaction overcome the pairing force.

In the spherical region, the independent particle states are described as states with definite orbital angular momentum and spin coupled to a total angular momentum j, of degeneracy $(2j+1)$. Major closed shells, which are configurations of exceptionally high stability, occur for the special nucleon numbers 2,20,50,82 and 126 (16). If there were no residual interactions between the nucleons, the nucleus would be similar to a Fermi gas and the distribution of nucleons in the particle states would drop sharply to zero at the highest level required to accommodate the nucleons. In this case a well-defined Fermi surface occurs. However, at low energies the nucleus is in the superfluid state and the effect of the pairing correlations is to disturb the distribution. In the treatment of Belyaev (17) the pairing interaction is assumed to be non-zero only between the conjugate orbitals (j,m) and (j,-m). The effect of this correlation is to cause the nucleon distribution to become diffuse in the region of the Fermi surface.

The distribution coefficients for conjugate pairs (j ±m) is given by

$$V_j^2 = \frac{1}{2}\left[1 - \frac{E_j - \lambda}{\sqrt{(E_j - \lambda)^2 + \Delta^2}}\right]$$

where λ is the Fermi level, Δ is the pair binding and E_j is the energy of the single-particle orbital (17). In an even-even nucleus, for which the ground state has zero seniority, the intrinsic excitations occur at an energy of at least 2Δ above the ground state.

The remainder of the residual interaction manifests itself in collective motions. For a spherical equilibrium shape, the collective motions take the form of vibrations about this shape. The lowest energy vibrations correspond to quadrupole oscillations and the next lowest energy vibrations correspond to octupole vibrations. The vibrational quanta, referred to as phonons, are of even parity and angular momentum 2 for quadrupole oscillations, and odd parity and angular momentum 3 for octupole vibrations. Particle-vibration interactions result from the vibrations of the self-consistent field caused by the collective oscillations. If the particle motions adjust adiabatically to the changes in the field, the intrinsic and collective motions are separable. However, if the vibrational energies are of the same order of magnitude as the intrinsic excitation energies, the adiabatic conditions are no longer fulfilled and the motions become coupled. Collective levels are characterized by enhanced electric moments with the appropriate multipolarity corresponding to the vibrational mode in question.

According to Brown (18) and Mottelson (15) the microscopic description of nuclei indicates the existence of high-energy collective modes of a unique character. With increasing excitation energy, the effects of the pairing correlation become less significant and in many respects the nucleus behaves as a normal Fermion system. This is reflected in the fact that at high energies the inertial parameters agree more closely with the rigid-body values and the nuclear specific heat is similar in behaviour to that of a Fermi gas.

It is known that in distorted nuclei the normal sequence of a rotation band is disrupted abruptly at an angular momentum sufficiently high that the Coriolis interaction exceeds the pair binding (19). It might be expected that a similar effect occurs in a vibrational band as the particle-vibration interaction increases.

Those nucleonic configurations for which there are only a few extra-core nucleons so that no permanent ground state deformation exists comprise what is referred to as transition nuclei. The systematics of the vibrational levels of transition nuclei has been reviewed by Sheline (20). The high-yield fission products generally are such transition nuclei so that the study of their level structure leads to much-needed additional information about this region.

CHAPTER II

SURVEY OF PREVIOUS WORK

Hahn and Strassmann (21) first reported the existence of a 74-minute lanthanum activity observed in their extensive and extremely thorough radiochemical investigations of the fission products. One cannot but express sincere admiration for these investigations which represent a classic example to experimental science. Values for the half life of this activity have been reported by several researchers (22,23,24,25) extending between this initial value to the most recent measurement of 92.6 minutes (25). In all cases, no daughter activity was observed. The mass assignment of $A = 142$ is based on this fact. Beta decay of lanthanum ($Z = 57$) leads to an isotope of cerium ($Z = 58$). The only stable cerium isotopes are Ce^{140} and Ce^{142}, the latter occurring in nature with an isotopic abundance of 11% (26). The lanthanum precursor of Ce^{140} was positively identified as a 40-hour activity (27).

Riezler and Kauw (28) have reported that Ce^{142} decays by the emission of a 1.5 MeV alpha particle with a half life of $5.1 \begin{smallmatrix} +\ 5.1 \\ -\ 2.5 \end{smallmatrix} \times 10^{15}$ years. Another possible decay mode for Ce^{142} is double beta decay to Nd^{142}. The energy difference between these two isobars has been measured by Johnson and Nier (29) who report a value of 1.68 MeV. The neutron separation energy for Ce^{142} has been measured using the reaction Ce^{142} (γ, n) to be 6.91 MeV (30).

The first study of the decay radiations of La^{142} published in the literature were undertaken by Vanden Bosch (31). This author reported the beta spectrum to be complex and to have an end-point energy greater than 2.5 MeV. These results were obtained by aluminum absorption methods. This author also reported the existence of two gamma rays with energies 0.63 and 0.87 MeV.

Ryde and Herrlander (23) were the first researchers to investigate the gamma-ray spectrum and gamma-gamma coincidence relations for the La^{142} decay. They reported the existence of eight gamma rays in the energy range from 0.63 to 3.4 MeV and observed the spectra in coincidence with pulses corresponding to the energies of four of these. The results are shown in Table I. On the basis of these results, the authors constructed a decay scheme consisting of levels at 0.63, 1.5, 2.4 and 3.5 MeV.

In 1959 a study of the barium and lanthanum isotopes, masses 141 and 142, was published by Schuman et al (24). These authors investigated the decay radiations of La^{142} and their gamma-gamma coincidence matrix. On the basis of their results, they concluded that two additional levels in Ce^{142} at 2.57 and 3.30 MeV were populated in the decay. The results are summarized in Table II. In Figure 1 is shown the known information about the decay properties of the mass 142 isobars as summarised by the Nuclear Data Group (32).

TABLE I

Energies and Coincidence Relationships of the Gamma Rays in La^{142} Reported by Ryde and Herrlander (23)

E_γ (MeV)	Gating Energy (MeV)			
	0.63	0.87	2.4	2.9
0.63		x		x
0.87	x			
1.0	x	x		
1.8	x			
2.0	x	x		
2.4				
2.9	x			
3.4				

TABLE II

Results of Schuman et al (24)

E_γ (keV)	Gating Energy (keV)							
	640*	900	1030	1920	2080	2400	2550	3000
640 ± 10		x	x	(x)	x		x	x
900 ± 10	x				(x)			
1030 ± 30	x							
1080 ± 40			x					
1370 ± 30	(x)							
1540 ± 20								
1750 ± 20								
1920 ± 20	(x)							
2080 ± 30	(x)							
2400 ± 20								
2570 ± 30								
2660 ± 100	x							
3000 ± 30	x							
3300 ± 30								
3650 ± 30								

$E_{\beta_{max}} = 4.4$ MeV

---

[*] Coincidences for which the authors indicated some doubt are bracketed. In addition, the authors observed coincidences between the 640 keV gate and transitions at 1200 and 1580 keV which they consider tentative.

Level Scheme for A = 142 Cs, Ba, La, Ce, Pr, Nd, Pm, and Sm

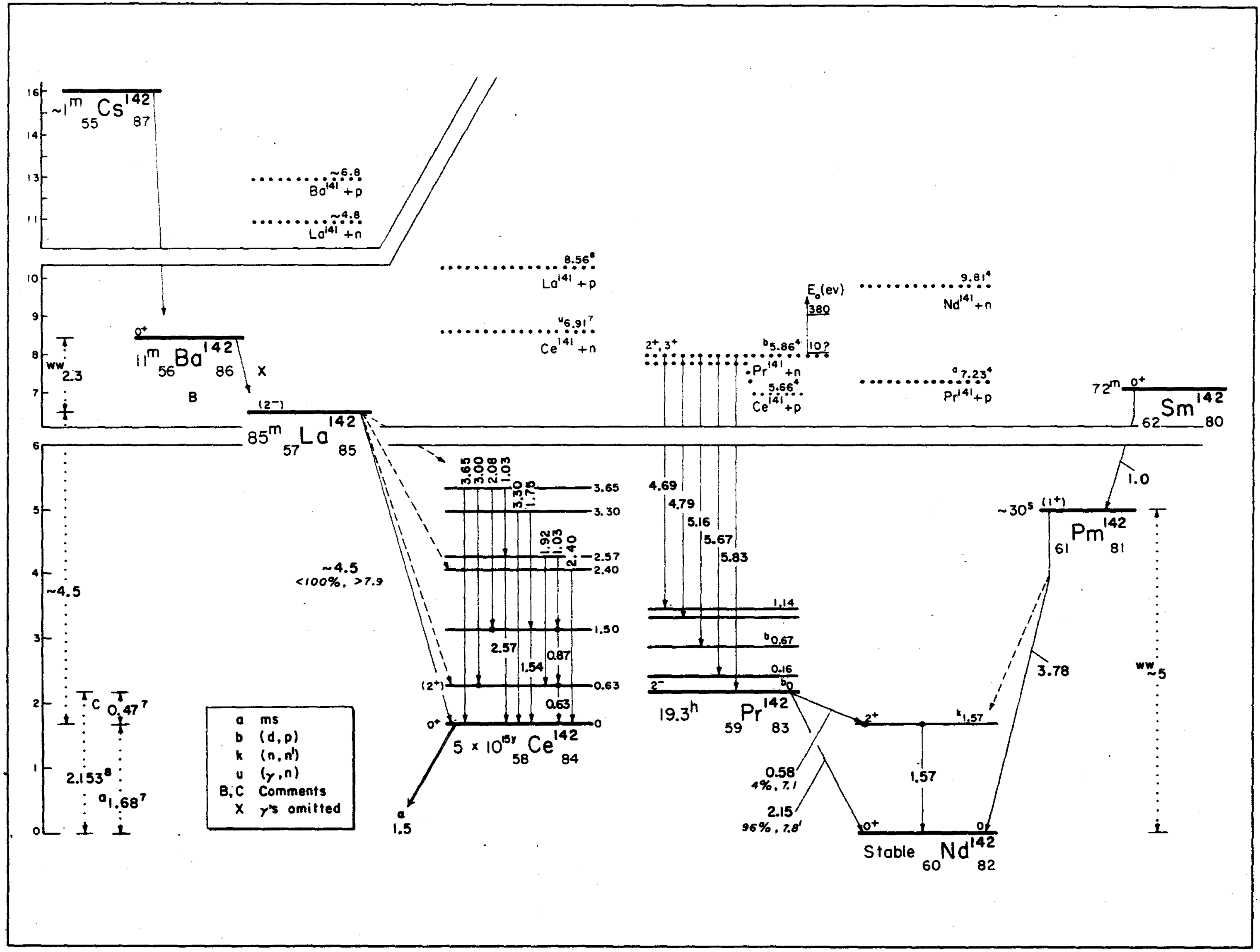

FIGURE 1

Level Scheme A = 142

16a.

CHAPTER III

SOURCE PREPARATION

3.1 Introduction

In order to prepare a source consisting of a short-lived isotope produced by fission, rapid radiochemical separation techniques may be used. The methods selected must fulfill rather stringent requirements. The time required for the separation must not be excessively long with respect to the half life of the nuclide of interest. If a detailed examination of the decay radiations is to be undertaken, the separation must result in a sample with a high degree of radiochemical purity. In many instances, such as in the study of low-energy beta spectra, very thin sources may be required. Of course, because of the limitation of time available for the separation, it is not always possible to fulfill these requirements.

The chemical behaviour of elements in trace concentrations is often quite different from that displayed in macroscopic quantities. In order to ensure that separation procedures developed using normal concentrations may be extended successfully to a problem involving trace concentrations, it is often necessary to add macroscopic quantities of the elements involved to the radioactive sample. These inactive quantities added to ensure macroscopic behaviour are referred to as carriers. Carriers are normally added to the sample in the form of ions. The chemical exchange between the radioactive and carrier atoms may not be complete, especially if there is a possibility that the valency state of the radioactive ions is different from that of the carrier ions.

Generally speaking, of the various chemical separation procedures used, group precipitations and solvent extractions are most easily adapted to rapid radiochemical separations. Normally, carrier is added to the sample in solution before precipitation. However, recent studies (33) indicate that in certain circumstances there are advantages to adding the sample to pre-precipitated carrier. In this case, one relies upon the exchange between sample and carrier occurring in the crystals of the precipitate. It has been found (25,33,34) that this method is more selective, reducing exchange between the carrier and radioelements of different species.

3.2 Application of Radiochemical Techniques to the Separation of Fission Products

When developing a procedure for the separation of a fission product, the properties of the decay chain in which the nuclide of interest occurs, as well as of neighbouring chains, must be taken into account. Since, of course, chemical techniques only result in elemental separations, the sample obtained may contain many isotopes of the element, interference from which precludes a study of the isotope of interest. By an appropriate use of the timing of the separation, and in some cases by separating precursors of the isotopes in question, it is sometimes possible to eliminate serious interference. In addition, separation of the precursor may require simpler procedures than direct separation of the element involved.

The problem of obtaining sources of La^{142} is a good illustration of the principles discussed above. The relevant decay chains are:

$$\begin{aligned}
&Cs^{140} \xrightarrow{\text{66 s}} Ba^{140} \xrightarrow{\text{12 d}} La^{140} \xrightarrow{\text{40 hr}} Ce^{140}\\
&Cs^{141} \xrightarrow{\text{25 s}} Ba^{141} \xrightarrow{\text{18 m}} La^{141} \xrightarrow{\text{3.7 hr}} Ce^{141}\\
&Cs^{142} \xrightarrow{\text{2.3 s}} Ba^{142} \xrightarrow{\text{11 m}} La^{142} \xrightarrow{\text{92.6 m}} Ce^{142}\\
&Cs^{143} \xrightarrow{\text{short}} Ba^{143} \xrightarrow{\text{12 s}} La^{143} \xrightarrow{\text{14 m}} Ce^{143} \xrightarrow{\text{33 hr}}
\end{aligned}$$

A direct separation of lanthanum from the fission products would require a gross separation of rare earths followed by an ion-exchange separation of lanthanum. The resulting sample would contain independently formed La^{140}, La^{141}, La^{142} and La^{143}. In order to obtain the sample free from the most active of these, La^{143}, a waiting period of approximately 2 1/2 hours would be required. Such a waiting period is undesirable since the ratio of La^{142} activity to that of the longer lived isotopes reduces with time.

There are distinct advantages to separating the barium precursor as the first step. If barium is separated approximately 2 minutes after the end of the irradiation, the sample will be free from isotopes of mass number greater than 142. For maximum yield, the lanthanum must be extracted from the barium solution after approximately 40 minutes when the La^{142} has fully grown in. The sample will contain La^{141} as the only interfering isotope. Fortunately, the nature of the La^{141} decay is such as to cause no serious problems as regards interference in the study of La^{142} (24).

3.3 Preparation of La^{142} Samples

Uranium samples consisting of 100 - 300 μgm of U^{235} in 3 ml uranyl-nitrate solutions were irradiated in polyethylene capsules for 1 to 4 minutes using the pneumatic system of the McMaster Nuclear Reactor. The flux at this position is $\sim 3 \times 10^{12}$ neutrons/cm^2 sec. The sample was delivered to the receiving station approximately 10 seconds after the end of the irradiation.

The initial step of the procedure, carried out 2 minutes after the end of the irradiation, was the separation of radiobarium from the gross fission products. The radiobarium was exchanged with 50 mgm of barium carrier in the form of freshly pre-precipitated barium chloride in 30 ml of concentrated HCl. The solution was filtered over a membrane filter and the precipitate washed with 30 ml of concentrated HCl. The precipitate was then dissolved in approximately 15 ml of water. From this point on, one of two methods was used to separate radiolanthanum from the barium solution.

Method 1: Since the most likely contaminant to be carried along with the fission-product barium is strontium, the precursor of yttrium, a lanthanum-yttrium separation using a tributyl-phosphate solvent extraction was used. Ten mgm of lanthanum carrier in the form of $La(NO_3)_2$ solution was added to the barium sample. Approximately 40 minutes after the end of the irradiation, lanthanum hydroxide was precipitated and the precipitate centrifuged. The precipitate was dissolved in fuming HNO_3 and the solution agitated together with 10 ml of freshly pre-equilibrated tributyl phosphate. Lanthanum was withdrawn in the acid phase into fresh TBP and the extraction repeated. Ammonium hydroxide was added slowly to the solution until lanthanum hydroxide precipitated. The hydroxide precipitate was re-dissolved in a few milliliters of concentrated HNO_3. The sample was obtained in its final form by precipitating lanthanum oxalate. The physical form of sources obtained in this procedure was a relatively uniform disc of lanthanum oxalate 1/2 inch in diameter backed by filter paper.

Method 2: The method described above resulted in lanthanum separations with a radiochemical decontamination factor of at least 10^6. However, the total time required for the separation was approximately 1 1/2 hours. Also, the source thickness of 10 mgm/cm^2 was considered relatively thick in some applications. For these reasons, a method resulting in a carrier-free sample a few minutes after the beginning of the lanthanum separation was investigated and proved highly satisfactory. Following the $BaCl_2$ exchange reaction, concentrated ammonium hydroxide was added to the solution without the addition of lanthanum carrier. When passed over a membrane filter, the radiolanthanum was found to be retained on the filter, presumably in the form of a colloid. It is not known whether the source forms a surface layer or is impregnated throughout the filter. In the latter case, the source thickness would be that of the filter paper, approximately 3 mgm/cm^2.

3.4 Source Purity

Although the second method produces carrier-free sources simply and rapidly, decontamination from yttrium relies solely on the fact that negligible amounts of strontium are carried in the barium chloride exchange (25). Decay curves of sources made by the second method revealed only the existence of half-life components corresponding to

La^{142} and La^{141}. The decay curve of the gamma radiation is shown in Figure 2. Decay curves of the beta-gamma and gamma-gamma coincidence rates also shown in Figure 2 revealed only the 92.6-minute La^{142} (25) component. A comparison of the single-crystal gamma-ray spectra of sources obtained with both methods indicated that they were identical. Because of these results it was concluded that sources obtained using the second method were sufficiently pure for the purposes of this study. As a matter of general procedure, decay curves were taken during each experiment.

LANTHANUM DECAY CURVES

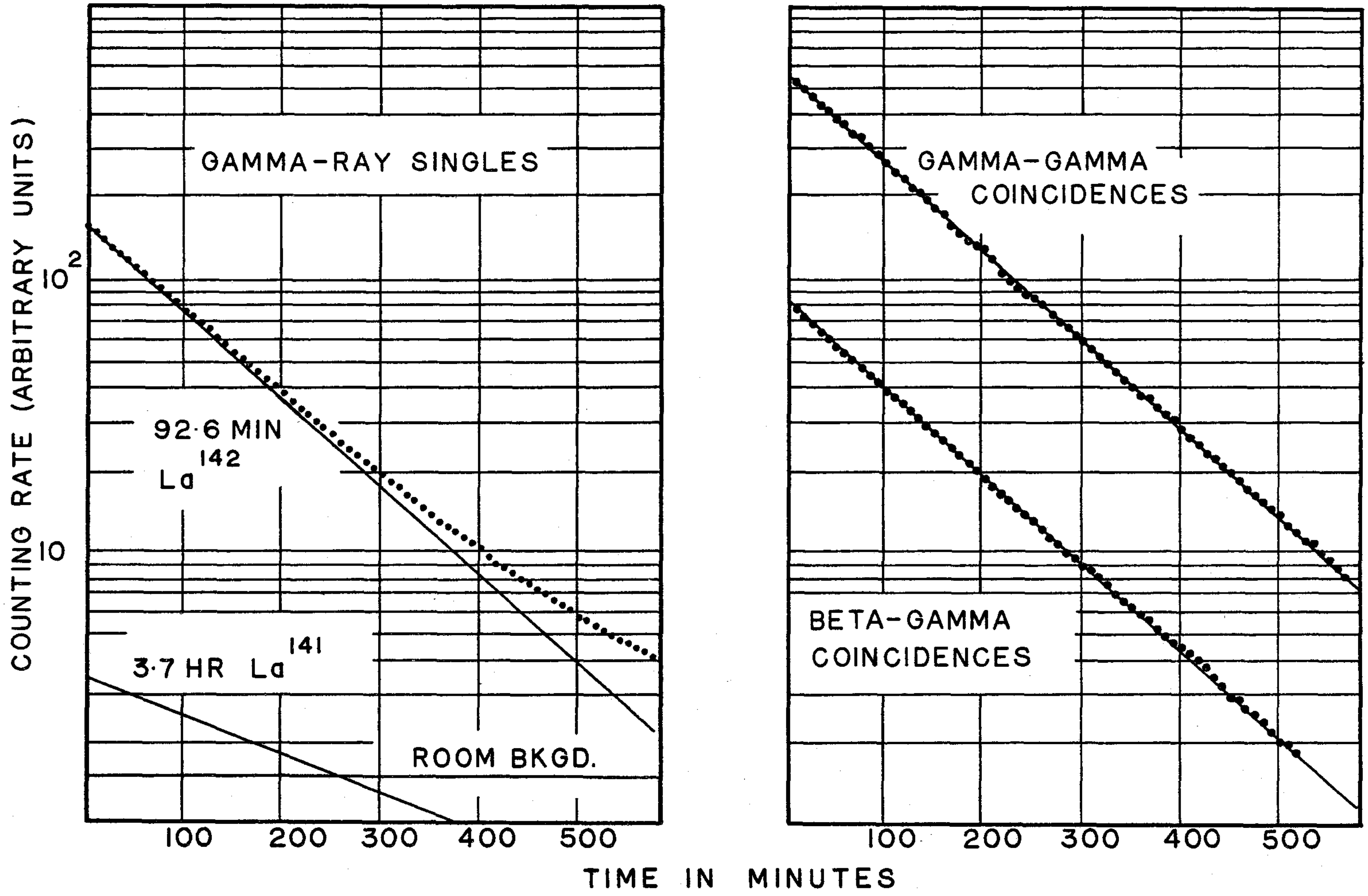

FIGURE 2

CHAPTER IV

INSTRUMENTATION AND TECHNIQUES

4.1 Scintillation Detectors

The detection of nuclear radiations with luminescent materials optically coupled to photomultiplier tubes relies on the nearly proportional transfer of the incident energy into light quanta which are not reabsorbed by the material itself. The details of the transfer mechanism depends on the nature of the interactions between the radiations involved and the detecting scintillator. The most popular scintillator used for the detection of gamma radiation is NaI activated with thallium. A plastic phosphor, referred to as NE-102* is frequently used for the detection of beta particles. In either case, the result of the interaction of the radiation with the scintillator is the excitation of electronic levels such as luminescence centers in the scintillator and the subsequent emission of light photons as de-excitation radiation. De-excitation of the phosphor electron states also takes place by the competing process of radiationless transitions, which reduce the light output of the detector. The number of photons emitted is proportional to the energy transferred to the scintillator and the emission occurs at a rate characteristic of the scintillator. The decay time for NaI(Tl) is approximately 0.25 μsec while for the

---

*NE-102 is a scintillating phosphor commercially available from Nuclear Enterprises Limited

NE-102 the emission occurs with the much shorter period of roughly 10^{-8} sec.

The light photons collected at the photocathode of the photomultiplier tube cause the emission of electrons, the number of which depends upon the nature of the cathode surface but is proportional to the number of incident light photons. The electrons emitted from the photocathode are multiplied in a cascade of secondary emission processes in the dynode chain of the tube. The resultant photomultiplier current is integrated at the anode and the total charge collected is proportional to the initial light intensity at the photocathode. Conversion to a voltage pulse suitable for amplification is frequently achieved with a charge sensitive preamplifier. The rise time of the pulse is determined mainly by the decay time of the scintillator in the case of NaI(Tl), while in the case of the plastic phosphor the effect of the photomultiplier transit time becomes equally important.

In the scintillation detection method, the height of the voltage pulses resulting from the detection of radiation is used as a measure of the energy of the radiation deposited in the detector. However, any given pulse represents only a statistical sampling of the events which give rise to the pulse so that there is associated with the pulse height a statistical uncertainty or variance. In statistical processes, the relative uncertainty is decreased as the size of the sample is increased. The best resolution is achieved therefore by obtaining the maximum pulse height possible under given conditions. This is accomplished by full integration of the photomultiplier current using a time constant several times as large as the scintillator decay constant. Assuming an exponential input pulse with rise time equal to the characteristic scintillator decay constant, and ideal response from the network, then the ratio of pulse height achieved to maximum pulse height is given by

$$R = \begin{cases} n \exp \dfrac{n \ln n}{1 - n} & \text{for} \quad n \neq 1 \\ 0.36 & \quad\quad n = 1 \end{cases}$$

where n = RC/T is the ratio of the circuit time constant to the scintillator decay time T. Since the pulse width also increases with the time constant, in practice a value is chosen which is a compromise between the desire for large but narrow pulses. Another criterion for this value will be mentioned later.

Another deterious effect of using too short a time constant at the photomultiplier anode is the decrease in signal-to-noise ratio. This limitation is not serious in the case of scintillation detectors except for extremely short clipping times because of the rather low inherent resolution of these detectors.

The signal-to-noise ratio can be maximized by an appropriate choice of photomultiplier voltage. However, the choice of voltage to be used also depends upon other considerations. If, as in our case, pulse spectra are to be studied over an energy range as wide as approximately 100 keV to 4000 keV, then the dynamic range required for the phototube is 100, a figure which includes a customary safety margin. At voltages sufficient to maximize the signal-to-noise ratio, the linear dynamic range is decreased because of saturation effects in the phototube.

In addition to considerations of dynamic range, another effect which is particularly noticeable in many of the three-inch phototubes currently available must be taken into account. This is the dependence of photomultiplier gain on counting rate. The details of this dependence varies with tubes from different manufacturers and has been studied by several researchers (35,36,37). The relative counting-rate gain shifts increase with photomultiplier voltage (37), so that this effect is minimized by using the lowest voltage possible consistent with the requirements of gain and signal-to-noise ratio. Except in special circumstances, the standard voltage adopted here for the DuMont 6363 phototubes used in the gamma-ray spectrometers was 750 V. The two-inch EMI 9536B photomultipliers used in the beta-ray detectors were found to be relatively free of counting-rate gain shifts and a voltage of 900 V was required because of the poorer light output of the NE-102 phosphor compared to NaI(Tl).

4.2 Double-Delay Line Amplifiers

The pulses obtained directly from the photomultiplier output are not suitable for pulse-height measurements so that they must be shaped and amplified before analysis. As described in Section 1, it is necessary to satisfy the conflicting requirements of high signal-to-noise ratio and relatively narrow pulse widths. In addition, when the main concern is the measurement of pulse height, a pulse which retains its maximum for a time which is appreciable with respect to the pulse width is desirable. Pulse widths presently required for analysis are in the ranges of 1 - 2 μsec.

Delay-line shaping provides the most accurate control of pulse widths while at the same time producing pulses which are more symmetrical and "flatter" than the pulses shaped with resistance-capacitance networks. The shorted end delay-line clipping which is commonly used in, for example the Bell, Graham, Petch (38) method for producing very narrow timing pulses, can result in troublesome ringing in a linear amplifier. The operational amplifier, which subtracts the delayed pulse from the prompt pulse in an active network is an alternative method which overcomes this limitation.

If the pulse is clipped at the input stage of the amplifier then the signal-to-noise ratio is reduced, while if the clipping stage is left until after amplification, pulses of long duration must be handled by the amplifying stages. In the latter case, the response of the amplifier is limited by pile-up effects at relatively low counting rates. Fairstein (39) proposed a compromise solution to this problem in which two clipping stages are used, one at the input and one near the output. The pulse shape resulting from this method is bipolar and has several characteristics which can be used to advantage in pulse spectroscopy. The equal balance of the positive and negative portions of the pulse eliminates the base-line shift which occurs noticeably at high counting rates in amplifiers with unipolar pulse shaping. The double-delay line, or DD2 amplifier is also characterized by rapid recovery from overload, so that pulse-height distribution in a low-energy range may be studied in the presence of high-energy radiations without undue amplifier blocking.

The transistorized version of the DD2 amplifier, designed by Chase (40) was used in this counting system. An oscillograph of the pulse spectrum of Cs^{137} obtained at the amplifier output is shown in Figure 3 (a). In order to obtain the best quality pulses, the time constant used in the integration of the photomultiplier pulse should be kept long with respect to the delay-line clipping time of 0.7 μsec. Time constants of 10 μsec were used.

4.3 Pulse-Height Analysis

Technically, the aim of pulse spectrometry is to obtain a statistically significant sample of the pulse-height distribution associated with the detector response to the radiation characterizing a particular excitation or de-excitation process. To achieve this aim, it is necessary to sort the amplified detector pulses according to height and record the relative frequency of occurrence of a given incremental pulse-height range.

By coupling an upper- and lower-level discriminator in anti-coincidence the familiar single-channel pulse-height analyzer is obtained which gives a logic pulse output in response to any input pulse, the height of which lies in the range defined by the discriminator levels. To obtain a measure of the pulse-height distribution, it is necessary to scan the pulse spectrum in steps, counting the number of pulses at each setting for a suitable time interval. When, as frequently occurs, it is necessary to count for a time interval comparable to the half-life of the source, this method is no longer feasible.

To obtain detailed structure of the pulse-height distributions associated with the decay radiations of short-lived nuclides, rapid data acquisition systems become a basic necessity. Such systems have

FIGURE 3

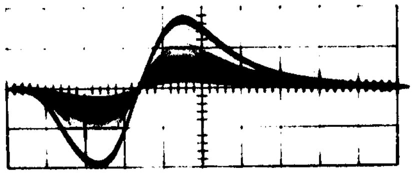

(a) DD2 Amplifier Output for Cs^{137} Scintillation Spectrum. Time Scale 0.25 usec./cm

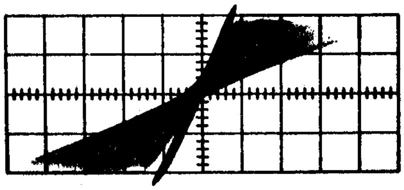

(b) Cross Over Region of Pulse Spectrum in (a). Time Scale 20 nsec./cm

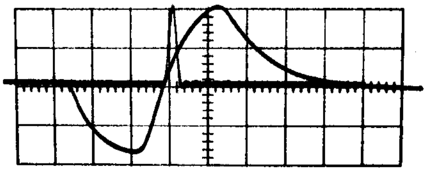

(c) Cross Over Gate Timing Marker. The DD2 Amplifier Pulse is also Shown for Comparison. Time Scale 0.35 usec./cm

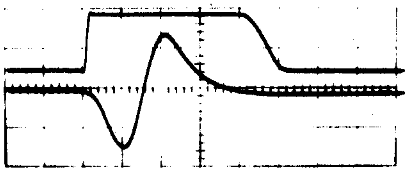

(d) Analyzer Enable Gate and DD2 Amplifier Input to the ADC. Time Scale 0.5 usec./cm been achieved by the application of computer logic techniques. The multichannel analyzer is a specialized computer designed to sort and accumulate detector pulses according to height so that a measure of the pulse-height distribution as a whole is obtained in one counting period. This approach is only useful when the method of detection is such that a pulse spectrum results with the desired information associated with the pulse height. If the information to be sorted is associated with some other property, such as pulse width, or radius of curvature in a magnetic field, then this property must either be translated into pulse height or a different sorting procedure must be adopted.

The multichannel pulse-height analyzer is comprised of the main functional units shown in Figure 4. Since the initial pulse-height distribution to be analyzed is continuous over a certain voltage range, it is necessary to group the pulses into quantized adjacent incremental voltage ranges in order that they may be sorted and accumulated in a memory of finite capacity. Using a triggered linear sweep or ramp circuit, the height of a given pulse is proportionally converted to a time interval. The time interval is measured in a digital manner by using an accurately controlled high-frequency oscillator, or clock. This process is known as analogue-to-digital conversion. The number of clock pulses during the time interval is determined by counting with the address scaler. In this way, the pulses in a certain voltage range are grouped together and associated with a definite address or channel, so that the initial continuous distribution is quantized.

After a channel number has been associated with an input event, the previous contents of the memory at that address are increased by

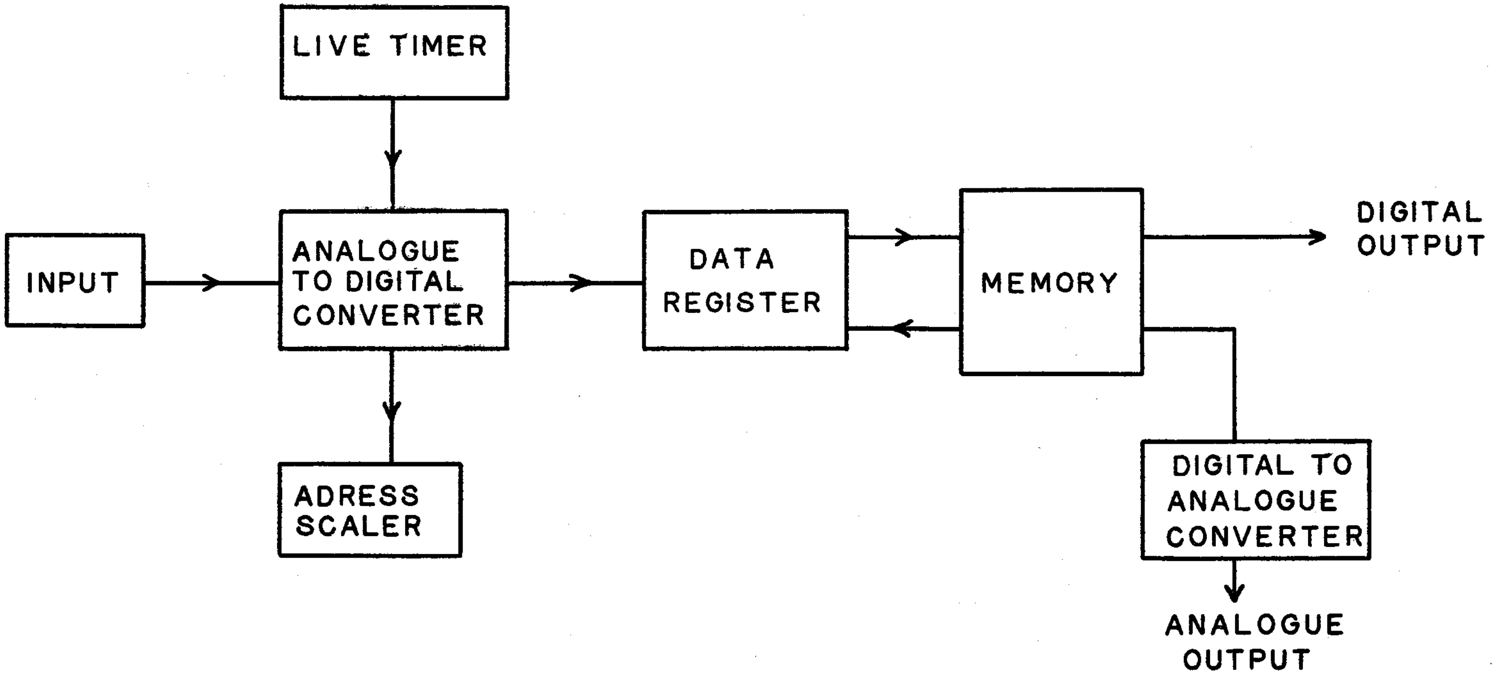

MULTICHANNEL ANALYZER

FIGURE 4

one in the accumulator, or data register. The contents of the data register are then restored in the memory location in question. This process of reading the previous contents of an address, increasing by one, and restoring is known as a memory cycle.

The pulses resulting from the decay radiations of an ensemble of radioactive nuclei are distributed randomly in time. In order that only one pulse occurs in the converter circuit during analysis, the analogue-to-digital conversion (ADC) circuit is preceeded by a linear gate. The gate closes during the analysis time required for the pulse already in the converter and opens when the analysis is completed.

Since the time required for analysis depends upon the address assigned to the pulse, the overall dead time for a particular counting experiment depends upon the nature of the spectrum involved. The actual live time of the analyzer during a given counting period is measured by scaling a clock oscillator. The scaling of the clock pulses is inhibited during those periods for which the analyzer is busy.

The response characteristics of the analyzer are determined mainly by the performance of the analogue-to-digital converter. The integral linearity, a measure of the linearity of the pulse-height channel-number relation, is determined by the quality of the ramp circuit. The stability of the analyzer depends upon the stability of the ramp, the oscillator and the associated gating circuits. The differential linearity is a measure of the constancy of the channel width. If a distribution is analyzed with the property that the counting rate is independent of pulse height then the counts per channel is inversely proportional to the channel width. A pulse generator was used to measure the linearity, and the profile of individual channels. The channel profile is shown in Figure 5. In addition, the generator can be used to determine accurately the channel corresponding to zero pulse height. The zero channel can be adjusted to correspond to any pulse height desired.

Many situations arise, such as in coincidence experiments, in which it is necessary to measure the pulse-height distribution of a subset of events defined by conditions additional to those necessary for the occurrence of the total set. The subset of events may be selected for analysis from the total set by gating the analyzer with suitable logic pulses which signify the occurrence of events satisfying the selective condition. The gating pulse enables the analysis of these events, while events unaccompanied by such a pulse are rejected.

Several pulse-height distributions corresponding to subsets selected by different conditions may be analyzed in one counting period. By reducing the conversion gain of the ADC ramp circuit by a factor N, the analyzer memory may be divided into N subgroups. Those events belonging to a given subset are directed to the appropriate memory subgroup by means of accompanying routing pulses. The routing pulses are derived from logic circuits which only respond to events satisfying the conditions selecting the corresponding subset.

4.4 Coincidence Circuit

In the application of pulse spectroscopy to decay-scheme studies, it is often necessary to obtain the pulse-height distributions of time-correlated events. These events must be sensed in separate detectors and a measure of their time separation obtained. Logic AND

FIGURE 5

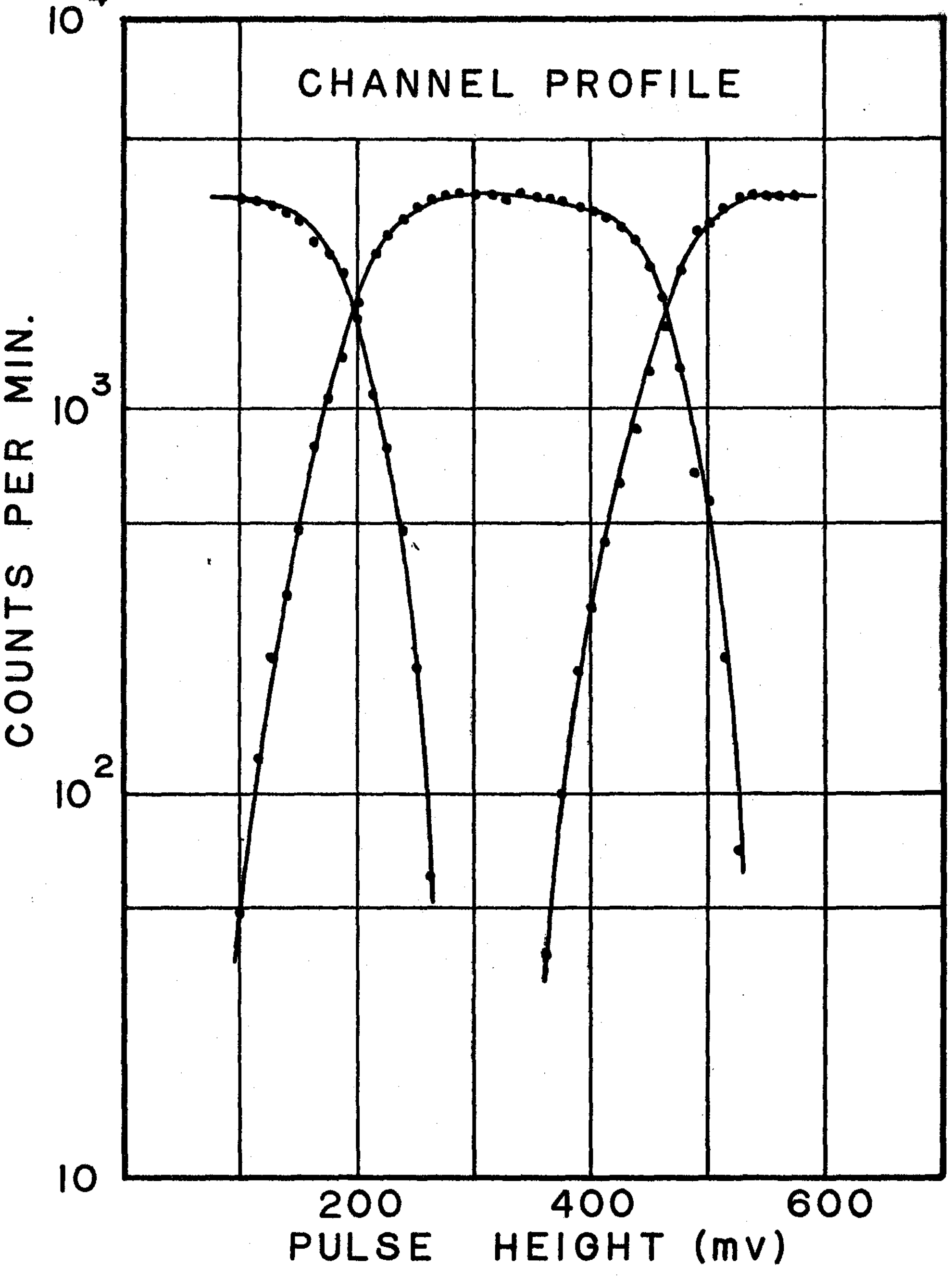
CHANNEL PROFILE
COUNTS PER MIN.
10^4
10^3
10^2
10
200
400
600
PULSE HEIGHT (mv)

circuits are used to signal the occurrence of a pair of correlated events. It is necessary to form timing marker pulses based on the detector signals as inputs to the AND circuit. Very fast timing circuits have been developed in which the timing markers are formed by clipping limited pulses obtained directly from the detectors (38). Usually, to obtain pulses of sufficient rise time and pulse height for this approach, it is necessary to operate the photomultipliers at voltage levels which are undesirably high for pulse spectroscopy. In addition, the time dispersion of three-inch photomultipliers together with the long decay time of NaI(Tl) become the limiting factors in ultimate resolution rather than the timing circuit.

Fast timing based on marker pulses derived from the slow amplifier pulses must overcome the problem of walk. This term refers to the amplitude dependence of the timing signal caused by the finite rise time of the generating pulse. Since the triggering level of any discriminator must be of some finite value exceeding the noise, say Δ, then the triggering time is approximately

$$t = \frac{\Delta}{V} \ t_r,$$

where V is the pulse amplitude and t_r is the rise time of the generating pulse. With a fixed pulse amplitude, it is found that the triggering time is still statistically distributed because of fluctuations in the pulse shape. This effect is known as jitter. One solution to the problem of walk is to confine the energies of interest to a narrow range by pulse-height selection. However, this results in a drastic reduction in the rate of data acquisition. The method is used frequently in life-time measurements but is of little use in the study of pulse-height distributions.

Amplitude-independent timing markers may be generated by triggering on a phase point of the generating signal which is independent of pulse height. The cross-over point of the DD2 amplifier output pulses is such an amplitude-independent phase point as illustrated in Figure 3 (a). This fact was pointed out by Fairstein (41) who developed a circuit which generates a timing marker at the zero-voltage point of the doubly-differentiated pulse known as a cross-over gate. The walk and jitter associated with the cross-over phase point is shown in Figure 3 (b). The amplifier pulse serves as the input to a Schmitt-trigger circuit which triggers at an arbitrary level on the leading edge of the pulse and returns to its initial state at the zero or cross-over point. The Schmitt-trigger output is differentiated and the leading edge pulse is removed with a back-biased diode. The zero-point timing marker is shaped in a multivibrator of variable time duration.

To a good approximation, the resolving time of the entire system is determined by the width of the timing marker, so that the resolving time is variable. For the transistorized circuits designed by Chase (42) which were used in this study, the width of the timing marker could be varied between 0 and 180 nsec. The output of the AND circuit provides a 3 μsec coincidence gate. Oscillographs of the timing marker and coincidence gates are shown in Figure 3 (c) and (d). The response of the circuit was measured by counting the coincidence gates as a function of the relative delay between the timing markers. A region in which the counting rate is independent of delay indicates full efficiency for the circuit. The width of the curve at half maximum is 2τ, the resolving time of the circuit. Flat resolution curves were obtained for resolving times in excess of $2\tau = 50$ nsec. A typical resolution curve is shown in Figure 6.

4.5 Gamma-Ray Scintillation Spectrometer

The complete system comprising the scintillation detector, the linear amplifier and pulse-height analyzer constitutes a relatively simple and efficient gamma-ray spectrometer with comparatively low resolution. The characteristics of the spectrometer, in particular the rather complex response to monoenergetic radiation, is determined for the most part by the characteristics of the detector, although detailed examination must also take into consideration certain properties of the associated circuits. The factors affecting the overall features of the detector response may be divided into two categories; the properties of the energy-to-charge transfer mechanism and environmental effects.

The transfer mechanism is characterized by several distinct stages. In the first stage, the energy of the gamma radiation is transferred to electrons in the crystal by a combination of photoelectric, Compton scattering and pair producing events. The relative probabilities of the three interactions are energy dependent; for energies less than 0.1 MeV the photoelectric process is dominant but decreases rapidly so that at 0.5 MeV the Compton scattering process is the most probable result of an interaction. Above 1.02 MeV competition from pair production occurs and increases rapidly. At 5 MeV the cross section for pair production is approximately one half of that for Compton scattering. In the low-energy region for which the photoelectric effect is the dominant mode, the entire gamma-ray energy is

FIGURE 6

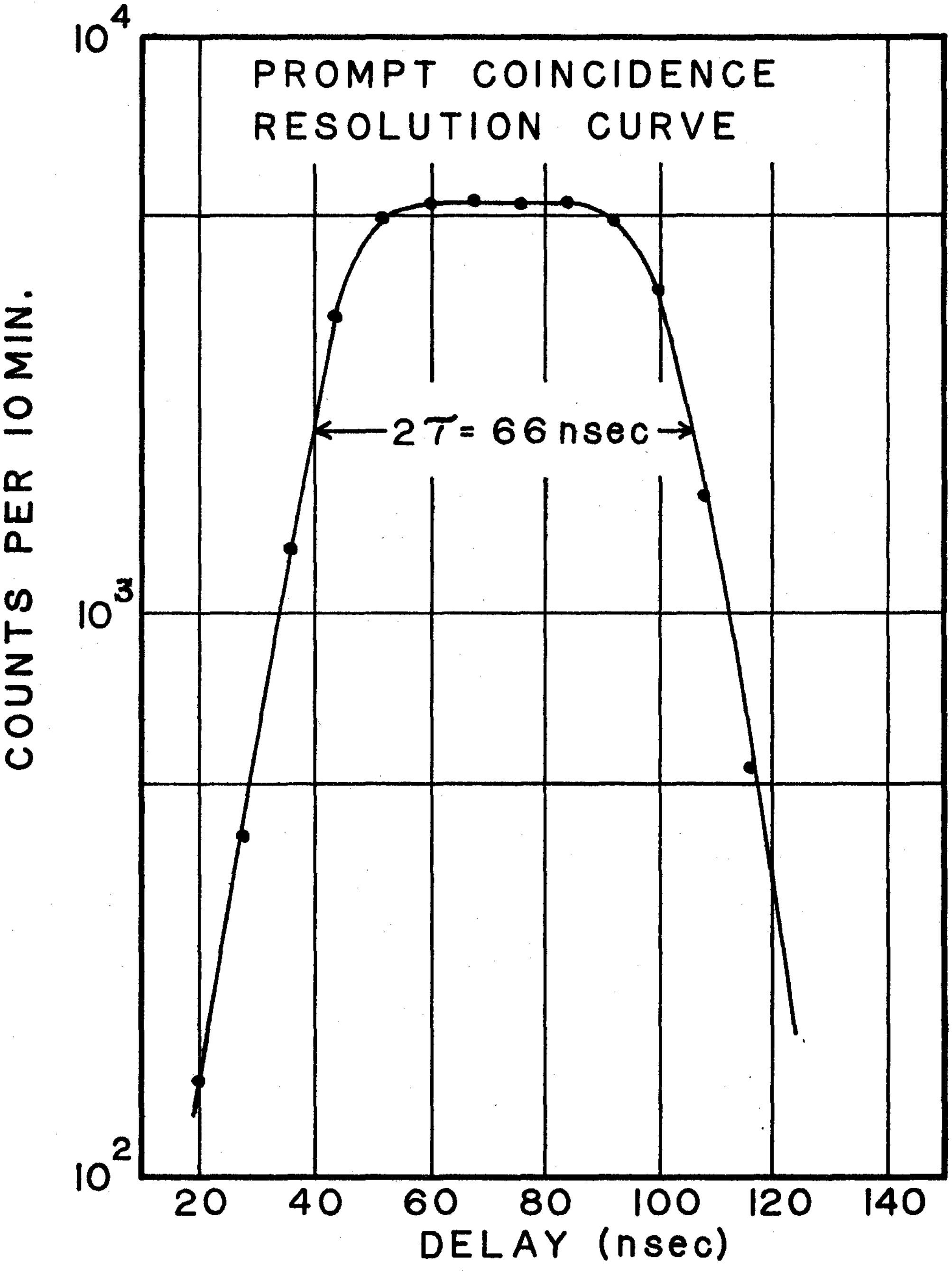
PROMPT COINCIDENCE
RESOLUTION CURVE
2τ = 66 nsec
COUNTS PER 10 MIN.
10^4
10^3
10^2
20
40
60
80
100
120
140
DELAY (nsec)

most frequently dissipated in a single event. Above this energy the fraction of multiple events which occur increases rapidly with energy, as does the probability for partial energy transfer in which not all the incident gamma-ray energy is dissipated in the crystal.

In the second stage, the electrons which have been energized by interaction with the gamma radiation excite crystal-lattice electron states and the process proceeds as described previously. In interpreting the features of the response function, it is important to realize that the pulse-height distribution which results reflects the energy distribution of the electrons produced in the gamma-ray interaction, rather than the much simpler energy distribution of the gamma rays themselves.

The response of the 3 x 3-inch NaI(Tl) detector to monoenergetic gamma rays is shown for several incident energies in Figure 7. The response is characterized by a full-energy peak, a continuous Compton distribution and at sufficiently high energies, pair-escape peaks. As can be seen from the figure, the relative contribution from these three components is energy-dependent. At a given incident energy and geometry, the partial-energy portions of the response decrease as the size of the detector is increased.

The nominal resolution of the spectrometer is taken as the relative width of the full-energy peak at one half the maximum height. In part, this parameter is related to the variance in the statistical distribution of the energy-to-charge conversion used in the detection process, so that the resolution improves with energy. In addition, however, there is found to be an intrinsic or "infinite energy" resolution.

FIGURE 7

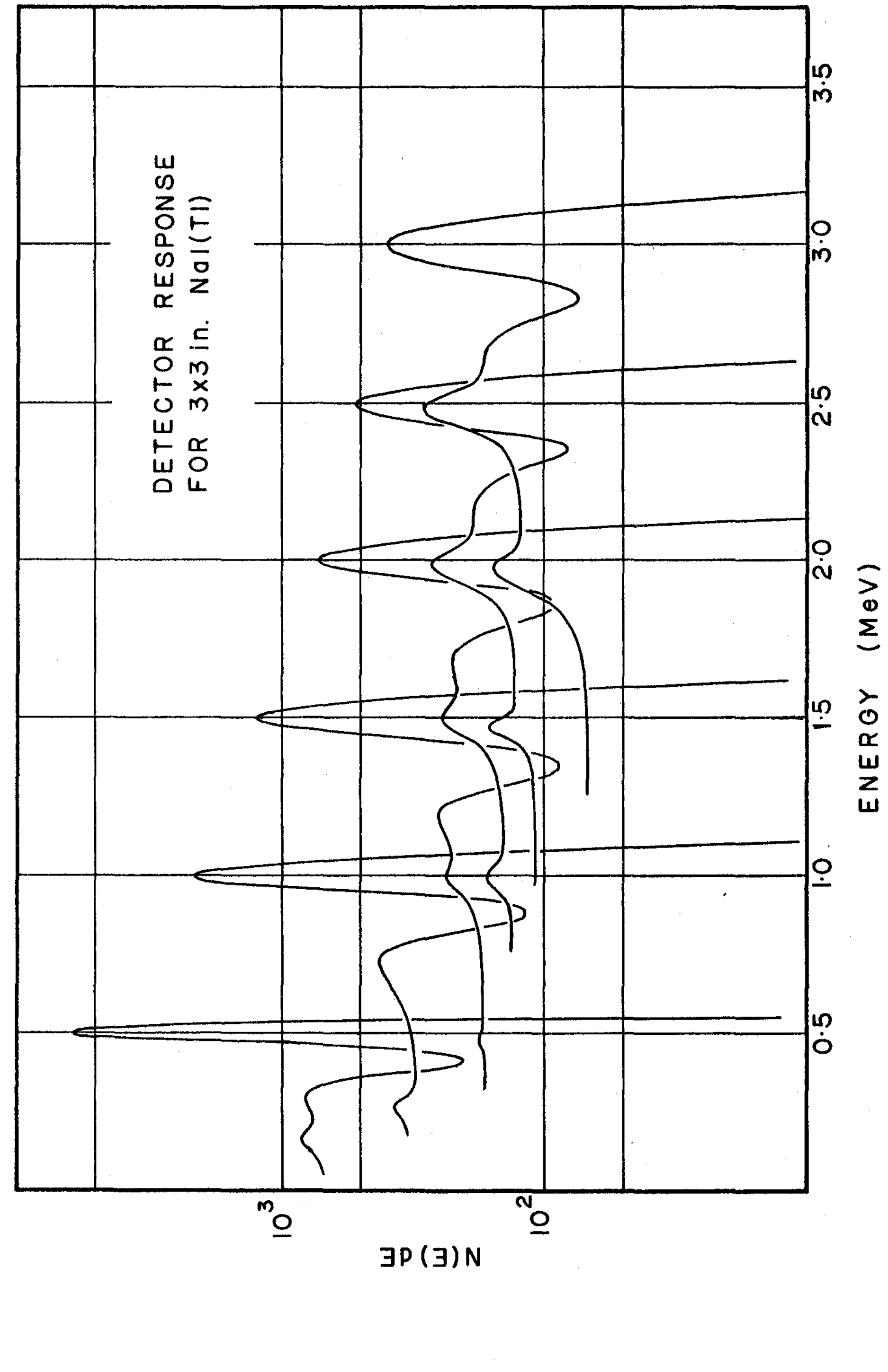
DETECTOR RESPONSE
FOR 3x3 in. NaI(Tl)
N(E) dE
10^3
10^2
ENERGY (MeV)
0·5
1·0
1·5
2·0
2·5
3·0
3·5

The position of the full-energy peak is taken as a measure of the incident energy. The relationship between the pulse height of the full-energy peak and the incident energy was investigated by measuring the pulse height per keV as a function of incident energy relative to the value for the 0.662-MeV gamma ray of Cs^{137}. The results are shown in Figure 8. The solid curve is a composite of the results of previous researchers (43,44,45) who investigated the low-energy region more thoroughly than in this study. The results obtained are in good agreement, and indicate that the relationship is not linear.

Certain features of the response are determined by such environmental factors as source-detector geometry and surroundings, source thickness, shielding and any absorbers interposed between the source and the detector. Large-angle scattering from shielding, source material and detector mounts give rise to the familiar back-scatter peak. Small-angle scattering which takes place in the absorber and the source material leads to photons only slightly degraded in energy. The detection of these photons decreases the peak-to-valley ratio. At sufficiently high energies, annihilation radiation is detected as a peak at 0.511 MeV and results from pair creation by high-energy gamma rays interacting with material other than that of the detector.

Another effect which can be considered as environmental is the detection of beta particles directly, or Bremsstrahlung which occurs when a charged particle is accelerated. High-energy beta radiation can be detected directly by NaI(Tl) counters packaged in thin aluminum. Electrons are stopped in a material by simple collisions and by the emission of Bremsstrahlung radiation. The ratio of radiative energy loss to loss by collisions is given approximately by

FIGURE 8

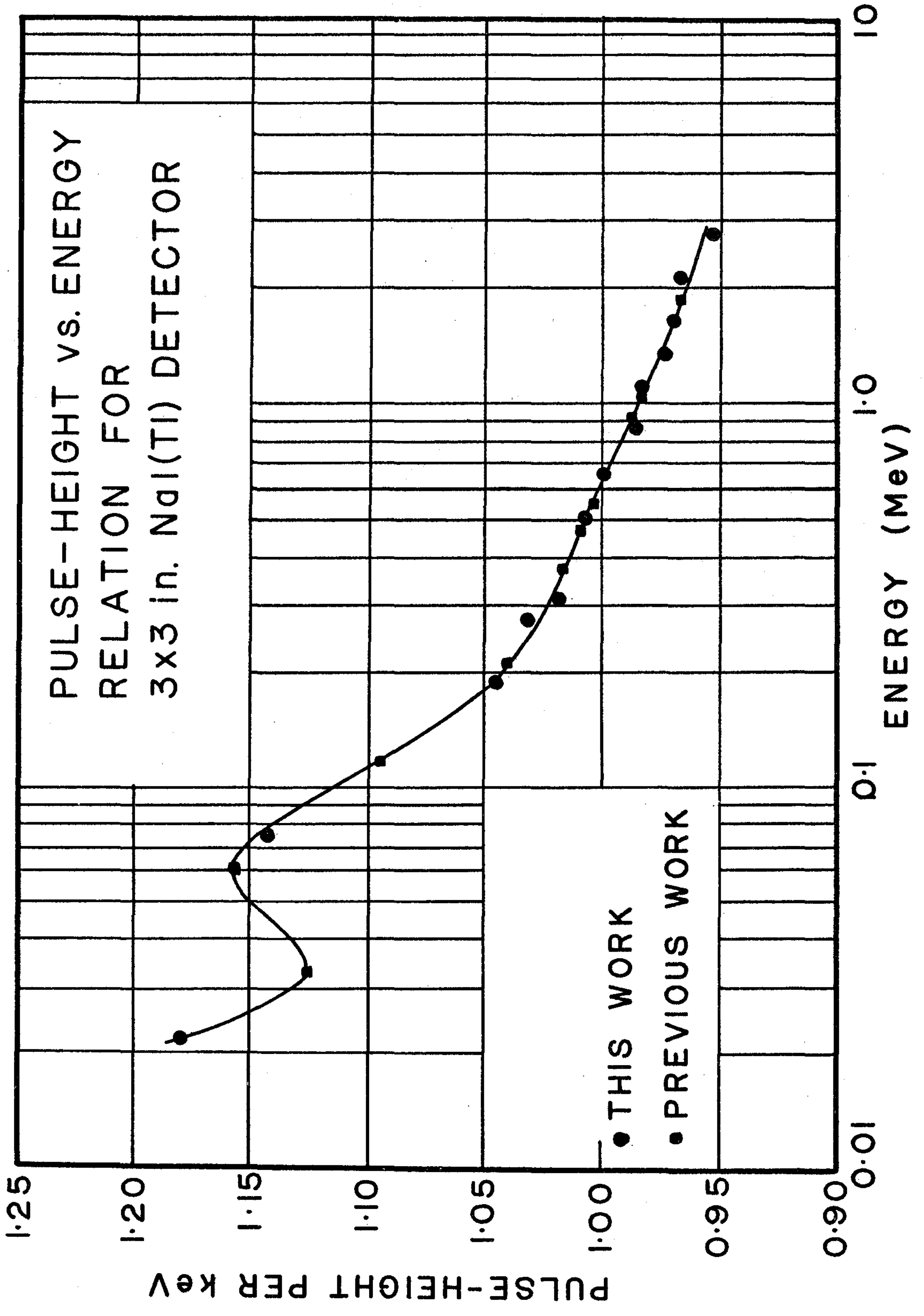
PULSE-HEIGHT vs. ENERGY
RELATION FOR
3x3 in. NaI(TI) DETECTOR
● THIS WORK
■ PREVIOUS WORK
PULSE-HEIGHT PER keV
1·25
1·20
1·15
1·10
1·05
1·00
0·95
0·90
0·01
0·1
1·0
10
ENERGY (MeV)

$$R = \frac{E_o Z}{800}$$

where E_o is the particle energy in MeV and Z is the atomic number of the stopping material. It can be seen that radiation losses can become significant when Z is large and E_o is in the energy range of 3 - 5 MeV. In order to keep Bremsstrahlung radiation levels at a minimum, polyethylene absorbers which have a low effective Z are used with the thickness selected so as to slightly exceed the range of the maximum energy beta particles encountered. In general, sources of minimum possible extraneous material are used. In the particular case of La^{142}, the carrier-free sources suited these conditions ideally.

In order to reduce the extraneous contributions from scattering as much as possible, it was decided to count with unshielded detectors. The counting room selected was the one available with the lowest background. At the source levels used, room background effects were not serious. Detector mounts were constructed of polyethylene and the counting was done on wooden benches, or in a lightly constructed aluminum frame.

Two remaining extraneous contributions to the scintillator response are connected with the fact that the energy selection is performed electronically. These contributions are referred to as coincidence summing and random summing. Coincidence summing refers to the detection of both members of a cascaded pair of gamma rays. Since the relative contribution from this effect depends upon the solid angle subtended, it is reduced by increasing the source-to-detector distance. Of course, this also results in an undesirable reduction in overall efficiency and in the ratio of desired events to room background. In the measurement of single-crystal gamma-ray spectra, a standard source-to-detector distance of 10 cm was found to be a satisfactory compromise.

Random summing is the detection of uncorrelated gamma rays by chance within the effective resolving time of the system. Since this contribution increases with counting rate, the minimum source strength required to obtain a statistically significant distribution was used. For the case of interest, it was found that the contribution from random summing was negligible when 2 - 3 μc sources were used. Methods for measuring the amount of summing contribution will be discussed in a later section.

4.6 Fast-Slow Coincidence Spectrometer

The fast-slow coincidence spectrometer enables the researcher to study the pulse-height distribution of events correlated in time with those events which satisfy a selected pulse-height condition. The logic arrangement used for this system is shown in Figure 9. The analyzer is enabled on the gate which only occurs when events detected in A and B are in fast coincidence and the event in B satisfies the pulse-height requirement set by the pulse-height selector. When this condition is satisfied, the event detected in A is sorted and accumulated in the multichannel analyzer. Since the timing marker is generated at the zero phase point of the amplifier output, it is necessary to delay the latter so that it arrives slightly after the coincidence enable gate. By using a two-speed system the uncertainty in pulse-height selection time may be tolerated while the advantage of faster timing is retained. This aspect is discussed thoroughly by

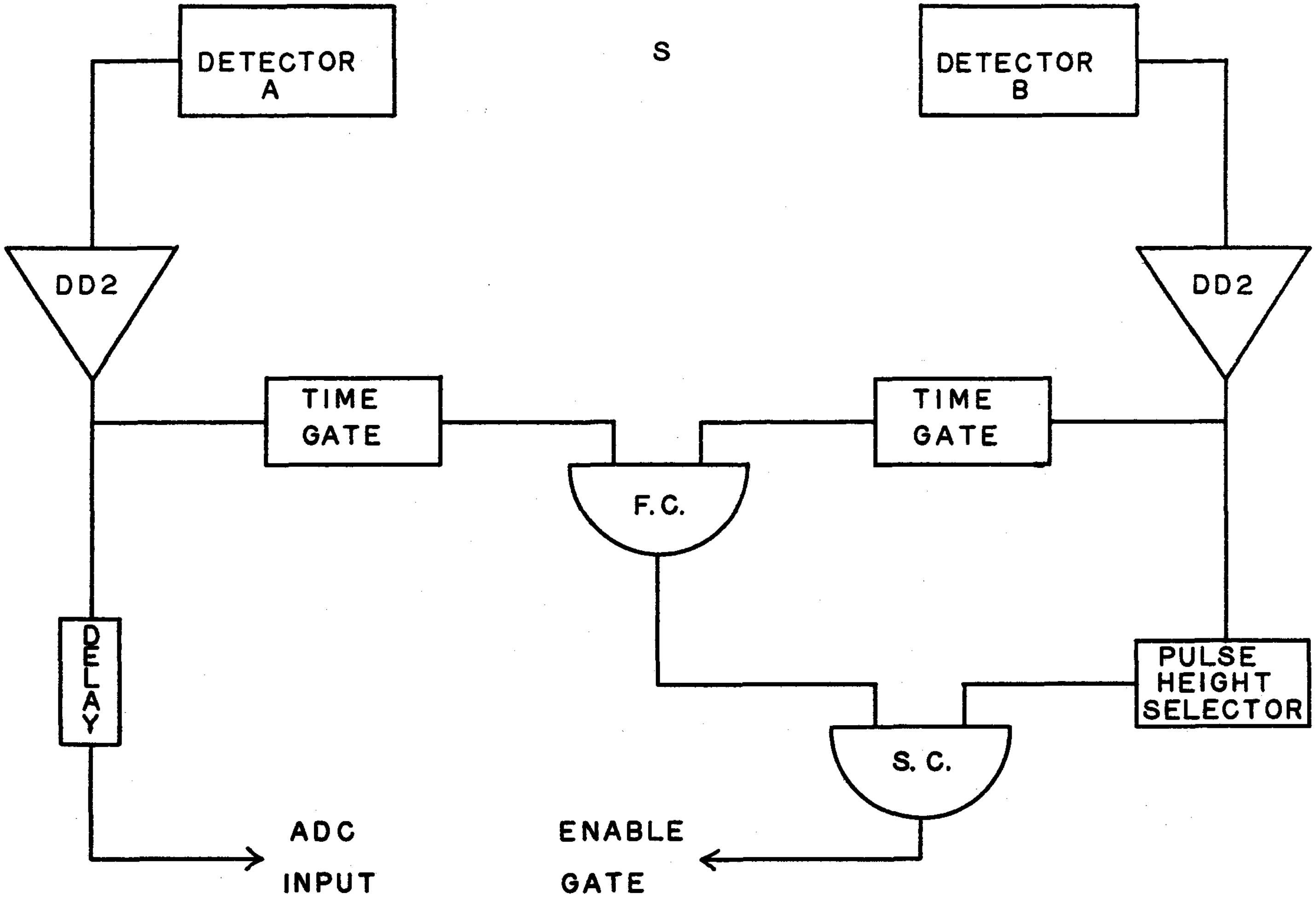

FAST-SLOW COINCIDENCE SYSTEM

FIGURE 9

several authors (41,46) who show that the overall resolving time of the system is the resolving time of the fast-coincidence circuit.

In the usual gamma-gamma coincidence experiment, a narrow window is set on the photopeak of the gamma ray of interest to be selected in side-channel B. In order that the detailed analysis of the results obtained be meaningful, it is necessary to determine accurately the position and width of the window. Because of counting-rate gain shifts and the possibility of long-term window drifts it is not usually sufficient to calibrate the pulse-height selector with standard sources. In dealing with short-lived isotopes, however, there is insufficient time available to find the window position by step-wise scanning of the spectrum of interest. This is particularly true when the spectrum involved consists of many photopeaks which cannot be readily identified when only a limited region of the spectrum is scanned.

The window width and position can be determined rapidly and accurately by self-gating the analyzer. The delayed output from the linear amplifier in side-channel B is connected to the analyzer which is enabled by gating with the output from the pulse-height selector. A single-crystal spectrum from detector B is obtained in one subgroup of the analyzer memory with the ADC unblocked. The gated spectrum, which only contains pulses satisfying the condition set by the pulse-height selector, is then obtained in a second subgroup. The position of the window with respect to the rest of the spectrum can be checked visually with an oscilloscope display of the overlapped subgroups. When the window has been adjusted satisfactorily a hard copy record of the memory contents is taken. The window position is checked again after the end of the coincidence counting.

Because the resolving time of the system is necessarily finite and the time distribution of unrelated events from an ensemble of decaying nuclides is random, not all pairs of events which give rise to a coincidence gate result from truly correlated events. Unrelated events which occur within the resolving time of the coincidence circuit are referred to as chance events. Since the ratio of chance events to true coincidence events is given by $2\tau N_o$, where τ is the circuit resolving time and N_o is the source strength, the chance contribution for a given resolving time is kept as small as possible by using the minimum source strength required for the experiment. It is possible to measure the chance contribution in a given experiment during the same counting period as that used to obtain the coincidence spectrum of interest. The analyzer memory is split into two subgroups. Two fast coincidence circuits with the same resolving time are connected in parallel to the outputs of the timing markers. The timing marker to one of the fast coincidence circuits is delayed a time significantly greater than the resolving time. The same pulse height restriction is imposed on both systems using slow coincidence circuits. The fast-slow coincidence gate obtained from the delayed coincidence circuit is both mixed with the normal coincidence gate and also used as a routing signal. In this way, a sampling of the chance contribution is obtained in one memory group under the same counting conditions as the coincidence spectrum and may be subtracted from the latter.

In a typical coincidence spectrum there are five distinct contributions: the true coincidences, the chance coincidences, the sum-coincidences, the random summing and Bremsstrahlung. Of course, all but the first are undesirable contributions while the remainder can lead to a misinterpretation of the results if their effect is sizeable. To obtain a sum-coincidence event in a coincidence experiment a coincident pair of events must be detected in counter A at the same time as an event of the selected pulse height occurs in detector B. The number of three-member cascades in a decay scheme is normally much less than the number of two-member cascades, so that although geometrically the magnitude of the effect is the same as in single-crystal spectra, its probability of occurrence is generally lower. The effects of Bremsstrahlung and random summing amount to the same relative contributions in coincidence and single-crystal spectra when these events occur in such a manner as to satisfy the logic conditions imposed by the system.

Because coincidence conditions are restrictive, the overall efficiency obtained in a coincidence experiment is much less than that of a single-crystal experiment. For this reason it is usually necessary to use stronger sources and count in a geometry which involves larger solid angles. A compromise must be reached between the desire for good statistics and the higher levels of interference from the above-mentioned extraneous contributions which inevitably accompany increased source strengths and solid angles. Generally speaking, it was usually found satisfactory to sacrifice an order of magnitude in counting rate in order to keep the level of interference as low as possible.

In the coincidence experiments on La^{142} approximately 5 μc sources were used at a distance of 3 cm from the faces of the detectors.

The detectors were placed at 180° and the source was mounted in an anti-Compton shield. The shield is used to prevent the occurrence of scattering between the detectors, an event which is detected as a true coincidence. The source was taped between the two halves of the shield, each of which consisted of one-quarter inch lead plate with a one-half inch hole in the center. This arrangement was found to reduce the scattering between crystals by an order of magnitude when tested with a Cs^{137} source.

4.7 Sum-Coincidence Spectrometer

The two-crystal sum-coincidence spectrometer developed by Hoogenboom (47) can be used to advantage in investigating the time relationships between gamma rays because the spectra obtained are usually simpler. This spectrometer is more selective than the normal fast-slow system and the spectra obtained have fewer components than in the latter case.

The logic arrangement for a sum-coincidence spectrometer is shown in Figure 10. The outputs from detectors A and B, for which the gains have been aligned, are added and amplified in the center channel. A fast-slow coincidence arrangement enables the analyzer only for coincidence events in A and B with an energy sum corresponding to the range of pulse heights selected from the summed distribution. The analyzer sorts events occurring in detector B which satisfy this requirement.

In simple cases, such as that of Sc^{46} shown in Figure 11, very pronounced full-energy peaks are obtained. The partial-energy portion of the NaI(Tl) gamma-ray response is entirely removed, since events of

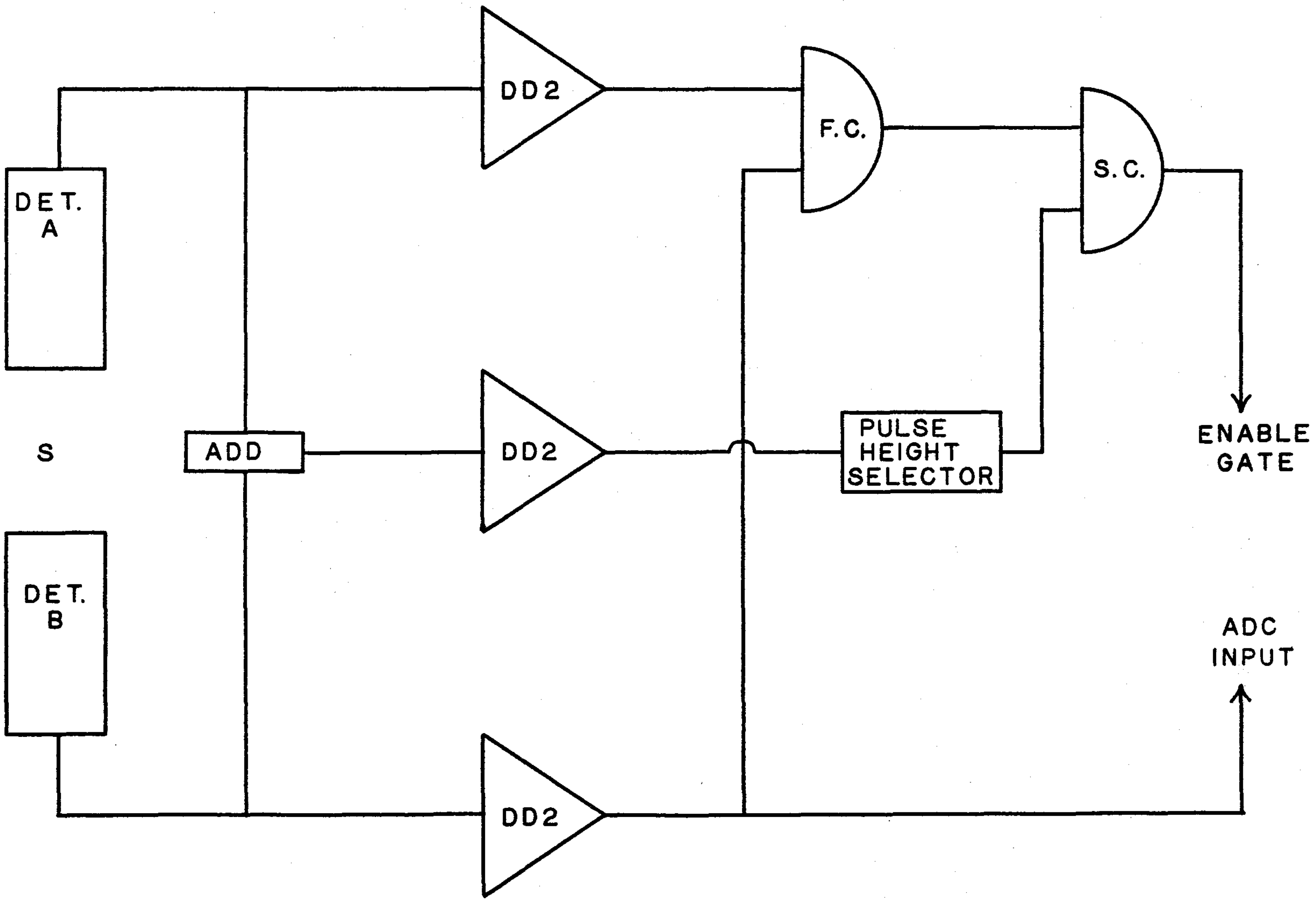

SUM-COINCIDENCE SYSTEM

FIGURE 10

FIGURE 11

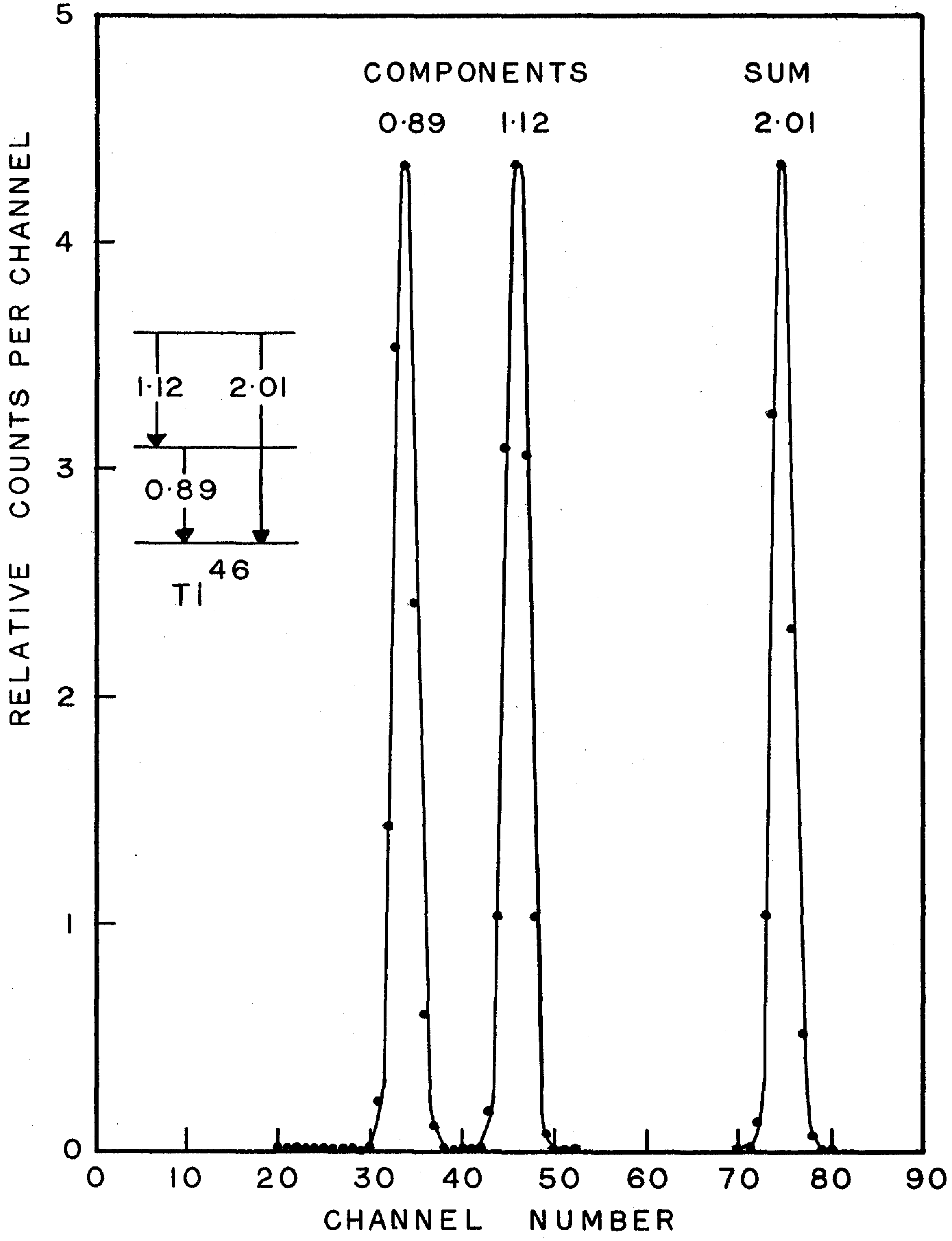
COMPONENTS
0·89
1·12
SUM
2·01
1·12
2·01
0·89
Ti46
RELATIVE COUNTS PER CHANNEL
CHANNEL NUMBER
0
1
2
3
4
5
0
10
20
30
40
50
60
70
80
90

this nature do not fulfill the summed-energy requirement. In the more general case, when the spectra involved are complex, three distinct types of adding can occur, each leading to contributions to the sum-coincidence spectra. The adding of one full energy peak to another gives the result shown in the figure. The adding of one Compton continuum to another, for which there is sufficient energy to give rise to the selected sum energy results in a continuous background which is usually approximately constant. The adding of a photopeak to a Compton continuum leads to the occurrence of "ghost peaks" which occur at an energy equal to the difference between the sum energy and the photopeak energy (48). It is possible to distinguish "ghost peaks" from true peaks, since there is a dependence of peak width on the width of the window set in the pulse-height selector for the latter case. The width of the "ghost peak" is independent of this parameter. Since the accurate determination of peak widths requires very good statistics and a correlation of peak width with sum-channel width requires several runs, this method of distinguishing the two cases is not usually practical. Furthermore, in order to observe this dependence, the pulse-height selector widths must cover a range which includes widths very much less than the natural sum peak width. Since in many cases the sum peak cannot be obtained rapidly, the use of self-gating methods to adjust the window to the desired position before beginning the coincidence run can be very time-consuming. When the half life of the nuclide under investigation is short, accurate setting of narrow windows cannot be achieved readily. An added difficulty resulting from inaccurate window settings is that the coincident photopeaks involved may appear at slightly different energies than their correct values.

Because of these difficulties it was decided to set windows sufficiently wide to accept the entire natural sum peaks. This technique was used in investigating specific properties of certain cascades in La^{142}. Information from other coincidence experiments was used as a guide in interpreting the sum-coincidence spectra. In general, "ghost peaks" are reduced in intensity as compared to true peaks in the same way that a given energy band of the Compton continuum is reduced in comparison to the photopeak in a monoenergetic response. Of course, confusion can arise between a "ghost peak" resulting from an intense line adding with a strong continuum and a low-intensity true peak. Only the stronger peaks in the sum-coincidence spectra were used as definite information.

As suggested by Johnson et al (49), the contribution from coincidence summing contained in a single-crystal spectrum may be determined using a slightly modified form of the arrangement shown in Figure 10. The output from the sum amplifier is connected to the analyzer ADC and the analyzer memory is split into two subgroups. The subset of fast coincidences between detectors A and B are routed to one of the subgroups and the rest of the events are stored in the other. Since the probability of detecting both members of a cascade in either detector A or B is the same as the probability of detecting one member in detector A and one in detector B, the routed subset of events exactly equals the sum-coincidence distribution contained in the combined single-crystal spectra of the two detectors.

If the resolving time of the coincidence circuit from which the routing pulse is derived is lengthened to approximately $2\tau = 2$ µsec, then the routed distribution contains both the coincidence- and random-sum contributions.

Random-sum events may also be detected by sensing the increased width of the corresponding amplifier pulse (50). In addition to the normal zero phase-point timing marker, a timing marker is derived from the leading edge. The leading edge marker is delayed a time equal to the undistorted pulse width and a coincidence requirement rejects abnormally-wide pulses. Both types of sum contributions are illustrated in Figure 12. It should be noted that, unlike the coincidence-sum distribution, the random-sum spectrum is not merely the convolution of the individual gamma-ray response curves. The latter distribution is further complicated by the fact that the effective amplitude of a sum pulse is dependent upon the time difference between the component pulses.

4.8 The Three-Crystal Pair Spectrometer

The identification and determination of the energy and intensity of individual components in the high-energy region of complex gamma-ray spectra is facilitated by using a spectrometer which has higher resolution and a simpler response than the single-crystal scintillation spectrometer. A spectrometer which fulfills these requirements, at the expense of reduced efficiency, is the three-crystal system shown in Figure 13. The center crystal is exposed to the source through a lead collimator three inches thick with a one-half inch diameter hole. The two side detectors are shielded from the

FIGURE 12

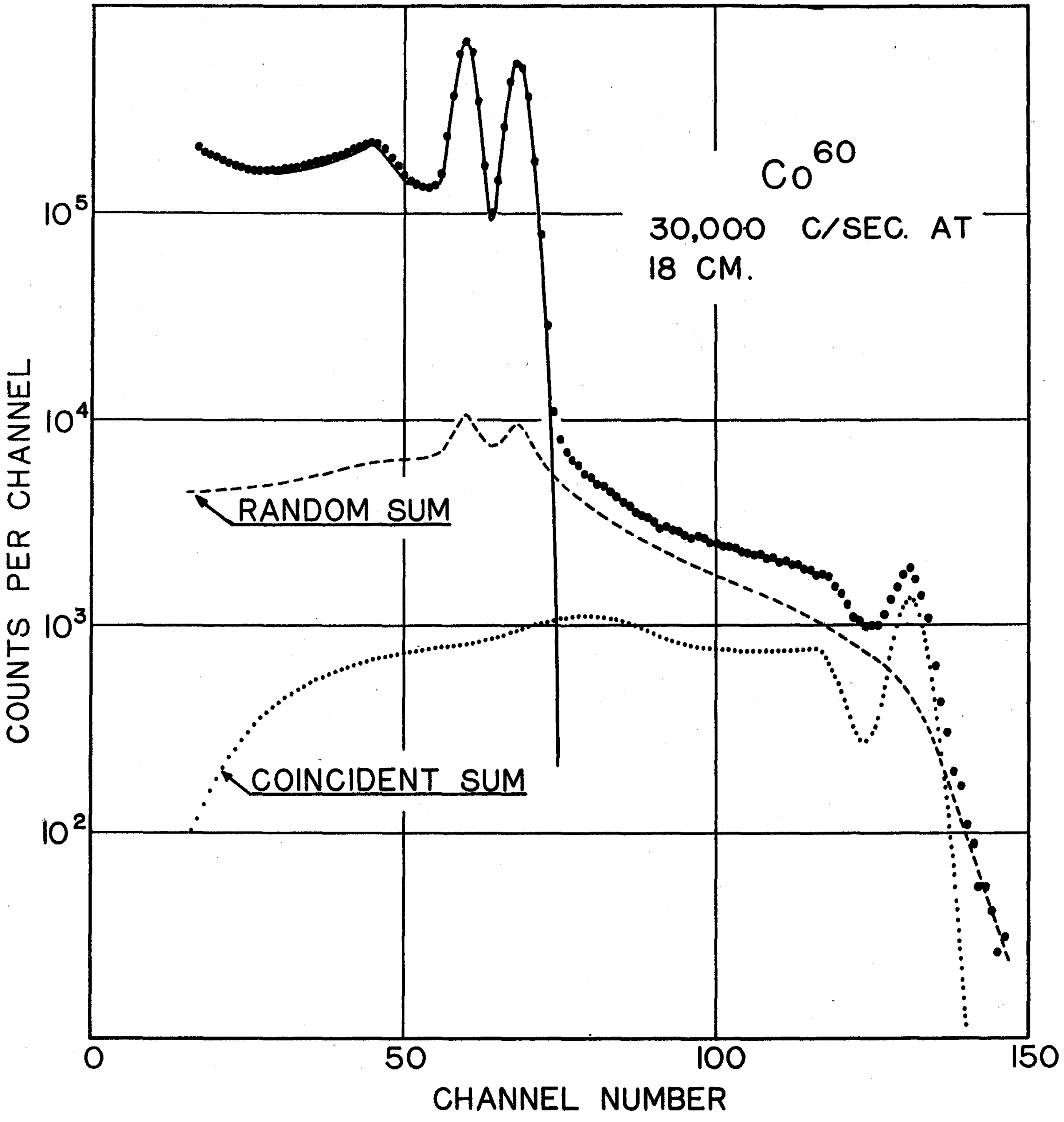
Co^{60}
30,000 C/SEC. AT
18 CM.
RANDOM SUM
COINCIDENT SUM
COUNTS PER CHANNEL
10^5
10^4
10^3
10^2
0
50
100
150
CHANNEL NUMBER

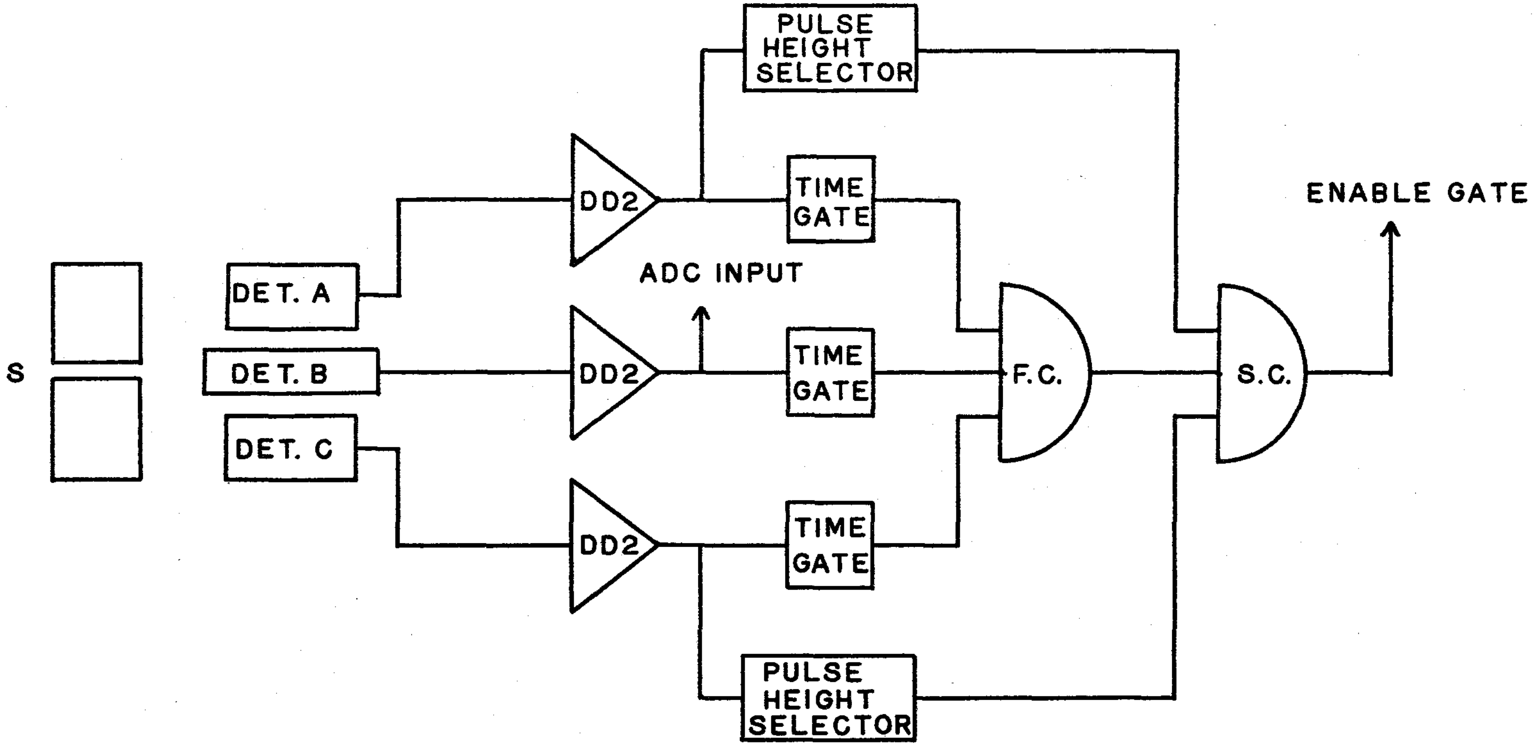

THREE-CRYSTAL PAIR SPECTROMETER SYSTEM

FIGURE 13

source and are used to detect annihilation radiation which escapes from the center crystal. The pulse-height selector windows for these detectors are centered at 0.511 MeV. By requiring a triple fast coincidence together with the above pulse-height condition those events which lead to the second pair escape peak of the single-crystal response are selected.

The spectra of Co^{60} and Na^{24} obtained with the three-crystal pair spectrometer used in this study are shown in Figure 14. The response to a gamma ray of incident energy E_γ is essentially a single peak appearing at a pulse height corresponding to an energy of $E_\gamma - 2m_oc^2$. The effective increase in resolution can be explained by the following arguments. Consider two gamma rays with mean energy E and separation ΔE. Then the relative separation in the single crystal spectrum is $\Delta E/E$ while in the three-crystal pair spectrum the relative separation is increased to $\Delta E/E - 2m_oc^2$. For energies in the region greater than 2 MeV the width of the pair peak is not appreciably greater than the photopeak width so that the resolution of the pair spectrometer is greater than that of the single crystal spectrometer by the factor $E/E - 2m_oc^2$. For example, the relative separation of the Co^{60} gamma ray energies is 12.8% while as can be seen in Figure 14 the relative separation of the corresponding second pair escape peaks is 69.3%, an increase in effective resolving power of a factor of 5.2.

As can be seen from the nature of the scintillator response shown in Figure 7, the second pair escape is the least probable event for the energy range extending to 3 MeV in a three-inch crystal. The relative contribution from pair-escape events is increased in smaller crystals. For this reason a 1.5 x 2-inch crystal was used as the

FIGURE 14

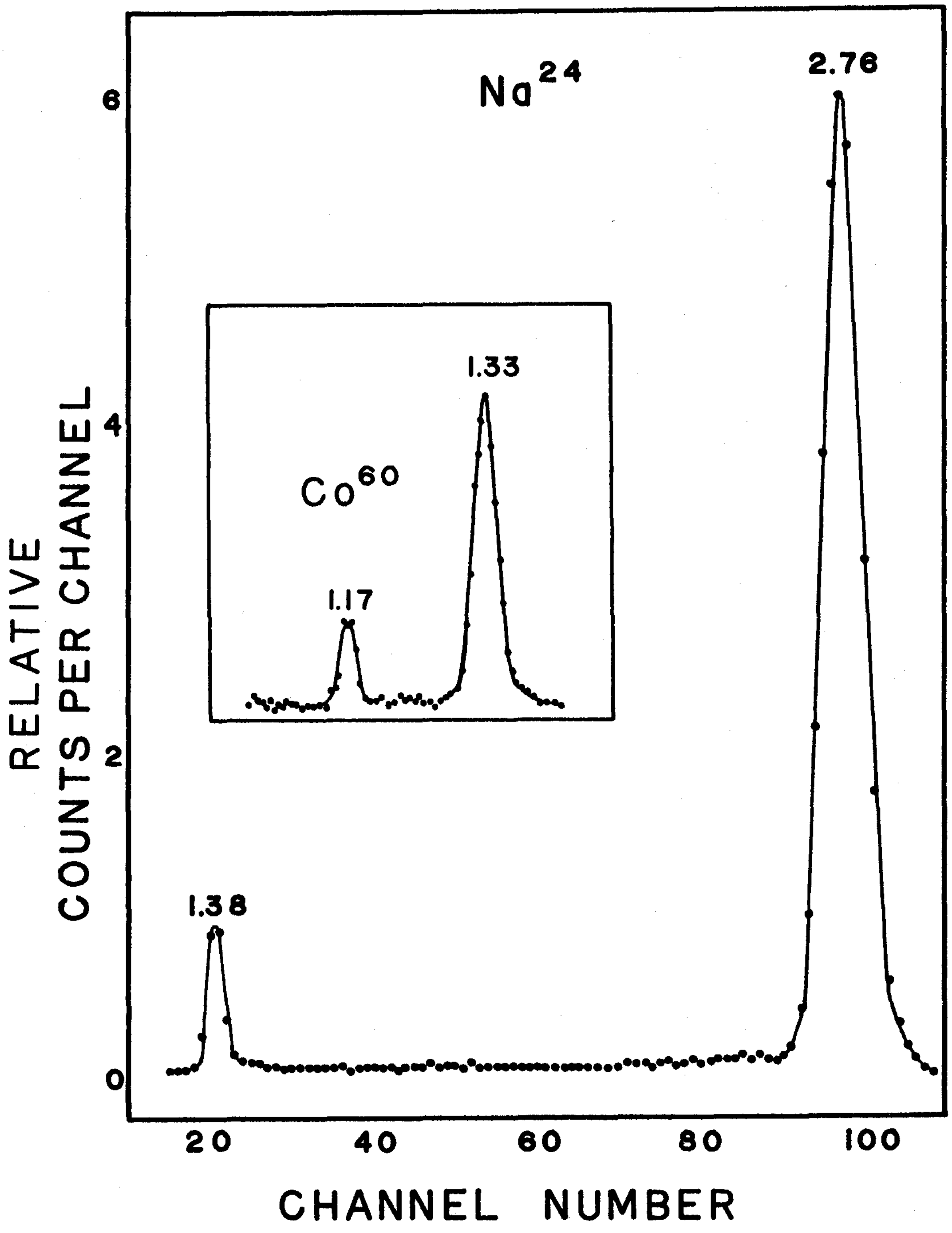
Na^{24}
2.76
1.38
Co^{60}
1.33
1.17
RELATIVE COUNTS PER CHANNEL
0
2
4
6
20
40
60
80
100
CHANNEL NUMBER

central detector. To obtain maximum efficiency for the detection of annihilation radiation escaping from the crystal, the side detectors used were 3 x 3 inch. The relative efficiency as a function of energy follows the pair cross-section curve. The overall efficiency at 2 MeV is approximately 10^{-4} while the resolution at 2 MeV is 3%.

4.9 Scintillation Beta-Ray Spectrometer

Beta spectra were measured using the system described in Section 4.5, with the NaI(Tl) detector replaced by a NE-102 plastic-phosphor beta detector. The phosphor was enclosed with a light-tight mylar cover. The source was placed at a distance from the crystal which was small compared to the range in air of the beta particles of interest. Since in this work the energies of interest were from 0.6 - 4.5 MeV, effects of air absorption and source backing thickness were negligible. The beta spectrum of Cs^{137} measured with this system is shown in Figure 15. The response of the detector to the 0.625-MeV conversion line also shown in the figure was measured by requiring a coincidence between electrons and the 0.032-MeV x-ray.

As in the case of the gamma-ray spectrometer, events occur in which there is only partial transfer of the incident electron energy to the phosphor. At low energies, where the depth of penetration of the incident electron is not great, such events are attributed to backscattering. The range of beta particles generally quoted in nuclear data tables refers to the normal depth of penetration through absorbers which extend over a surface area that is large with respect to the range. Since electrons interacting with matter suffer many large-angle scatterings, the actual distance travelled is much larger

FIGURE 15

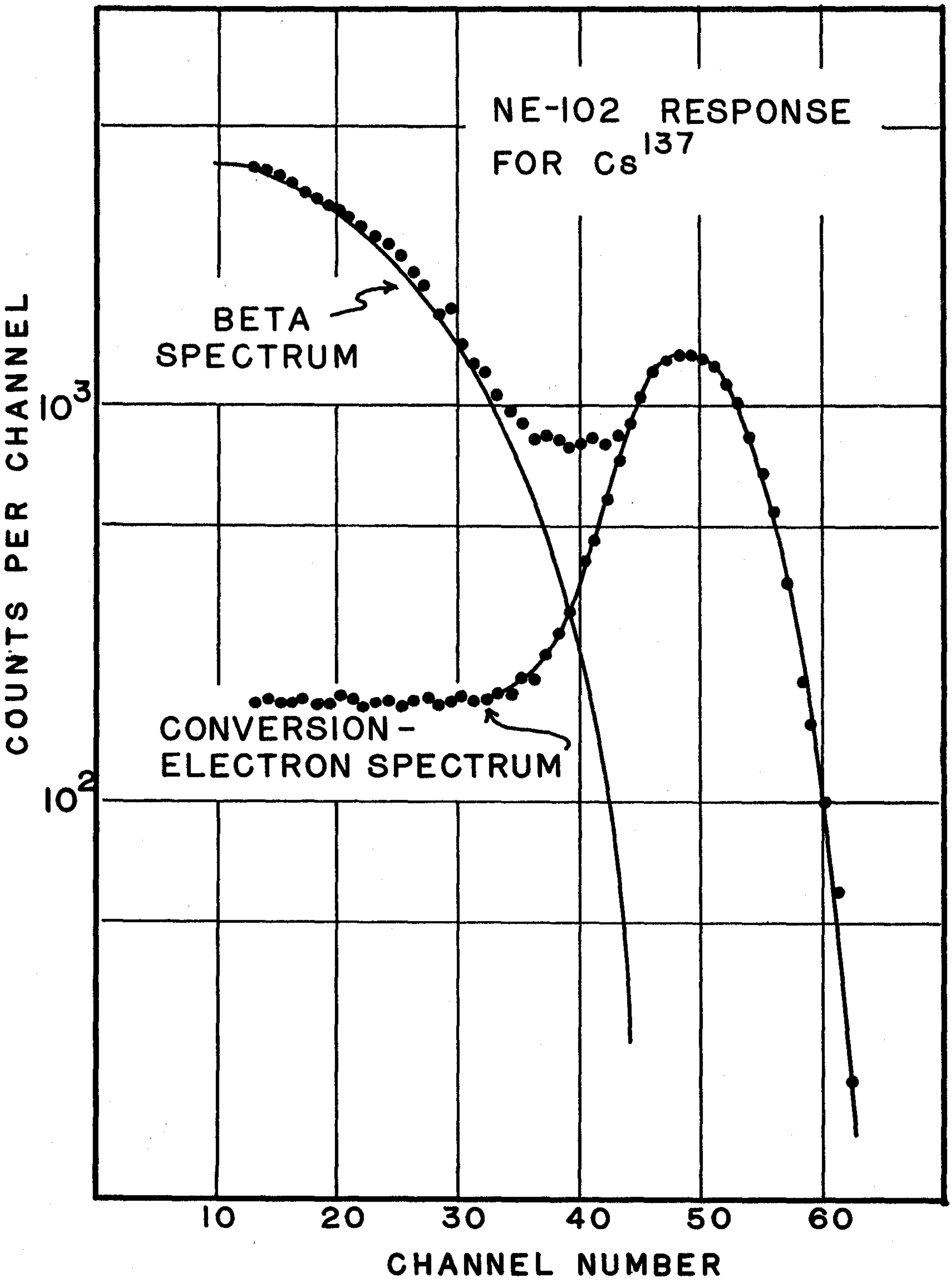
NE-102 RESPONSE FOR Cs^{137}
BETA SPECTRUM
CONVERSION-ELECTRON SPECTRUM
COUNTS PER CHANNEL
10^3
10^2
10
20
30
40
50
60
CHANNEL NUMBER

than the range values quoted. This fact becomes important in the consideration of scintillation beta detectors in which the lateral dimensions can be of the same order as the range. In this case beta particles may be scattered out the sides of the phosphor (51).

For these reasons it is desirable to use a phosphor, the dimensions of which are large with respect to the range of the beta particles of interest. Unfortunately, as the thickness of the scintillator is increased, the relative efficiency for the detection of beta particles, as compared to the efficiency for gamma detection, is reduced. The response of the detector to gamma rays results from Compton events and the distribution is a Compton continuum. It may be argued that by interposing a beta absorber between the source and the detector the gamma-ray contribution to a beta spectrum can be measured and should therefore not constitute a serious problem. Extraneous contributions to beta spectra are more serious than in the case of gamma-ray spectra. This is because in beta spectroscopy one is interested in determining the pulse height for which the counting rate vanishes while in gamma spectroscopy one is interested in positions of maximum counting rate. In addition, since large solid-angle geometries are used, the effects of beta-gamma coincidence summing can become serious unless gamma-ray detection efficiency is small compared to the efficiency for beta particles. For these reasons it is necessary to reach a compromise between the conflicting requirements of minimum gamma-ray efficiency and a maximum of full-energy transfers of incident electron energy.

The effect of random summing is shown in Figure 16. Since the beta transitions are not correlated in time, beta-beta coincidence

FIGURE 16

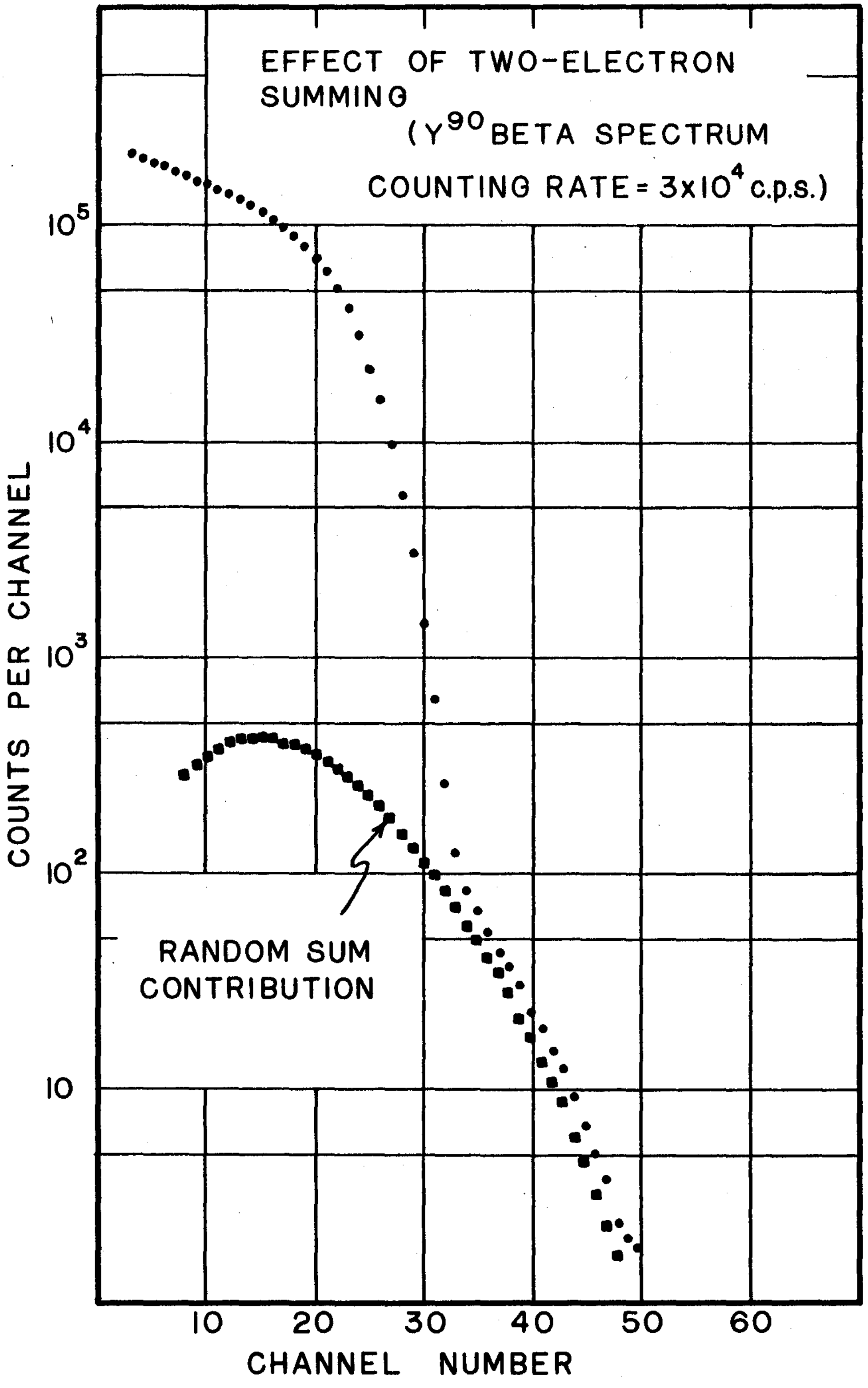
EFFECT OF TWO-ELECTRON SUMMING
(Y^{90} BETA SPECTRUM
COUNTING RATE = 3×10^4 c.p.s.)
COUNTS PER CHANNEL
10^5
10^4
10^3
10^2
10
RANDOM SUM CONTRIBUTION
10
20
30
40
50
60
CHANNEL NUMBER

summing cannot, of course, occur. The contribution from random summing extends beyond the true endpoint of the beta spectrum and can lead to confused interpretation of the data.

The energy pulse-height relation for plastic beta scintillation detectors is linear over the energy range of interest in this work (52). The relation was measured with several calibration sources using the position of Compton edges in the case of gamma-ray sources and endpoints of known beta spectra. The results are shown in Figure 17.

4.10 Multi-Parameter Analysis

The study of the frequency distributions of events, with which are associated several correlated parameters, is facilitated by the use of logic systems which assign a dimension to each parameter and accumulate the events into an appropriate multi-dimensional distribution. For each parameter there is required a detector and an analogue-to-digital converter. The analyzer memory is arranged in an array, the dimension of which is equal to the number of parameters involved. In general, if each parameter is to be studied in the same detail, the memory capacity required is that of a one-dimensional analyzer raised to the power of the number of parameters. For example, in order to obtain the two-dimensional pulse-height distribution corresponding to coincident gamma rays, one may require a memory comprising the order of $(100)^2$ locations, each of which is required to store 10^5 events.

It is only recently that attempts have been made to construct analyzers with such large memory capacities. Previously the approach adopted by researchers requiring multiparameter analysis has been address recording. In the address recording system there is no attempt

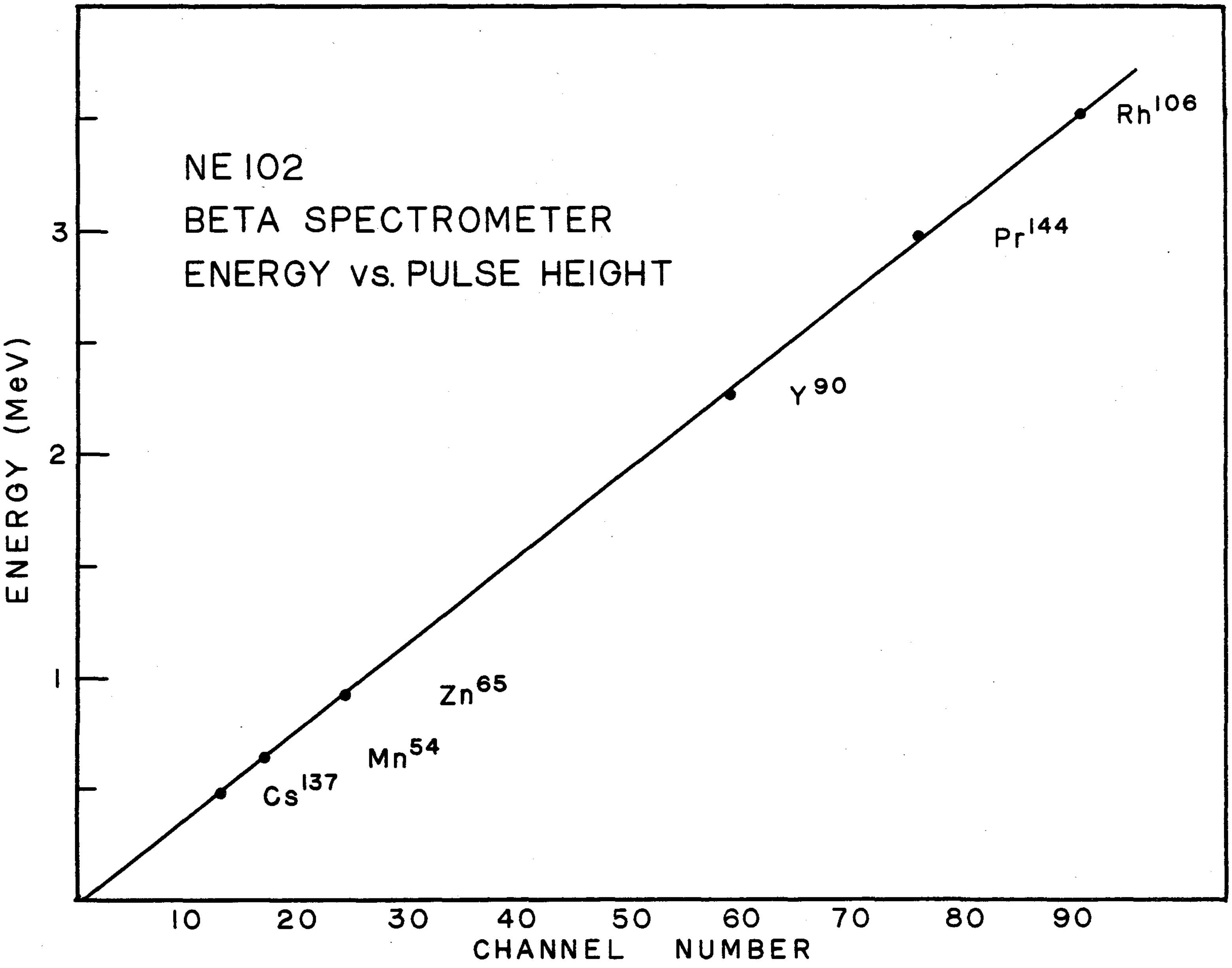
NE 102
BETA SPECTROMETER
ENERGY vs. PULSE HEIGHT
ENERGY (MeV)
1
2
3
10
20
30
40
50
60
70
80
90
CHANNEL NUMBER
Cs137
Mn54
Zn65
Y90
Pr144
Rh106

FIGURE 17

to accumulate and sort events during the experiment. The digitized values of the parameters corresponding to each event are entered on a continuous recording device, usually magnetic tape. The data is searched and converted to the required form in a computer after the completion of the experiment. The advantages and disadvantages of these two approaches has been discussed fully by several researchers (53,54,55).

A simple two-dimensional spectrometer was constructed based on the design of Grodzins (56). Amplifier pulses are stretched and applied to the horizontal and vertical deflection plates of an oscilloscope. The cathode-ray beam is intensified by the output of a coincidence circuit. Each event appears as a spot on the oscilloscope at a position on the screen with co-ordinates which are proportional to the pulse heights produced by the coincident gamma rays in the detectors. The distribution is accumulated by obtaining a time exposure of the oscilloscope screen on a photographic plate. Unfortunately, the results obtained by this method are only semi-quantitative. In addition, when the gamma-ray spectra involved are complex, as in the case of most fission products with total disintegration energies of 3 to 4 MeV, the distribution obtained by this method is not sufficiently detailed to be useful.

A 1024-channel multiparameter analyzer was used to study the beta-gamma and gamma-gamma coincidence distribution of La^{142}. The arrays available with this instrument were 8 x 128, 16 x 64 and 32 x 32 channels in each dimension. Information obtained with this instrument was used to complement that obtained with the fast-slow coincidence spectrometer. Several arrangements were used in the course of the study. The distribution of time-correlated gamma radiation from Sc^{46} is shown in Figure 18 as an example of the form which the results take. Because of the limited number of channels in each dimension, it is not always possible to obtain the entire distribution in one counting period. However, in such cases restricted regions of the distribution may be selected for detailed examination. With the same energy range covered by each axis, the distribution is symmetric about $E_x = E_y$. The coincidence peaks at the positions (1.118, 0.892) and (0.892, 1.118) are approximately two-dimensional Gaussian distributions. Other significant positions of the spectrum are the photopeak, Compton and backscatter combinations.

FIGURE 18

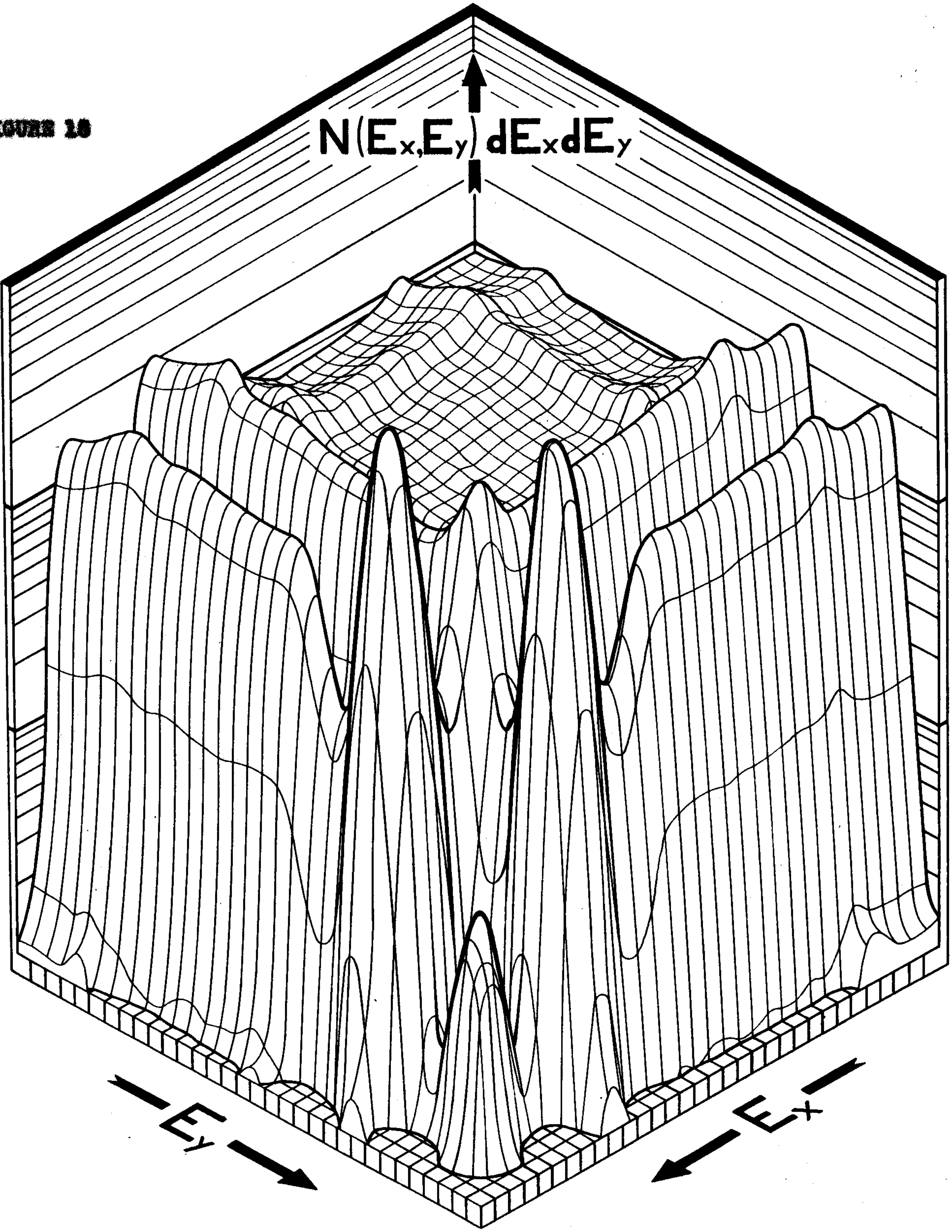

TWO-DIMENSIONAL COINCIDENCE SPECTRUM OF Sc^{46}

CHAPTER V

DATA ANALYSIS

5.1 The General Problem

As has been indicated in the previous chapter the pulse-height distribution of a scintillation spectrometer is much more complex than the actual energy distribution of the incident gamma radiation. The spectrometer can be looked upon as a simple system relating an incident spectrum (object function) to a measured spectrum (image function). A complete description of this relationship is contained in the response characteristics of the spectrometer. The relationship can be derived from the following arguments. Consider the idealized monoenergetic object function $\delta\,(E-E_o)$ corresponding to a discrete incident spectrum of energy E_o. The image function or measured spectrum which results is called the response and denoted by $R\,(E,E_o)$. A knowledge of $R\,(E,E_o)$ for all E_o, i.e. the response surface, constitutes a complete description of the spectrometer as a mathematical system. A general object function $S\,(E)$ satisfies the relation

$$S\,(E) = \int_{-\infty}^{\infty} S\,(E_o)\,\delta\,(E-E_o)\,dE_o \qquad 5.1$$

The image function $M\,(E)$ is therefore related to the object function $S\,(E_o)$ by the relationship

$$M\ (E) = \int_{-\infty}^{\infty} S\ (E_o)\ R\ (E,E_o)\ dE_o \qquad 5.2$$

The measured spectrum is related to the incident spectrum by an integral transform, the kernel of which is the response surface of the spectrometer.

The problem of determining the incident spectrum given the experimental information in the form of the image function involves two distinct aspects obtaining a complete description of the response surface and inverting by some method the integral transform in 5.2. Looked upon in this way the problem becomes awesome indeed. Of the several approaches required to simplify this problem, one in particular, the regression model, leads to a formal description of the didactic philosophy of decay-scheme studies themselves.

5.2 Vector Formulation and Statistical Considerations

The general formulation of the spectrometer performance in mathematical terms involves continuous functions and an integral transform in an infinite dimensional space. In order to reduce the problem to terms more practical as regards data analysis, it is necessary to formulate an approximate description in finite dimensions. It is interesting to note that this step is closely parallel to the analogue-to-digital conversion process. Indeed, the data corresponding to the function M (E) obtained with the multichannel analyzer takes the form of an N-dimensional vector $(M_1, M_2 \ldots M_N)$ where M_i is the number of events accumulated in the memory location i. An approximate form of the integral transform is the finite transformation

$$\vec{M} = R\,\vec{S} \qquad 5.3$$

where R is usually called the response matrix.

Generally speaking, the quality of the finite approximation improves as the dimension is increased. Of course, one is confronted with the practical limitation of memory size. It has been pointed out by other researches (54,55) that the detail obtained using a mesh corresponding to two-hundred channels is sufficient for most cases. No hard and fast criterion can be given since the detail required depends upon the nature of the spectra involved and the methods of analysis adopted.

The most straightforward solution to the problem, inversion of the response matrix, is beset with practical difficulties. If the mesh required for sufficient detail corresponds to 200 channels, the inversion of the response matrix represents a problem beyond the capabilities of present-day computers. The characteristics of the response must be determined experimentally so that the form of the response matrix used is approximate. It is difficult to estimate the effects of inaccuracies in the response matrix. Finally, statistical fluctuations in the data are apparently exaggerated in this method (57).

Aside from these practical difficulties, the success of the inversion method presumably depends upon the mathematical properties of both the transformation and the image and object functions. The object function corresponding to an incident spectrum which is discrete is highly discontinuous. Operating on $\vec{M}$ with R^{-1} in this case leads to an $\vec{S}$ with oscillating components.

The measured spectrum $\vec{M}$ is a random vector. The vector may be assumed to follow the normal multivariate distribution with the variance of each component equal to the magnitude of the component except in the extreme of small or large samples. Components corresponding to only a few events actually follow the Poisson distribution. In the case of large samples, departures from differential linearity in the analyzer will lead to departure from the normal distribution. Since fluctuations in channel widths are less than one percent, this effect is probably not serious except in a detailed statistical analysis of spectra with approximately 10^4 counts/channel, or greater.

5.3 Analysis of Gamma-Ray Spectra

The input function corresponding to a discrete set of n gamma-ray components with energy E_i is given by

$$\vec{S} = \sum_{i=1}^{n} \alpha_i \vec{e_i}$$

where $\vec{e_i}$ is the basic vector in the channel representation corresponding to the energy E_i. The single-crystal scintillation spectrum is given by

$$M(j) = \sum_{i=1}^{n} \alpha_i R(i,j) \quad j = 1,2, \ldots N \qquad 5.4$$

It can be seen from Equation 5.4 that the analysis of a particular gamma-ray spectrum can be carried out without a complete knowledge of the response surface. All that is required is the set of n appropriate sections through the surface cut by the planes E_i. These sections are usually called line shapes $L_i(j) = R(i,j)$ and form a new basis of representation. The spectrum is given by

$$\vec{M} = \sum_{i=1}^{n} \alpha_i \vec{L_i} \qquad 5.5$$

The unknown vector $\vec{\alpha} = (\alpha_1, \ldots \alpha_n)$ is of dimension equal to the number of spectral components, while $\vec{M}$ and $\vec{L_i}$ are N-dimensional vectors, where N is the memory size, so that 5.5 is an over-determined set of linear equations.

To facilitate the analysis of the gamma-ray spectra encountered in this work, a library of line shapes in the energy region of 0.2 - 3.1 MeV was compiled. A set of line shapes was obtained using the standard sources listed in Table III. Line shapes were constructed at intervals of 0.1 MeV by interpolation between adjacent measured profiles. In Figure 19 is shown a percentile plot of the photopeak of Mn^{56} on probability paper. The high-energy side of the photopeak is linear, indicating a Gaussian distribution. Deviations from linearity on the low-energy side result from small angle scattering. The variation of the photopeak width parameter as a function of incident gamma-ray energy and of the ratio of the pair-peak areas to the corresponding photopeak areas were determined from the line shapes of the standard sources. The continuous portion of the response was constructed using point-by-point linear interpolation. The library constituted a convenient reference for the analysis of gamma ray spectra which extend over a large range of energy. The scale change required to apply line shapes from the library to a spectrum was achieved by means of a pantograph.

Since the standard line shapes used in the library were obtained using different channel widths than those used in obtaining

FIGURE 19

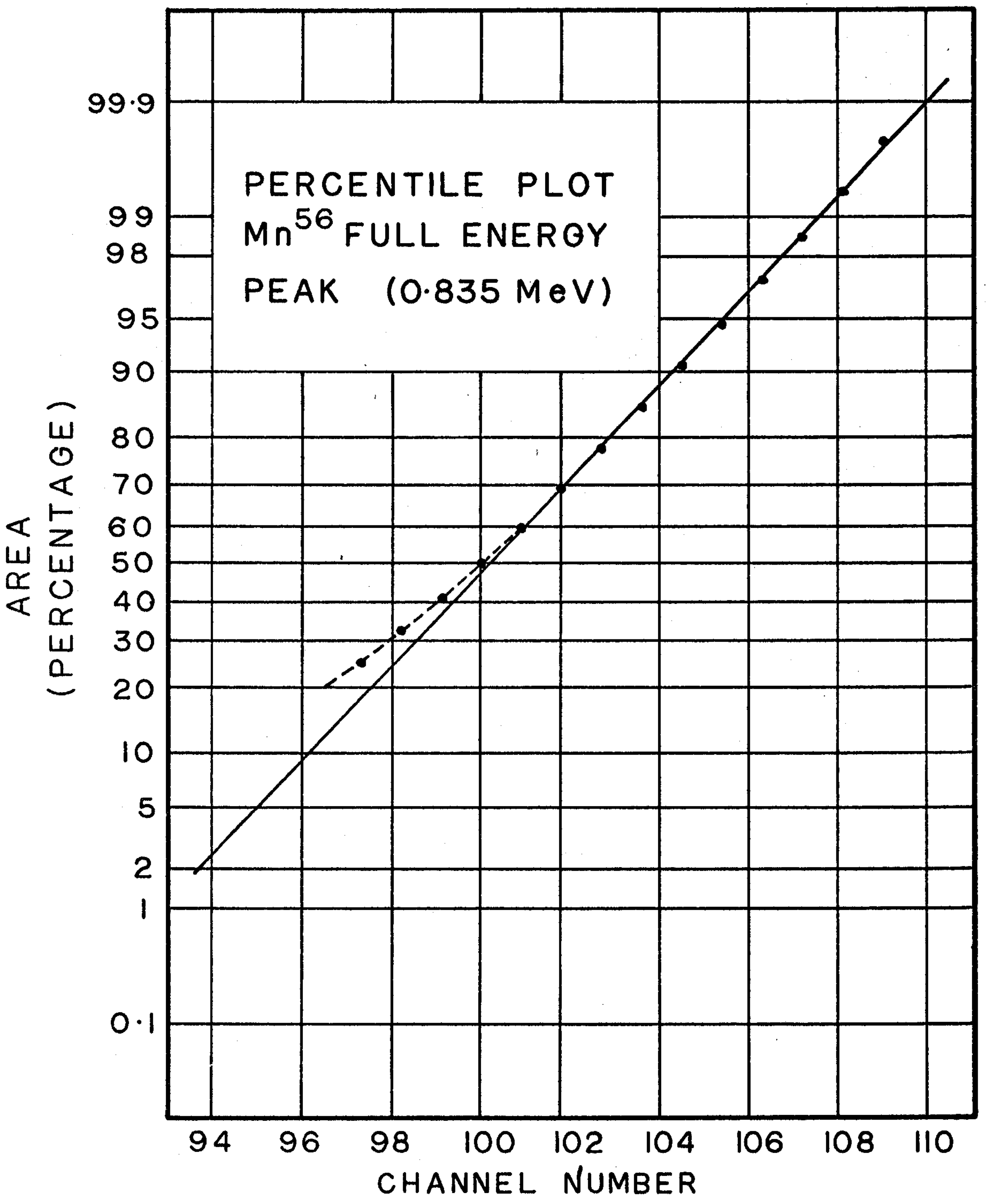
PERCENTILE PLOT
Mn56 FULL ENERGY
PEAK (0·835 MeV)
AREA (PERCENTAGE)
99·9
99
98
95
90
80
70
60
50
40
30
20
10
5
2
1
0·1
94
96
98
100
102
104
106
108
110
CHANNEL NUMBER

TABLE III

Standard Gamma-Ray Sources

Isotope	E_γ (MeV)
Au^{198}	0.411
Cs^{137}	0.662
Mn^{54}	0.835
Zn^{65}	1.114
V^{52}	1.434
La^{140}	1.60
Al^{28}	1.78
Cl^{38}	2.16
Tl^{208}	2.615
Na^{24}	2.76
S^{37}	3.12

the gamma-ray spectra to be analyzed, the effective photopeak widths may differ. For a given channel width w and photopeak width α, the effective photopeak width is approximately $b = (w^2 + \alpha^2)^{1/2}$. The effect of finite channel width only becomes important, therefore, when the channel width is comparable to the line width. In these cases, when it is desired to investigate a limited region of the spectrum in more detail, appropriate standard lines are measured at the same gain as that used for the spectrum.

The simplest method of analyzing gamma-ray spectra is the method of successive subtractions, or stripping. The stripping can be carried out conveniently using graphical analysis. The appropriate line shape is fitted to the highest energy photopeak and the contribution corresponding to the detector response to this gamma ray is subtracted from the total spectrum. The process is repeated using the highest energy photopeak occurring in the first residual and this procedure continued until all the components have been fitted. Spectrum stripping, despite the tedium of the method, is probably the most widely used approach to the analysis of gamma-ray spectra. Since the analyst is closely controlling the procedure, subjective allowances for possible inaccuracies in line shapes and extraneous contributions are made. The estimate of the incident spectrum represented in the model basis as $\vec{S} = (\alpha_1, \alpha_2 \ldots \alpha_n)^t$ is biased. Full use of the data is not made in the sense that no attempt is made to satisfy consistently the complete set of Equations 5.5. Because it is possible to make allowances in the analysis for inaccuracies of the model, it was decided to use this method extensively in the analysis of the gamma-ray spectra measured in this study. Components of the spectrum revealed by the graphical analysis were considered tentative unless their existence was patently obvious and more clear-cut evidence from other experiments was required before they were considered as definite. In the case of photopeaks corresponding to unresolved gamma rays all that could be done as a first step was to note any anomalous peak widths. The analysis was repeated as further information indicated a refinement of the model was necessary.

A more sophisticated approach which makes full use of the data and leads to an unbiased statistically-significant estimate is multiple regression (or the method of least squares). The most general approach in which both the energies and intensities of the spectral components are treated as variables is a non-linear problem requiring iterative methods. When a more restrictive model based upon both the number of components assumed and their energies is used, the problem is linear in the remaining unknown α_i. The regression model manifests itself in the n x N design matrix $X_{ij} = L_i(j)$ and 5.5 becomes $\vec{M} = X\vec{S}$, so that the incident spectrum consists of the regression co-efficients $\vec{S} = (\alpha_1, \alpha_2 \ldots \alpha_n)^t$. The requirement of minimum residual leads to the normal equations

$$\vec{S} = (X^t \omega X)^{-1} \; X^t \omega \vec{M} \qquad 5.6$$

where ω is the diagonal weighting matrix,

$$\omega_{rr} = \frac{1}{\sigma_r^{\;2}} = \frac{1}{M_r}$$

and $C = (X^t \omega X)^{-1}$ is the variance-covariance matrix. The weighted residual is given by

$$p = (M - XS)^t \;\; \omega(M - XS) \qquad 5.7$$

and the covariance (unbiased estimate) between the components a_i, a_j is given by

$$\sigma_{ij} = C_{ij} \frac{p}{N - n} \qquad 5.8$$

The advantages of multiple regression over stripping are twofold. The results obtained are unbiased estimates of the regression coefficients and their associated correlation matrix. In addition, goodness-of-fit criteria, such as the χ^2-test, and analysis of variance techniques indicate the correctness of the regression model and the significance level of each component of the model respectively. However, these criteria, especially the first, rely upon assumptions about the statistical nature of the data itself. For instance, if an unlikely value of χ^2 is obtained it could indicate that the design matrix which contains essentially all the physical assumptions of the model is incorrect or that some statistical requirement has not been fulfilled. It may be that $\vec{M}$ is not distributed according to a normal multivariable distribution and that incorrect estimates of the component variances have been used in the weighting matrix.

Assuming that the statistical requirements are fulfilled, a detailed interpretation of the results of a regression analysis requires further stringent conditions to be met. For instance, if the test indicates that the design matrix is incorrect, it may be because too few components have been assumed or that the line shapes used are not appropriate. Instabilities in the overall gain of the analyzer system, such as arise from counting-rate shifts, cause a broadening of the photopeaks and a general smearing of the spectrum. This effect is usually too small to be detected in the rather insensitive stripping method.

Incorrect positioning of the line shapes and the use of too few components in the design matrix may be detected by observing the differential residual (M - XS). If a line shape has been incorrectly positioned the residual will oscillate in the region of the photopeak concerned. If a component has been omitted and is statistically significant, a peak in the residual will occur.

A complete program for the regression analysis of gamma-ray spectra would require a means of generating line shapes, and a preliminary stripping procedure leading to an approximate design matrix, as well as the solution of the normal equations and the application of statistical tests. Such a program was beyond the scope of this study. However, the single-crystal spectrum of La^{142} was analyzed using the results of the graphical analysis as a basis for the design matrix in a regression program for the Bendix G-15 Computer. The quality of the fit is shown in Figure 20. In addition, when studying the angular correlations of some cascades, limited regions of the spectra measured at each angle were analyzed using this method.

In summary, it might be mentioned that the use of a regression model has decided advantages over the straightforward inversion of the response matrix in the channel-basis representation. The inversion of the correct design matrix, which contains no irrelevant information and is therefore of much smaller dimension, is more efficient than the general method. Despite this it is hoped that investigations of the general method will lead to success in the future. No assumptions are necessary in this approach and a regression model based upon a statistical distribution representing the response-corrected spectrum is the most satisfactory analytical approach.

FIGURE 20

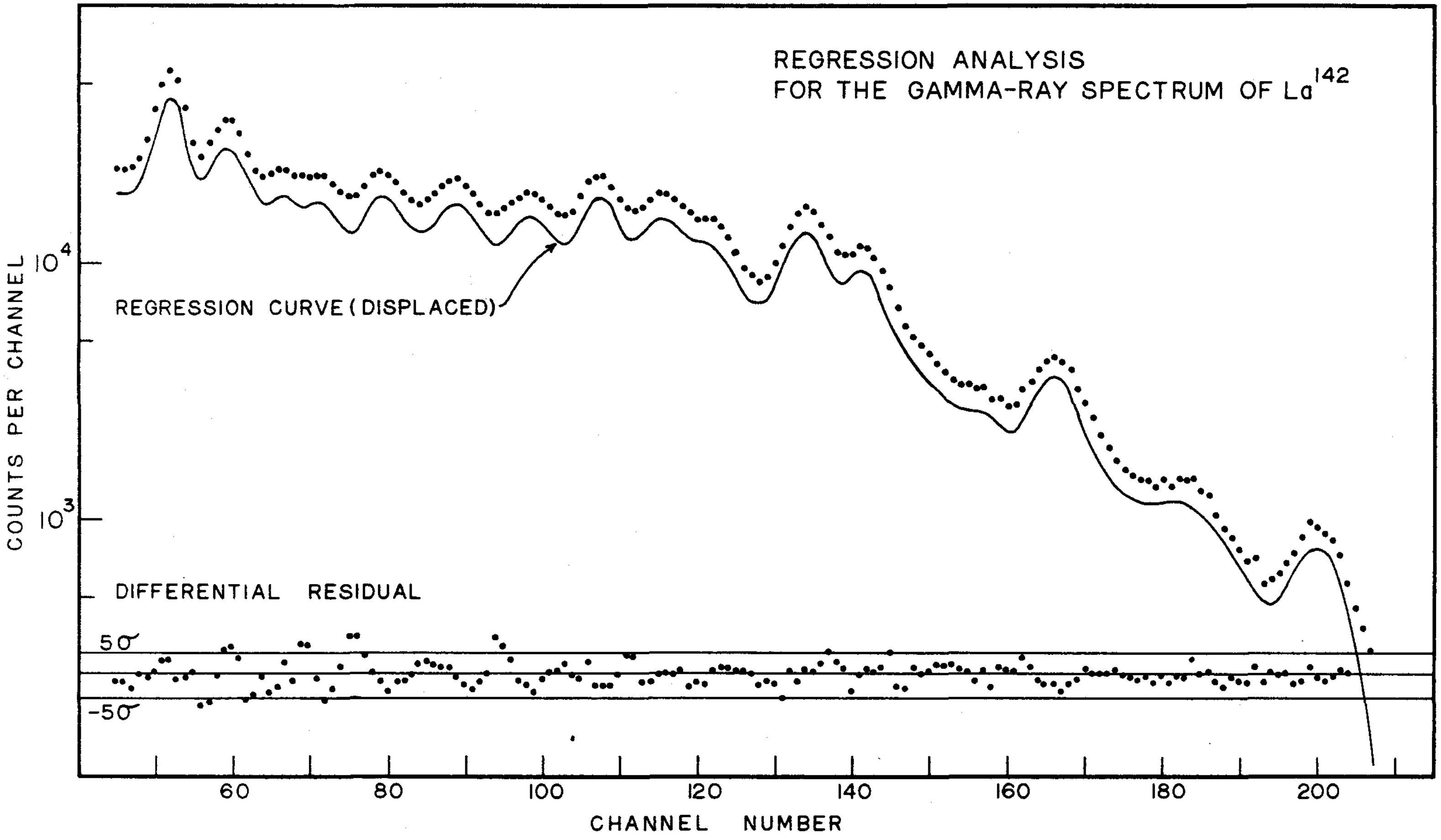
REGRESSION ANALYSIS
FOR THE GAMMA-RAY SPECTRUM OF La^{142}
REGRESSION CURVE (DISPLACED)
DIFFERENTIAL RESIDUAL
5σ
-5σ
COUNTS PER CHANNEL
10^4
10^3
60
80
100
120
140
160
180
200
CHANNEL NUMBER

5.4 Analysis of Gamma-Gamma Coincidence Spectra

As discussed in the section on multi-parameter analysis the distribution of coincident events determined by a pair of counters is two-dimensional, one dimension being associated with each counter. The general formulation of spectral analysis is easily extended to this case and the relation between image and object functions is given by

$$M(E_x,E_y) = \int R_A(E_x,E'_x)\, R_B(E_y,E'_y)\, S(E'_x,E'_y)\, dE'_x dE'_y \qquad 5.9$$

where x and y are the dimensions assigned to counters A and B respectively. The functions $M(E_x,E_y)$ and $R(E,E')$ are defined in Section 5.1. The transformation from the channel basis to the model basis leads to the equation

$$M(E_x,E_y) = \sum_{i=1}^{n} \sum_{j=1}^{n} q_{ij}\, L_i(E_x)\, K_j(E_y) \qquad 5.10$$

where $L_i(E_x) = R_A(E_i,E_x)$ and $K_j(E_y) = R_B(E_j,E_y)$. Equation 5.10 is the corresponding two-dimensional regression model. A multiple regression solution to this problem which takes into account both dimensions simultaneously leads to a variance-covariance matrix of dimension n^2. However, since the variables are separable, it is possible to analyze the distribution in two steps.

For a fixed E_x, a fit can be performed to 5.10 in the form

$$M(E_x,E_y) = \sum_{j=1}^{n} \alpha_j(E_x)\, K_j(E_y). \qquad 5.11$$

This step is repeated for each of the N channels in the x-direction leading to the set of N equations

$$\alpha_j(E_x) = \sum_{i=1}^{n} q_{ij} L_i(E_x) \qquad 5.12$$

each of which can be fitted to obtain the q_{ij}. The distribution $\alpha_j(E_x)$ is referred to as the spectrum in coincidence with γ_j.

When coincidence studies are carried out using the fast-slow coincidence spectrometer, usually only portions of the two-dimensional spectrum are measured. Consider an experiment in which a window centered at E_o of width $2\Delta E$ is imposed by the pulse-height selector of the system. The coincidence spectrum under these conditions is given by

$$C(E_y) = \int_{E_o - \Delta E}^{E_o + \Delta E} M(E_x, E_y)\, dE_x \qquad 5.13$$

$$= \sum_{j=1}^{n} \int_{E_o - \Delta E}^{E_o + \Delta E} \sum_{i=1}^{m} L_i(E_x)\, dE_x \quad q_{ij} K_j(E_y)$$

Designating the window contribution arising from γ_i as D_i, then 5.13 can be written

$$C(E_y) = \sum_{j=1}^{n} p_j K_j(E_y) \quad \text{where} \quad p_j = \sum_{i=1}^{n} D_i q_{ij} \qquad 5.14$$

Usually the window position E_o is set to correspond to the full-energy peak of a particular gamma ray of interest. Then the correlation coefficient corresponding to coincidences between the gating gamma ray γ_r and a gamma ray γ_s occurring in $C(E_y)$ is given by

$$q_{r,s} = \frac{1}{D_r}\left[p_s - \sum_{i \neq r} D_i\, q_{i,s} \right] . \qquad 5.15$$

With the fast-slow system, each measurement of $C(E_y)$ usually requires a separate experiment and it is necessary to normalize p_s so that the analysis leads to meaningful comparisons. In this work the normalization suggested by O'Kelley (58) was adopted.

$$q_{r,s} = \frac{1}{D_r}\left[\frac{P_s e^{\mu d}}{C_W \epsilon_s} - \sum_{i \neq r} D_i q_{i,s} \right] \qquad 5.16$$

where P_s is the area of the photopeak of the distribution $p_s\, K_s(E_y)$ and C_W is the number of events in the window. The photopeak area is corrected for absorption losses ($e^{-\mu d}$) and photo-efficiency (ϵ_s).

The correlation coefficients normalized in this manner are referred to as coincidence quotients. The coincidence quotient $q_{r,s}$ is the ratio of the number of coincident events corresponding to the cascade pair (γ_r, γ_s), to the number of gating events corresponding to γ_r, the gamma ray of interest. The gating fraction D_i, $i \neq r$ represents the extraneous contribution to the window which results from the partial-energy portion of the response $L_i(E_x)$, when $E_i > E_r$. This is illustrated in a typical self-gated spectrum of La^{142} in Figure 21. The contributions to the region covered by the window are obtained by numerical integration of the equation

FIGURE 21

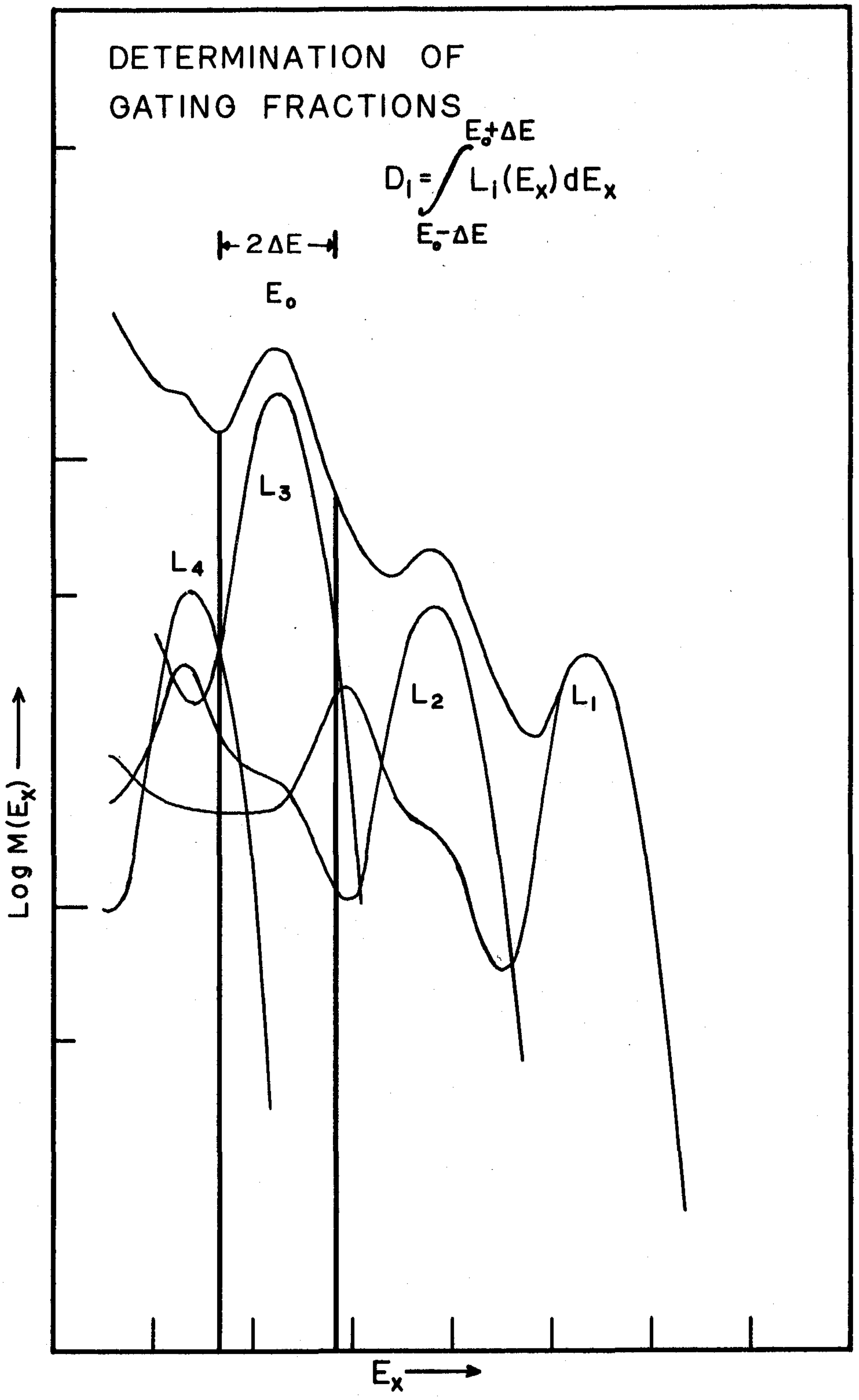
DETERMINATION OF GATING FRACTIONS
$D_1 = \int_{E_0-\Delta E}^{E_0+\Delta E} L_1(E_x)\, dE_x$
2ΔE
E_0
L_3
L_4
L_2
L_1
Log M(E_x)
E_x

$$D_i = \int_{E_o - \Delta E}^{E_o + \Delta E} L_i(E_x)\, dE_x \qquad 5.17$$

The composition of the window assumed in the analysis is of course based on the results of the single-crystal analysis.

The spectrum $C(E_y)$ is analyzed graphically in the same manner as the single-crystal spectrum. Coincidence-quotient analysis is the natural extension of stripping to two dimensions. The method of analysis can be most easily appreciated by considering the following experimental design. A window is first positioned at E_n which corresponds to the highest energy photopeak, in which case $D_n = 1$ and $D_i = 0$, $i \neq n$. Coincidence spectra are measured for window settings $E_n, E_{n-1}, \ldots E_1$, and each spectrum is corrected for the contribution of coincidences from higher-energy gamma rays by successive subtractions as represented by the term

$$\sum_{i \neq r} D_i\, q_{i,s}$$

This procedure contains the same disadvantages as the one-dimensional stripping analysis. One refinement possible is to use regression techniques for the analysis of each $C(E_y)$.

The expression given for the coincidence quotient above is approximate since the effects of coincidence and random summing, Bremsstrahlung and angular correlation have been neglected. The exact corrections for these effects, which are present in both detectors, are difficult to make. If it is possible to obtain their relative contribution to the single-crystal spectrum, then they may be included in the gating fractions D_i. On the other hand, the contribution to which they give rise in $C(E_y)$ is usually impossible to determine. It is possible to correct for random and coincidence summing in crystal B, either experimentally or analytically. An experimental determination of this contribution could be obtained by using three crystals in a natural though complicated extension of the method discussed previously (Section 4.7). An approximate analytical correction can be made if one has some idea of the coincidence relations before hand. Consider the case of a three-member cascade, $\gamma_1, \gamma_2, \gamma_3$ and a cross-over cascade γ_1, γ_4, for which $E_{\gamma_4} = E_{\gamma_2} + E_{\gamma_3}$. Then the appropriate response to $\gamma_4, K_4(E_y)$ is complemented by the sum coincidence contribution from γ_2, γ_3. The photopeak area of γ_4 is given by

$$N_4 = P_4 + P_2 \varepsilon_3 q_{3,2} + 2\tau P_2 P_3. \qquad 5.18$$

The actual area, P_4 is obtained by subtracting the sum-coincidence contribution, $P_2 \varepsilon_3 q_{3,2}$ and the random summing contribution $2\tau P_2 P_3$. If a regression analysis of $C(E_y)$ is to be carried out, the actual shapes of these contributions must be included in the design matrix.

The coincidence quotient relation can be modified to include angular correlation effects (58). However, the angular correlations are seldom known during the initial stages of a decay-scheme study.

A complete coincidence-quotient matrix is used in conjunction with the single-crystal intensities to test the validity of the various decay-schemes postulated on the basis of the coincidence relations. Once an acceptable decay scheme is constructed the quotients are used to obtain the gamma-ray intensities by an iterative procedure which proceeds until internal consistency is achieved.

Strictly speaking, the diagonal elements of the coincidence matrix should all be zero. However, in practice, when a cascade pair consists of members which cannot be resolved and therefore are indistinguishable, the result can appear as a non-zero diagonal element.

5.5 Analysis of Beta Spectra

Unlike the discrete object function corresponding to the incident gamma-ray spectrum, the object function deriving from a beta transition of energy E_o is continuous. In this case, therefore, correction for finite response requires the inversion of the integral transform 5.1. For an allowed transition of energy E_o,

$$S(E) = k_o \, pW(E_o - E)^2 \, F(Z,W) \qquad 5.19$$

where p and W are the relativistic momentum and energy and F(Z,W) is the Coulomb factor. The equation is usually re-arranged in the form of a Kurie plot

$$\frac{S(E)}{f}^{1/2} = (k_o)^{1/2} (E_o - E), \quad f = F(Z,W)\ pW \qquad 5.20$$

As indicated in Section 4.9, the response function has the approximate form

$$\begin{aligned} R(E,E') &= k + \exp - \frac{(E' - E)^2}{\alpha(E')^2} \qquad E<E' \\ &= \exp - \frac{(E' - E)^2}{\alpha(E')^2} \qquad E>E' \end{aligned} \qquad 5.21$$

where, according to Freedman et al (59), k is independent of E'. An extensive investigation of the response function for the energy range of interest in this work, 0.5 - 5.0 MeV, is made difficult by the lack of naturally occurring monoenergetic electron sources over this range of energies. Indeed, there is a scarcity of long-lived standards with simple beta-ray spectra in this region. It was decided to calculate the shape of the measured spectra for $Sr^{90}-Y^{90}$ (2.3 MeV) and $Ce^{144}-Pr^{144}$ (2.98 MeV) using the value of k determined from the Cs^{137} conversion line. The parameter α was adjusted for agreement with experimental data. The iterative inversion procedure of Freedman et al (59) was then used to correct the measured spectra for resolution effects. The equation of iteration is

$$S^{(n+1)} = S^{(n)} + M - R\,S^{(n)};\ S^{(o)} = M. \qquad 5.22$$

As a first test, the response correction was applied to a calculated M, the results of which are shown in Figure 22a. Kurie plots of response-corrected $Ce^{144}-Pr^{144}$ and $Sr^{90}-Y^{90}$ spectra are shown in Figure 22b. The main difficulty encountered with the direct application of this method is an exaggeration of the statistical fluctuations in the data. It was found necessary to smooth the spectra before iterating.

A convenient response correction satisfactory for the beta spectra involved in this study was based on a comparison of calculated spectra M with object functions S. Consider the spectrum for a beta transition of energy E_o. Then it is possible to calculate the correction factor

$$g_{E_o}(E) = \frac{S(E)}{M(E)} \text{ so that } S(E) = g_{E_o}(E)\,M(E).$$

Kurie analysis of complex beta-ray spectra is, like spectrum stripping, a procedure of successive subtractions beginning at the high-energy end in the region for which only one group contributes to the spectrum. The difficulties of such an analysis, particularly when the endpoint energies are unknown, are severe even in very pure spectra obtained with magnetic spectrometers for which the effects of finite response are not large. For example, two beta groups of comparable intensities and endpoint energies tend to be analyzed as a combined single group. Similarly, a group of lower energy and intensity may be obscured by a high-intensity group.

If we consider a complex incident spectrum

$$S(E) = \sum_{i=1}^{n} S_i(E)$$

then the measured spectrum is given by

$$M(E) = \sum_{i=1}^{n} \frac{S_i(E)}{g_i(E)}$$

Analysis of the high energy group follows from

$$S_n(E) = g_n(E)\, M(E) - \sum_{i=1}^{n} S_i(E)\, \frac{g_n(E)}{g_i(E)}$$

The construction of a regression model for a complex beta spectrum is a much more difficult problem than the corresponding case of a gamma-ray **spectrum.** A prerequisite is a knowledge of the number of components, their nature (allowed or forbidden shape) and their endpoint energies. This information also provides a useful guide for graphical Kurie analysis but cannot be arrived at easily. It was decided to obtain a model for analysis based on the examination of several beta-gamma coincidence spectra. Generally speaking, these spectra are much simpler and provide an indication of the model to be

FIGURE 22 (a)

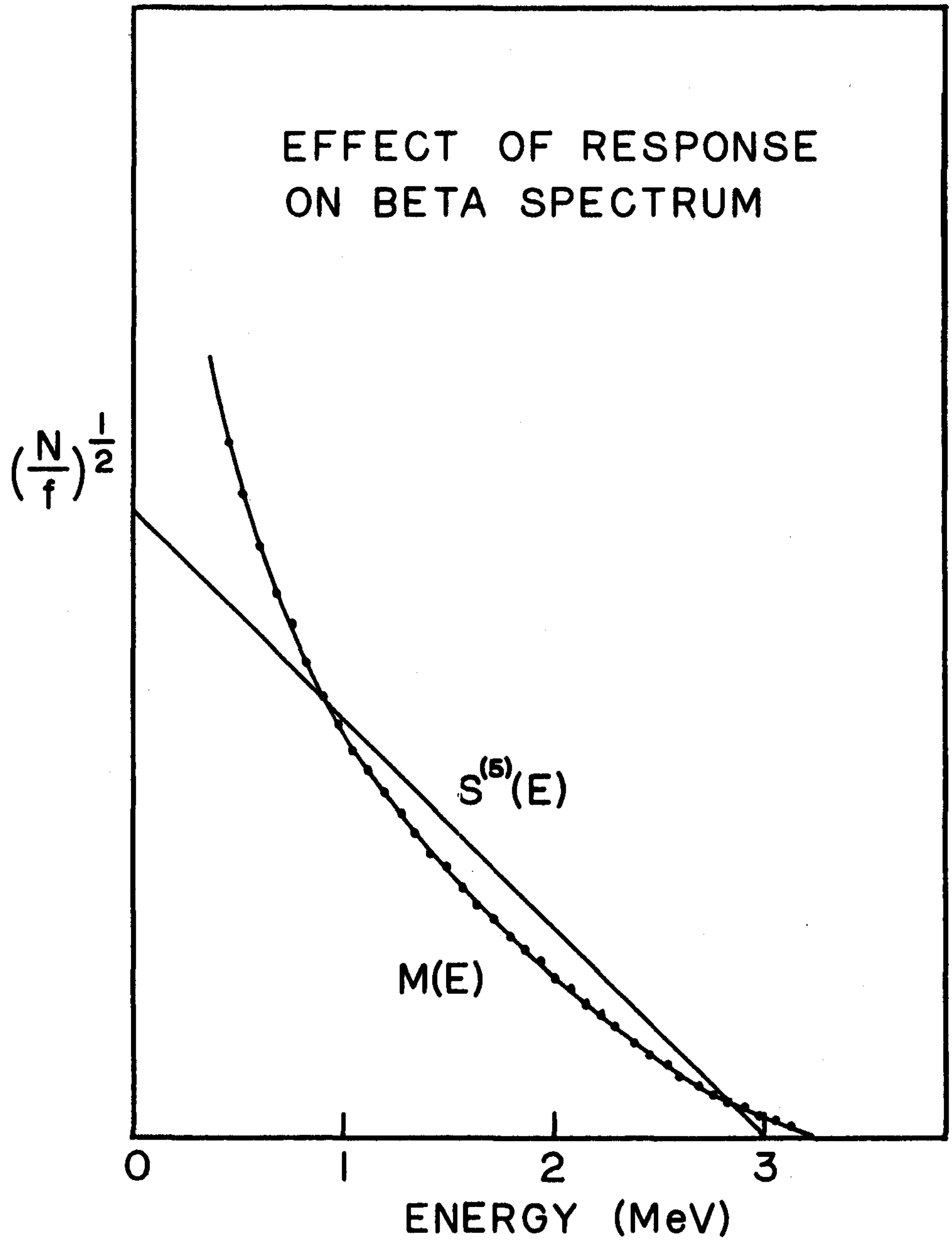
EFFECT OF RESPONSE
ON BETA SPECTRUM
$\left(\frac{N}{f}\right)^{\frac{1}{2}}$
$S^{(5)}(E)$
M(E)
0
1
2
3
ENERGY (MeV)

FIGURE 22 (b)

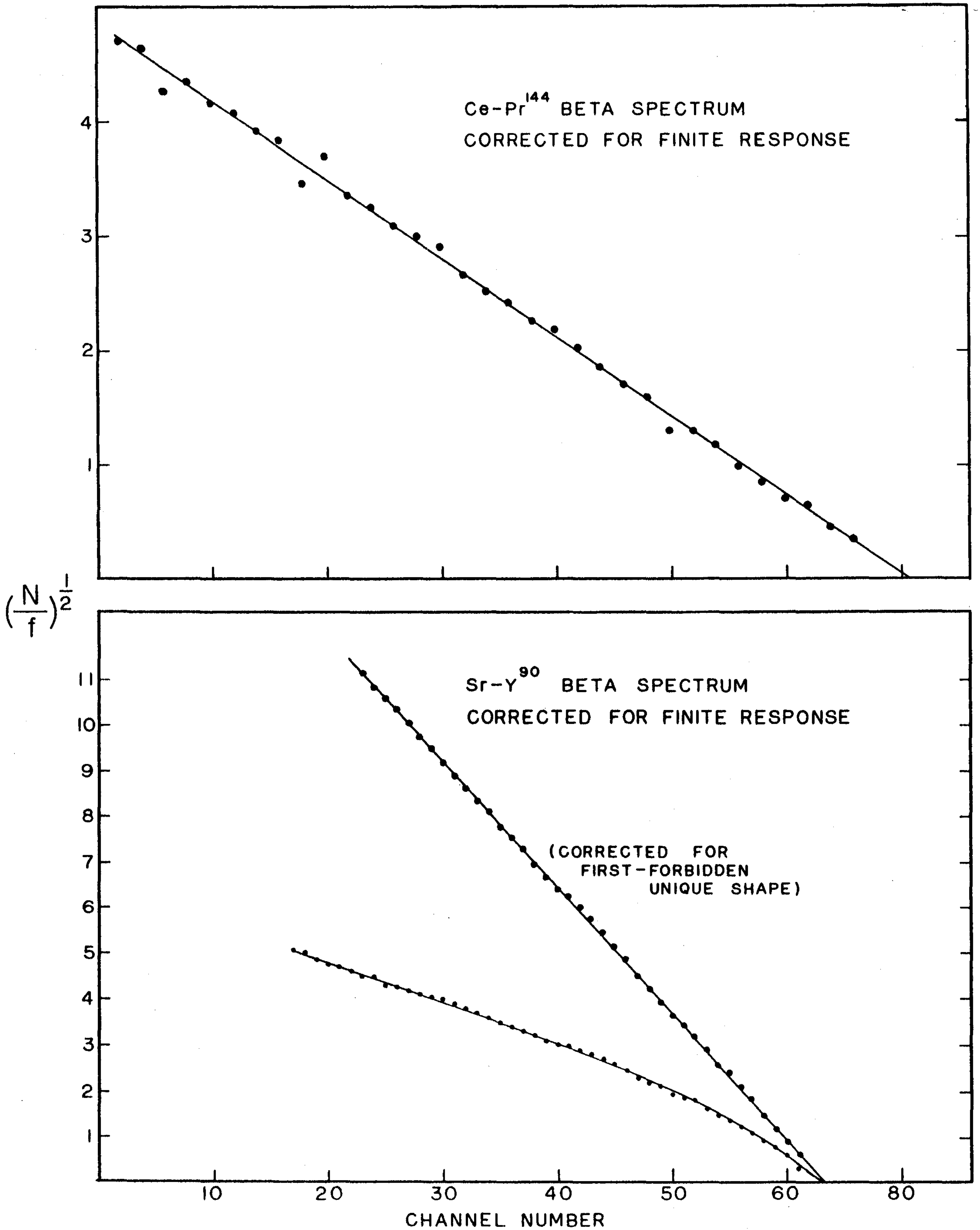
Ce-Pr^{144} BETA SPECTRUM
CORRECTED FOR FINITE RESPONSE
1
2
3
4
$\left(\frac{N}{f}\right)^{\frac{1}{2}}$
Sr-Y^{90} BETA SPECTRUM
CORRECTED FOR FINITE RESPONSE
(CORRECTED FOR
FIRST-FORBIDDEN
UNIQUE SHAPE)
1
2
3
4
5
6
7
8
9
10
11
10
20
30
40
50
60
80
CHANNEL NUMBER

used. An extensive investigation of the general problem of spectral analysis for beta continua is outside the scope of this study.

5.6 Analysis of Angular Correlation Data

Both the fast-slow coincidence system and the sum-coincidence system are used in angular correlation studies. Analysis of the fast-slow coincidence data consists of obtaining the coincidence co-efficients as a function of angle, $p_j(\Theta)$ suitably normalized. The analysis of the sum-coincidence data is much more straightforward because of the simpler nature of the spectra involved. The areas of the relevant sum-component peaks are determined by numerical integration and normalized to correspond to an equal number of singles events. As has been pointed out in Section 4.7 for this work, only those parts of the spectrum definitely established to correspond to true sum-coincidence peaks were analyzed. The normalized correlation functions are fitted to an equation of the form

$$W_M(\Theta) = A_o + A_2P_2(\cos\Theta) + A_4P_4(\cos\Theta).$$

The best parameters A_i and the associated variance-covariance matrix are determined by linear regression. The function is then re-normalized so as to take the form

$$W_M(\Theta) = 1 + \alpha_2P_2(\cos\Theta) + \alpha_4P_4(\cos\Theta).$$

The variance associated with the normalized parameters is given by

$$v_i = \alpha_i^2 \quad \frac{\sigma_{oo}}{A_o^{\ 2}} + \frac{\sigma_{ii}}{A_i^{\ 2}} - \frac{2\sigma_{io}}{A_iA_o} \qquad i = 2,4.$$

As is well known, the measured correlation function is attenuated in comparison to the true function because of the finite angular response of the detectors (60). The finite solid angle effect can be described by attenuation coefficients G_2, G_4 so that

$$W_M(\Theta) = 1 + G_2\alpha_2P_2(\cos\Theta) + G_4\alpha_4P_4(\cos\Theta)$$

where α_2, α_4 are the true correlation parameters. The angular response of the detector $f(\Theta)$ may be measured observing the variation in counting rate with angle when a collimated gamma-ray beam is incident upon the detector. As shown by Rose (60) the attenuation factor for each detector is given by

$$J_i = \int_0^{2\pi} f(\Theta)\, P_i(\cos\Theta)\, \sin\Theta\, d\Theta.$$

The function $f(\Theta)$ is dependent upon the energy of the incident gamma ray. The variation of J_i with incident energy has been investigated by several authors (60,61,62) for the detector size of three inches and source distance of 10 cm used in this work. Since the effective solid angle subtended depends upon energy, the attenuation co-efficient for the full-energy peak of the spectrometer response is larger than that for the integrated response. The absolute values of J_i were determined for full-energy peaks corresponding to 0.662 and 1.33 MeV. It was assumed that the energy variation in J_i for the full-energy peaks is the same as that for the integrated response given in Reference (62). For a cascade comprised of gamma rays of energy E_1, E_2, the attenuation coefficients are given by

$$G_i = J_i(E_1)\, J_i(E_2).$$

The sources used for angular correlation studies were in the form of cylinders ~ 2 mm in length x 2 mm in diameter. These dimensions were considered sufficiently small with respect to the size of the detector and the source-to-detector distance so that corrections for finite source size were neglected.

5.7 A Philosophy of Decay-Scheme Studies

The advances in the techniques of nuclear pulse spectrometry has led to the increased use of relatively complex counting systems capable of rapidly acquiring a large volume of data. The experimenter is faced with the challenge of efficiently reducing the data to a relatively few physically meaningful numbers. This situation has forced a re-appraisal not only of the techniques of suitable analysis methods but of the general philosophy of decay-scheme studies. It is important to guide the efforts of data-reduction investigations with a basic and concise description of the overall problem. It is within this context that the concept of a regression model becomes important. The use of such a model provides a natural and convenient vector formulation which simply describes all the important measurements connected with the large volume of data collected.

The model consists of the basic set of gamma-ray and beta-particle transitions assumed to be emitted in the decay and their corresponding energies $E_1, E_2, \ldots E_n; W_1, W_2, \ldots W_r$. To be perfectly general the energies may be considered as first estimates. The problem then encompasses the non-linear iterative procedures required to include the energy as an independent variable. However, it is more convenient to consider the model in the more restrictive sense as including the precise energies as well as the number of each type of transition involved.

One-dimensional distributions are then linear combinations of the distributions of the individual components and are expanded in the representation in which the transitions assumed in the model constitute the basic set. The single-crystal gamma-ray and beta-particle spectra are simply described by the vectors $(\gamma_1, \gamma_2, \dots \gamma_n)$ and $(\beta_1, \beta_2, \dots \beta_r)$. Similarly, the two-dimensional distributions of time-correlated events are described by the n x n matrix (γ_{ij}) and the r x n matrix (β_{ij}) respectively. In some instances it may be necessary to extend the coincidence studies to three-fold coincidences, in which case the distribution is described by the array (γ_{ijk}).

Angular correlation studies and life-time studies can be considered from this viewpoint as investigations of the dependence of the appropriate matrices on angle or delay time viz $\gamma_{ij}(\theta)$ or $\beta_{ij}(t)$ etc.

In practice, of course, the model must be continually refined as new information is obtained. Once a reasonably accurate model has been constructed the convolution relation between the incident and measured spectrum is used together with statistical techniques to obtain estimates of the values of the parameters required and their associated variance. It is the opinion of this author that this approach is the most satisfactory in providing a didactic description of decay-scheme studies in general and in serving as a guide to the solution of rapid reduction of large volumes of data.

CHAPTER VI

EXPERIMENTAL RESULTS

6.1 Energy and Intensity of Gamma-Ray Transitions

A relatively complete catalogue of the gamma-ray transitions which occur in the beta decay of 92.6-min La^{142} was obtained by considering the results of many experiments. These include the single-crystal gamma-ray spectrum, the three-crystal pair spectrum and the coincidence spectra measured for several window settings. As has been described in the previous section, the procedure for evolving a consistent description of the spectrum involves a continual updating of the model used in the analysis as information is obtained. The results shown in this section represent the final analysis based upon a model considered to be relatively complete.

The single-crystal gamma-ray spectrum of La^{142} is shown in Figure 23. The Gaussian full-energy peaks of the spectral components of the spectrum are also shown. In order to avoid confusion the partial-energy portion of the response to each gamma ray has been omitted. The line shapes used for the analysis of spectra observed over the complete energy range were obtained from the library.

Secondary internal calibration lines were determined using the method of mixed sources. A $La^{142} - Na^{22}$ mixture was used to obtain the energies of the prominent lines in the region between 0.511 and 1.27

FIGURE 25

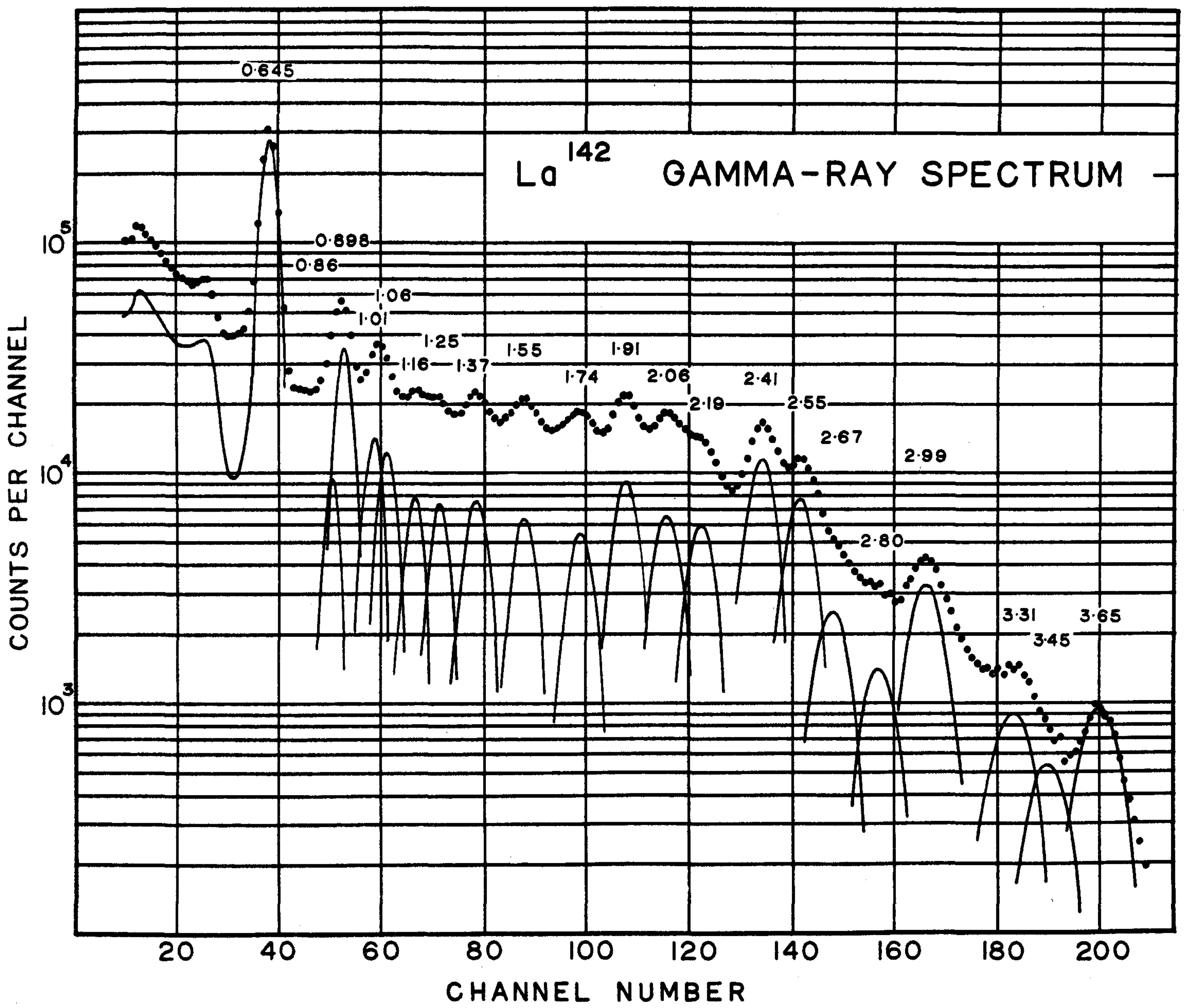
La^{142} GAMMA-RAY SPECTRUM
COUNTS PER CHANNEL
10^5
10^4
10^3
CHANNEL NUMBER
20
40
60
80
100
120
140
160
180
200
0·645
0·898
0·86
1·06
1·01
1·25
1·16
1·37
1·55
1·74
1·91
2·06
2·19
2·41
2·55
2·67
2·99
2·80
3·31
3·45
3·65

MeV. A La^{142} - Na^{24} mixture was used for the region between 1.3 and 2.8 MeV. As can be seen from Figure 23, the spectrum is complex and exhibits a strong line at 0.645 MeV. This line, together with the less prominent lines at 1.91, 2.41 and 2.55 MeV were adopted as secondary standards. Although as shown in Section 4.5, the energy pulse-height relation is not linear, the assumption of a linear relation was used together with the following procedure. The positions of the secondary standards were determined by calculating the centroids of the full-energy peaks. The gain and zero-energy channel were considered as parameters of the linear relation and their best values obtained from the internal standards by the method of least squares. A comparison of the values obtained in this manner indicated that over the energy range of 0.6 - 3.0 MeV, the neglect of the non-linearity in the dispersion relation introduces an error of less than 0.2%. The error is, of course, mainly absorbed in the zero channel parameter and the method would not be as accurate in the energy region below approximately 0.5 MeV where the non-linearity is more serious. The accuracy with which the position of the full-energy peak can be determined depends upon the magnitude of the interfering contributions from partial-energy events corresponding to higher-energy gamma rays. The energies of the remaining gamma rays in the spectrum were determined using the positions of the full-energy peaks of the analyzed components and the fitted dispersion relation appropriate to all other experiments and the energies recalculated in each experiment. In this way the experiments were checked for consistency and the values obtained were averaged with the existing values.

Unfortunately, it was impossible to obtain standard line shapes corresponding to incident gamma-ray energies greater than 3.1 MeV. It was necessary to construct line shapes for the analysis of this energy region of the La^{142} spectrum by extrapolation. The contribution from summing was measured for the 10-cm geometry used by the method discussed in Section 4.8. The sum contribution was never greater than 5% of the gross spectrum so that the subtraction of this contribution introduced a negligible uncertainty. As can be seen from Figure 23, there is a departure of the data on the high-energy side of the 3.65-MeV full-energy peak. Although this line shape was based on an extrapolation procedure, it is felt that the error in the response is small compared to the observed deviation. However, since the existence of any transition of energy greater than 3.65 MeV was not revealed in the course of this study, it is concluded that a small residual remains.

A residual in the region of 3.1 MeV revealed the existence of a weak transition at this energy. However, it was not possible to obtain sufficient information about the transition to include it in the decay scheme. The existence of the 2.67-MeV gamma ray, revealed in the stripping, was first suggested by Heath (24) and confirmed in this investigation by coincidence results. Other evidence which will be cited later in this chapter also confirmed the existence of all the components shown in Figure 23 which were revealed by graphical analysis. The analyses of the 1.01 - 1.05 MeV and 0.86 - 0.898 MeV doublets were particularly difficult. Initially it was merely noted that the widths of these lines were somewhat broadened. The lower energy region of the spectrum was analyzed separately using the distribution measured with a higher gain. In this case, the required line shapes were obtained from measurements of the spectra of Cs^{137} (0.662 MeV), Mn^{54} (0.835 MeV) and Zn^{65} (1.114 MeV) performed immediately after the run so that similar counting conditions applied. The contribution from higher energy gamma rays was calculated on the basis of the analysis of the spectrum in Figure 23. Careful graphical analysis of the high gain spectrum led to the relative contributions for the components of these doublets as shown in Figure 23.

The relative intensity of each component of the spectrum was calculated using the area of the full-energy peak corrected for photo efficiency. The correction factors given by Heath (63) were used. Except in the region of 1.37 MeV, all portions of the spectrum were observed to decay with the 92.6-min half life corresponding to La^{142}. The 1.37-MeV transition was found to consist of approximately equal contributions of 92.6-min La^{142} and 3.7-hr La^{141} over the counting period used.

Using a design matrix based upon the results of the graphical analysis, the spectrum was analyzed by the method of multiple linear regression. The regression values, the corresponding variance-covariance matrix and the variance ratios were determined. The variance ratios indicated that each component (including the 3.1 MeV line) was statistically significant, exceeding the 95% confidence limit. Of course, the existence of a residual not taken into account in the design matrix would invalidate definite conclusions based on the variance ratios. The differential residual indicated no significant trends and the effective value of χ^2 for the model used was 1.8. This rather large value is believed to be caused mainly by inaccuracies in the line shapes, especially the positioning of the full-energy peaks in the region between 1 and 2 MeV. The results obtained by graphical analysis and linear regression are shown in Table IV. Except for the less prominent lines, the results of the two methods agree within 15% and usually within the standard deviation.

As mentioned above, the existence of weak transitions, though confirmed statistically, was still considered tentative until further experimental evidence proved conclusive. One source of such evidence concerning the transitions in the region above approximately 1.5 MeV is the three-crystal pair spectrum shown in Figure 24. Because of the superior resolution and the simplified response, the more obscure transitions in the single-crystal spectrum are more clearly revealed. A definite peak is seen at 2.80 MeV. The 2.67 MeV line appears just barely resolved on the high energy side of the 2.54 MeV peak. Because of the low intensity, the 3.45 MeV line is still not very prominent, but its existence is indicated.

The residual on the high-energy side of the 2.99 MeV peak also indicates the possible existence of the transition at 3.1 MeV referred to above. The peaks corresponding to the 2.05- and 2.18-MeV transitions are clearly resolved, in contrast to the corresponding peaks in the single-crystal spectrum. However, the valley between these two peaks is higher than expected on the basis of the resolution and energy separation indicating the possible existence of a weak transition at 2.1 MeV. The energies of the gamma transitions revealed in the three-crystal pair spectrum were found to agree with the corresponding energy values determined from the single-crystal spectrum within the experimental error of 1%. The intensities of the transitions relative to

FIGURE 24

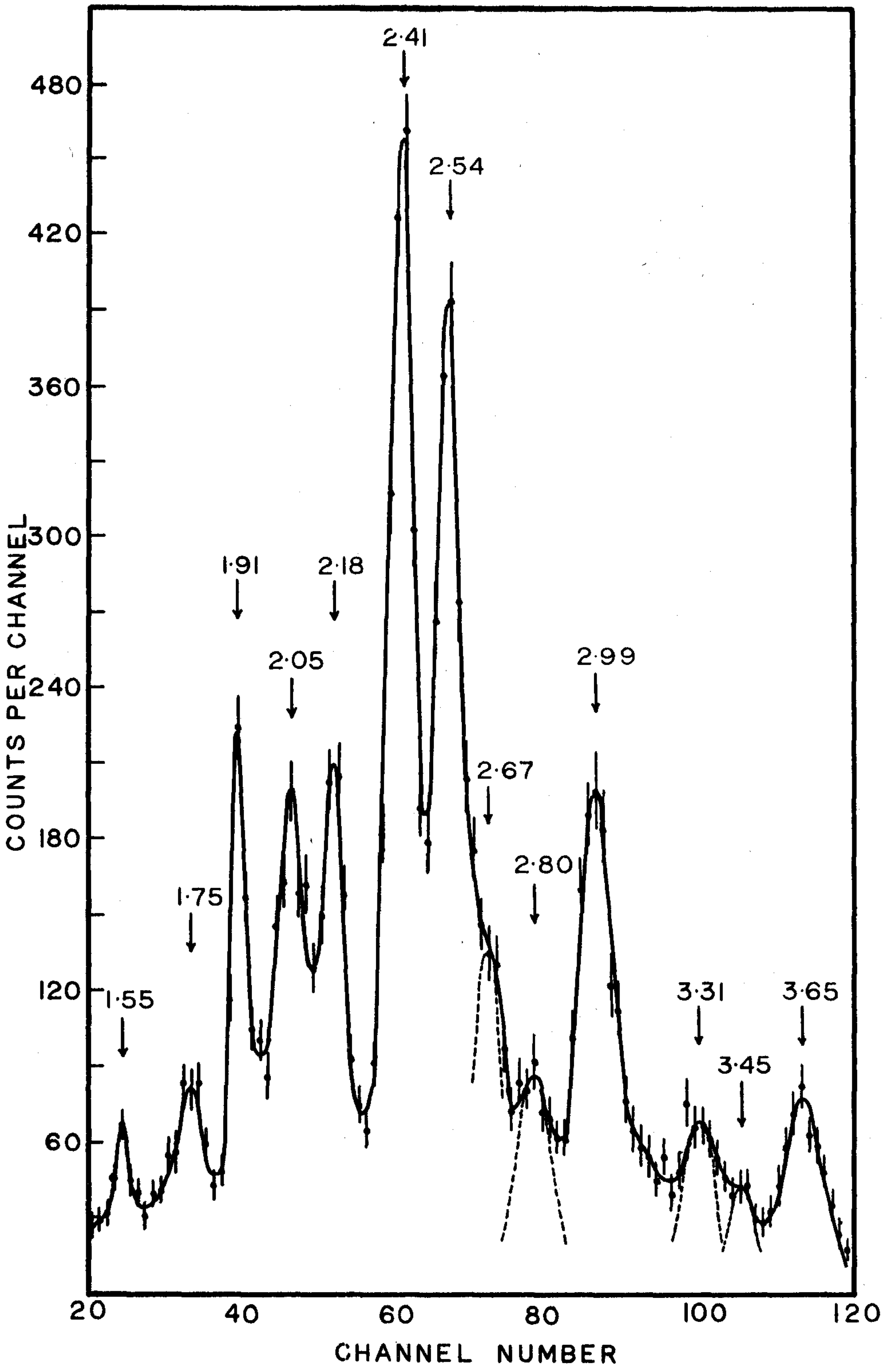

COUNTS PER CHANNEL
480
420
360
300
240
180
120
60
20
40
60
80
100
120
CHANNEL NUMBER
2·41
2·54
1·91
2·18
2·05
2·99
2·67
2·80
1·75
1·55
3·31
3·45
3·65

TABLE IV

Summary of La^{142} Gamma-Ray Transitions

E_γ (MeV)	Relative Intensity				
	Graphical Analysis	Regression	Pair Spectrometer	Coincidence	Average
0.645 ± 0.007	1.000	1.000			1.000
0.86 ± 0.01	0.049	0.056 ± 0.006		0.044	0.050
0.898 ± 0.009	0.19	0.194 ± 0.006		0.17	0.185
1.01 ± 0.01	0.10	0.091 ± 0.005		0.090	0.094
1.06 ± 0.01	0.085	0.076 ± 0.007		0.071	0.077
1.16 ± 0.01	0.066	0.060 ± 0.012		0.051	0.059
1.25 ± 0.01	0.064	0.060 ± 0.015		0.048	0.057
1.37 ± 0.01	0.039	0.049 ± 0.004		0.063	0.050
1.55 ± 0.02	0.081	0.100 ± 0.004	0.11	0.055,0.045	0.053,0.044
1.74 ± 0.02	0.097	0.107 ± 0.004	0.12	0.101	0.106
1.91 ± 0.17	0.17	0.171 ± 0.005	0.21	0.151	0.176
2.06 ± 0.02	0.13	0.137 ± 0.004	0.15	0.11	0.132
2.14 ± 0.04	0.15	0.130 ± 0.004	0.15	0.04	0.044
2.19 ± 0.02				0.09	0.099
2.41 ± 0.02	0.31	0.318 ± 0.006	0.318*		0.314
2.55 ± 0.02	0.22	0.229 ± 0.005	0.23		0.227
2.67 ± 0.03	0.06	0.073 ± 0.004	0.07	0.040	0.061
2.80 ± 0.03	0.05	0.044 ± 0.003	0.05	0.039	0.046
2.99 ± 0.03	0.12	0.130 ± 0.003	0.10	0.091	0.11
3.14 ± 0.04		0.031 ± 0.004	0.02		0.026
3.31 ± 0.03	0.04	0.038 ± 0.003	0.04		0.039
3.45 ± 0.03	0.03	0.029 ± 0.002	0.02		0.026
3.65 ± 0.04	0.05	0.054 ± 0.002	0.04		0.048

*The relative intensity of this line was normalized to the corresponding single-crystal value.

that of the 2.41-MeV transition were obtained by determining the peak areas corrected for the pair-production cross section. The values obtained are compared to the single-crystal values in Table IV. Also shown in the table are the intensity measurements obtained from coincidence studies. These measurements are based on an interpretation of the coincidence quotients within the context of the proposed decay scheme.

6.2 Gamma-Gamma Coincidence Studies

Coincidence spectra were observed with the fast-slow coincidence spectrometer and the two-dimensional spectrometer. Only the spectra obtained with the fast-slow system are shown in the illustrations. Each of these spectra was analyzed graphically. The results obtained with the two-dimensional system were in agreement with those obtained with the fast-slow system. The results quoted are the averages of several experiments.

The spectrum shown in Figure 25 is the distribution of events in coincidence with gating events selected by a window 0.05-MeV wide centered at 0.645 MeV. Events in this region correspond primarily to the 0.645 MeV transition. The coincidence spectrum obtained extends to the line at 2.99 MeV. Analysis revealed the existence of the 2.80- and 2.67 MeV lines. The region between 2.2 and 2.5 MeV was not entirely accounted for by the response to these three gamma rays, but because of the expected higher levels of interference as discussed in Section 4.5, the residual was not considered to definitely indicate the existence of gamma transitions in this region. The energy of the transition at 2.14 MeV was consistently observed to be lower than the corresponding

FIGURE 25

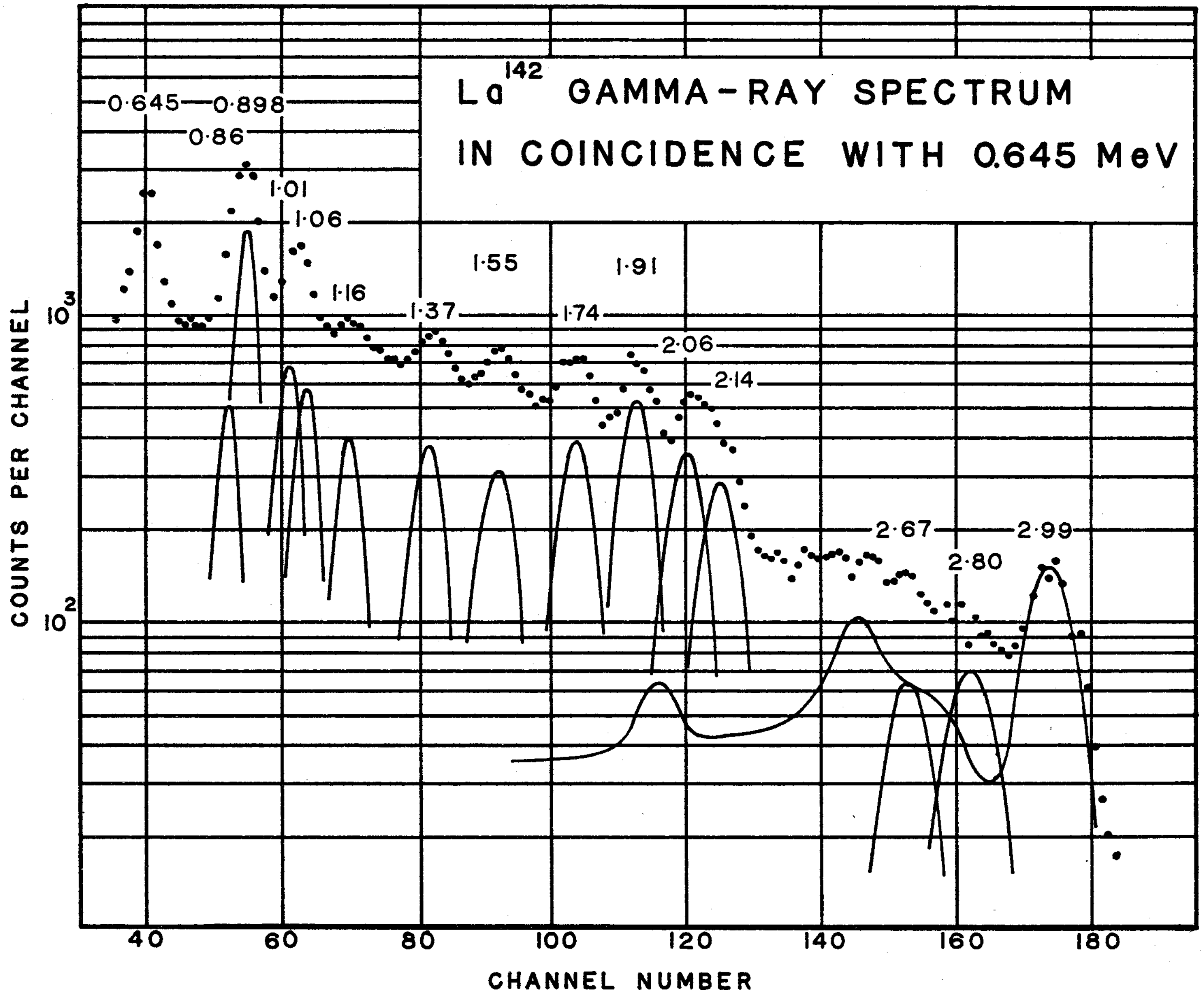
La^{142} GAMMA-RAY SPECTRUM
IN COINCIDENCE WITH 0.645 MeV
0·645
0·898
0·86
1·01
1·06
1·16
1·37
1·55
1·74
1·91
2·06
2·14
2·67
2·80
2·99
COUNTS PER CHANNEL
10^3
10^2
40
60
80
100
120
140
160
180
CHANNEL NUMBER

transition at 2.18 MeV present in the single crystal and pair spectrum. This result, together with the anomalous residual at 2.1 MeV in the pair spectrum, is believed to indicate that the transition at this energy is complex. The coincidence-quotient analysis indicates that approximately 60% of the transitions at this energy are in coincidence with events in the window. Below 2 MeV, the spectrum is similar to the single-crystal gamma-ray spectrum. However, only 45% of the transitions at 1.54 MeV and 63% of the transitions at 1.37 MeV appear in coincidence with the 0.645-MeV gamma ray. As mentioned in the previous section, the 1.37-MeV line is attributable to both La^{142} and La^{141}, so that this result indicates that approximately 37% of the transitions at this energy in the spectrum shown in Figure 23 are due to La^{141}. Further evidence from the coincidence experiments indicate that the 1.54-MeV peak corresponds to two unresolved gamma rays. The 0.645-MeV line which appears in the spectrum is caused by events in the gate corresponding to higher energy gamma rays.

The interference from such events was both treated analytically as outlined in Section 5.4 and measured experimentally. In the latter case, windows were set both at 0.645 MeV and 0.76 MeV. Both distributions were sampled concurrently and routed into different subgroups of the memory. There was no significant difference between the results obtained experimentally and analytically.

The low-energy region of this spectrum was also investigated experimentally using a higher gain. Line shapes measured immediately after the run were used to analyze the spectrum. In agreement with the single-crystal data, the analysis revealed the complex nature of the 1.01 - 1.06 MeV and 0.860 - 0.898 MeV doublets.

In Figure 26a is shown the spectrum obtained for a window position of 0.88 MeV and width 0.05 MeV. Only 50% of the gating events at this position correspond to the gamma rays of interest, 0.860 - 0.898 MeV. The spectrum is characterized by an enhancement of the 1.16-MeV line and a broadening of the 0.860 - 0.898 MeV doublet. The previous authors (23) suggested that the 1.0-MeV line was in coincidence with the 0.898-MeV transition. However, the coincidence quotient $q_{0.898,1.0}$ is nearly zero so that the appearance of the 1.0-MeV line in this spectrum is due to Compton interference. This result was confirmed in the corresponding two-dimensional distribution. The coincidence quotients for the 0.860 - 0.898 MeV doublet indicate that these transitions are members of a cascading pair. There is a considerable residual in the region above 1 MeV. The coincidence quotient for the 1.55 MeV peak, taken to be correlated with the 0.860-MeV component of the window, accounts for the 55% portion not in coincidence with the 0.645-MeV transition. The doublet at ~ 2 MeV accounts for approximately 30% of the single-crystal intensity. The low-energy region of the spectrum was observed at a higher gain and the results of the graphical analysis are illustrated in Figure 26a.

In Figure 27 is shown the coincidence spectrum obtained when a region of 0.05 MeV centered at 1.03 MeV is selected for gating. The gating fractions $D_{1.01}$ and $D_{1.06}$ are 25% and 24% respectively. The most prominent feature of the spectrum is the enhancement of the 1.01 - 1.06 MeV doublet. The 0.898-MeV line is suppressed and the small coincident quotient confirms the fact that the major part of the 0.898-MeV and 1.03 MeV transitions are not correlated. As in the case of the 0.898-MeV coincidence spectrum, there is a considerable residual

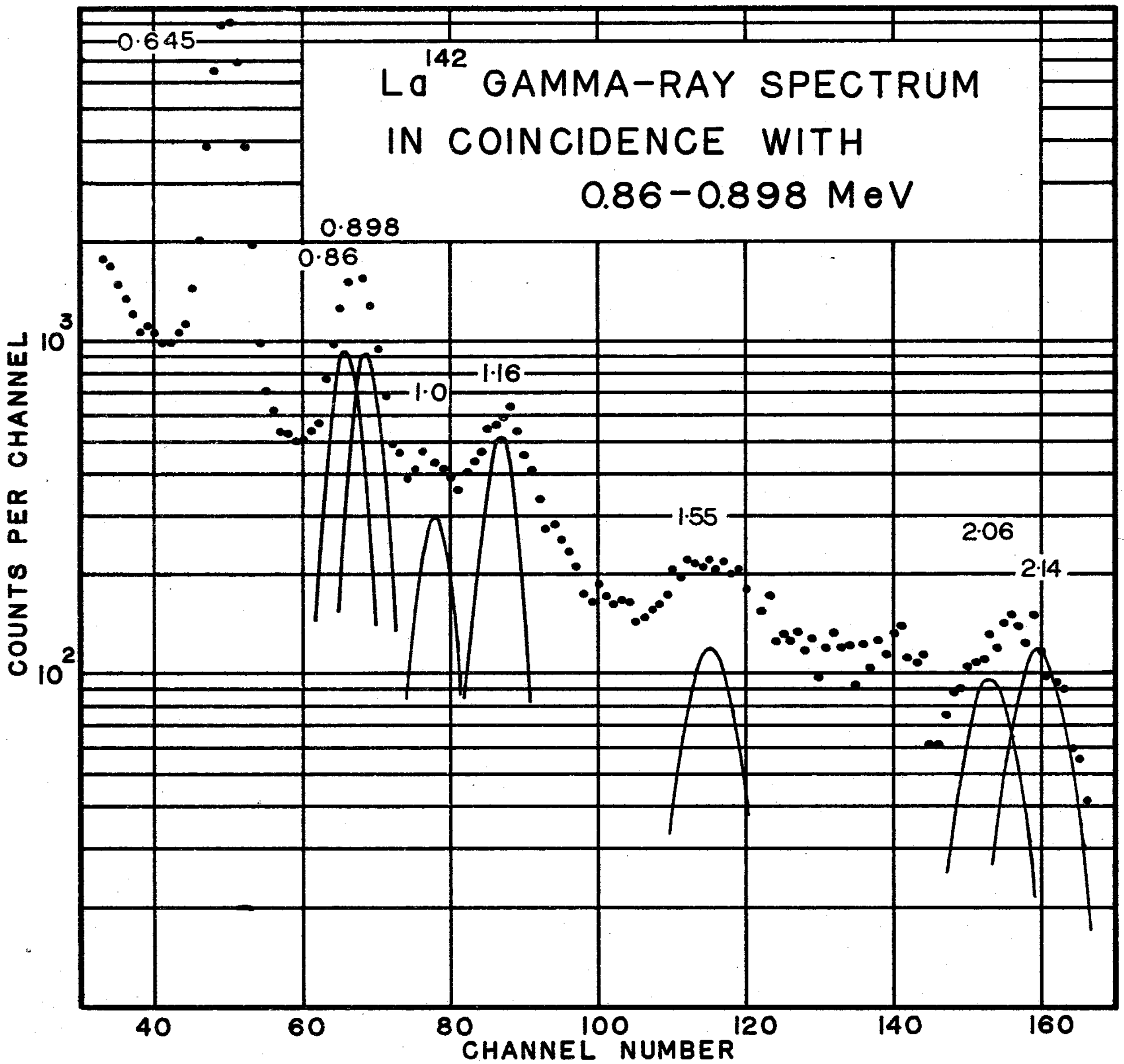
La^{142} GAMMA-RAY SPECTRUM
IN COINCIDENCE WITH
0.86–0.898 MeV
COUNTS PER CHANNEL
10^3
10^2
CHANNEL NUMBER
40
60
80
100
120
140
160
0·645
0·898
0·86
1·0
1·16
1·55
2·06
2·14

FIGURE 26 (a)

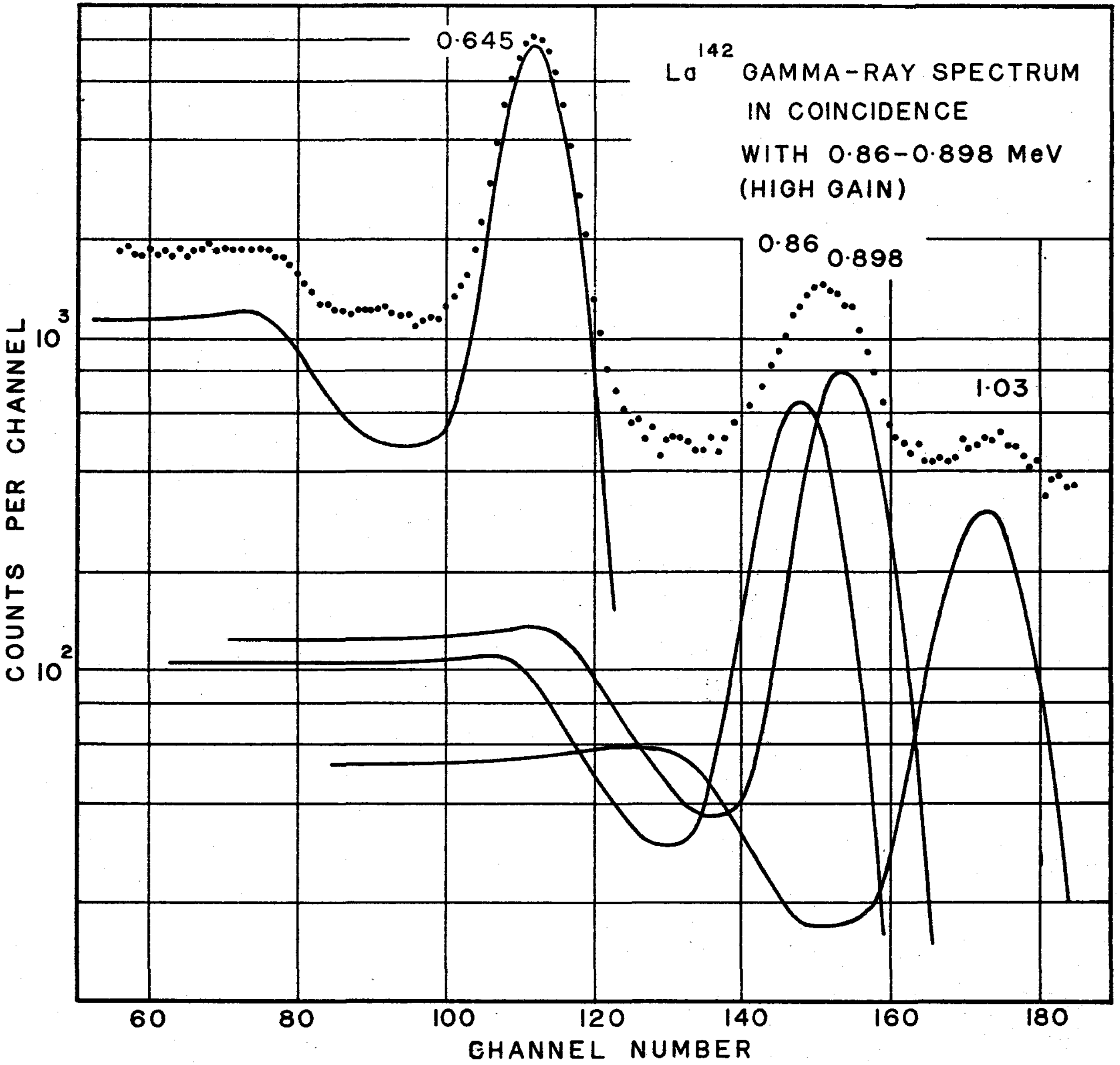
0·645
La^142 GAMMA-RAY SPECTRUM
IN COINCIDENCE
WITH 0·86–0·898 MeV
(HIGH GAIN)
0·86
0·898
1·03
COUNTS PER CHANNEL
10^3
10^2
60
80
100
120
140
160
180
CHANNEL NUMBER

FIGURE 26 (a)

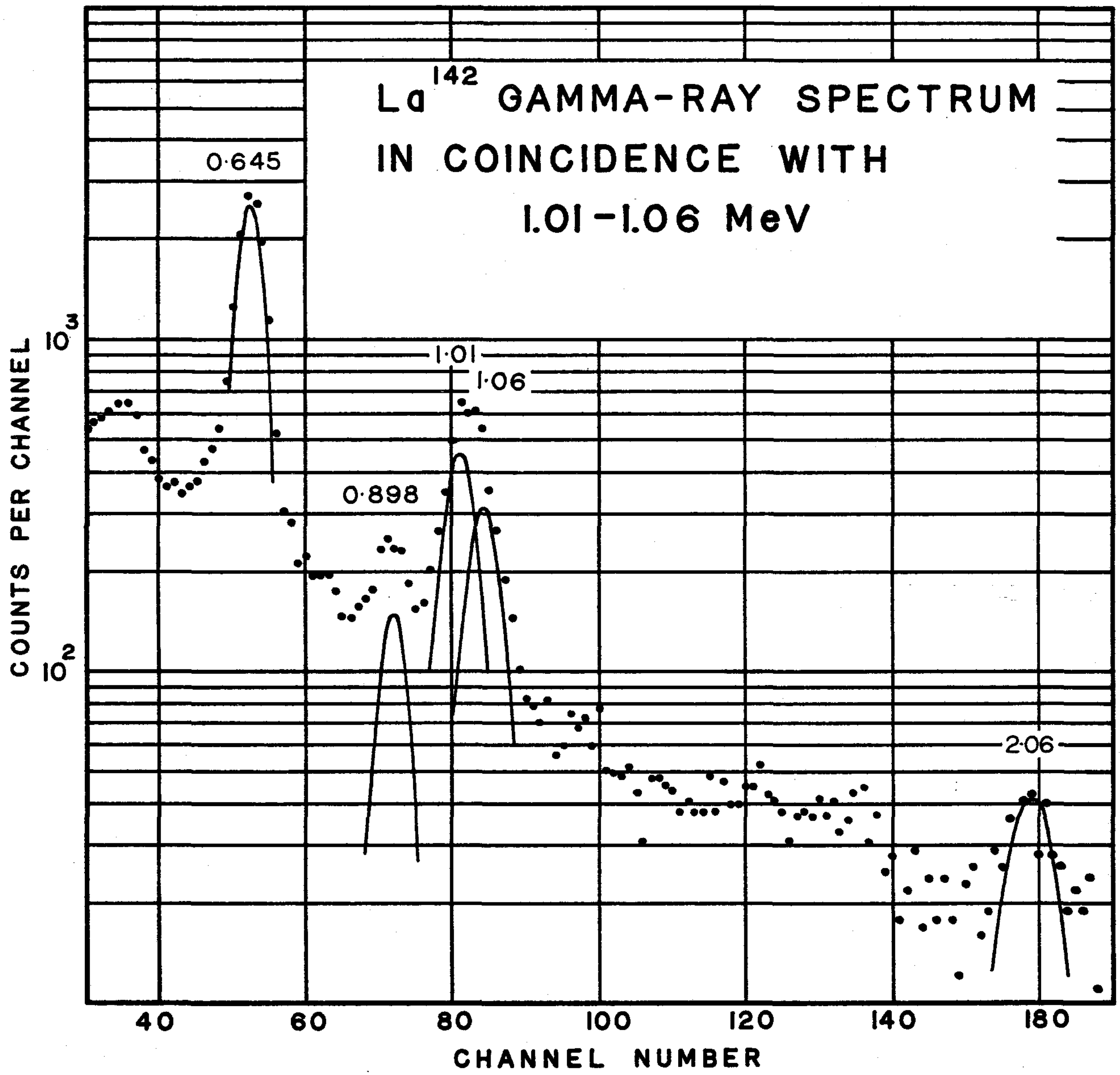
La^{142} GAMMA-RAY SPECTRUM
IN COINCIDENCE WITH
1.01-1.06 MeV
0·645
1·01
1·06
0·898
2·06
COUNTS PER CHANNEL
10^3
10^2
40
60
80
100
120
140
180
CHANNEL NUMBER

FIGURE 27

above 1.2 MeV, only a part of which can be accounted for by the response to the 2.06-MeV gamma ray. The coincidences at 2.06 MeV comprise approximately 30% of the corresponding single-crystal intensity. In Figure 28 is shown the low-energy region of this spectrum observed at higher gain. The analysis was based on the appropriate line shapes measured immediately after the run. The results confirm the doublet nature of the 1.03-MeV peak. The relative contributions of the 1.01- and 1.06-MeV components obtained in this analysis differ from the corresponding results obtained in the analysis of the spectrum shown in Figure 27. This difference reflects the difficulties inherent in the graphical analysis of doublets. The ratio obtained from the spectrum shown in Figure 28 is believed to be more accurate both because the line shapes used in the analysis were obtained under the same counting conditions and because of the finer mesh resulting from increased gain.

In Figure 29 is shown the distribution of events in coincidence with gating pulses selected by a 0.06-MeV window centered at 1.25 MeV. For this window setting only 27% of the gating pulses correspond to the 1.25-MeV gamma ray. The most striking feature of the spectrum is the enhancement of the 1.55-MeV and 2.19-MeV peaks. The coincidence-quotient analysis indicates that these transitions are both in coincidence with the 1.25-MeV gamma ray. The coincidences at 2.19 MeV correspond to approximately 80% of the single-crystal intensity so that the doublet nature of this peak appears to be approximately 75% 2.19 MeV and 25% 2.14 MeV.

The intensity of the 1.55-MeV transition in coincidence with the 1.25-MeV gamma ray is 55% of the single-crystal intensity. This is in reasonable agreement with the 0.645 MeV result of 59%. The 1.25-MeV

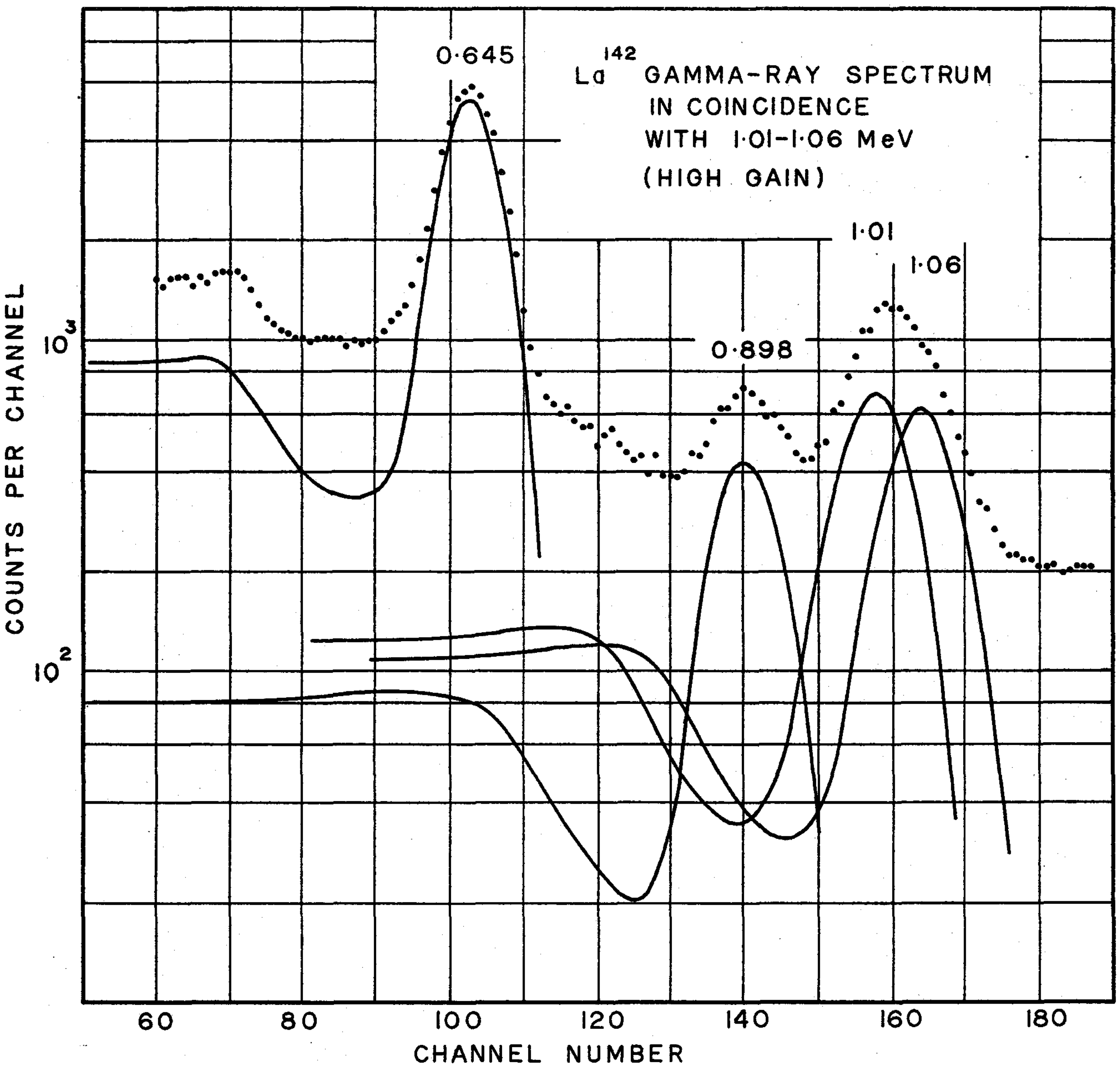
0·645
La^{142} GAMMA-RAY SPECTRUM
IN COINCIDENCE
WITH 1·01-1·06 MeV
(HIGH GAIN)
1·01
1·06
0·898
COUNTS PER CHANNEL
10^3
10^2
60
80
100
120
140
160
180
CHANNEL NUMBER

FIGURE 29

FIGURE 29

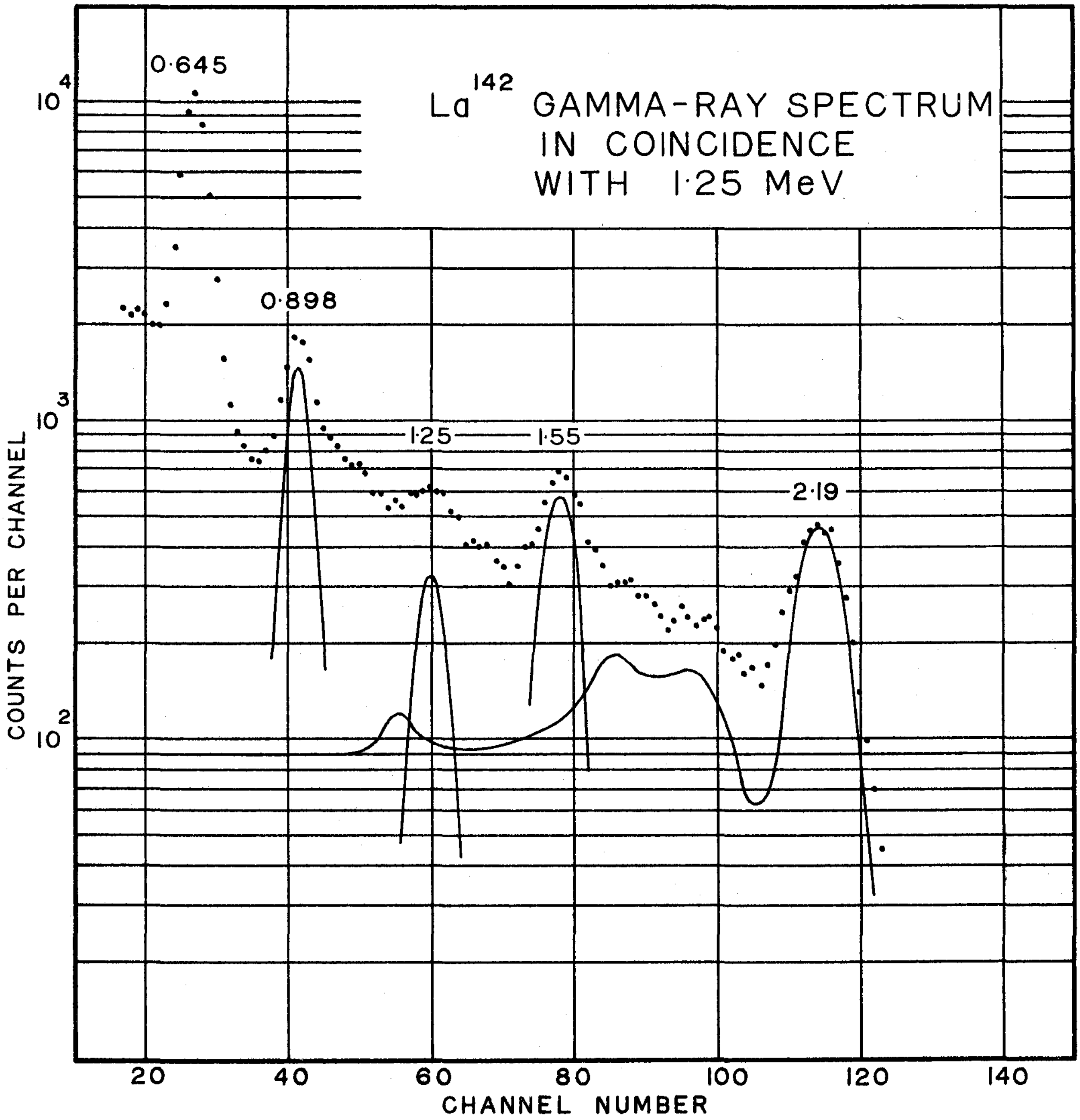
La^{142} GAMMA-RAY SPECTRUM
IN COINCIDENCE
WITH 1·25 MeV
0·645
0·898
1·25
1·55
2·19
10^4
10^3
10^2
COUNTS PER CHANNEL
20
40
60
80
100
120
140
CHANNEL NUMBER

and 0.898-MeV peaks are predominantly due to Compton interference. The 0.645-MeV transition is assigned to be in coincidence with the 1.25-MeV gamma ray on the basis of the analysis.

The gamma-ray spectrum in coincidence with gating pulses selected by a window 0.06-MeV wide centered at 1.55 MeV is shown in Figure 30. In this spectrum the 1.25-MeV peak is prominent, confirming the existence of the 1.25 - 1.55 MeV cascade. The coincidence-quotient analysis also confirms the existence of the 0.645 - 1.55 MeV cascade. The rest of the lines in the spectrum result mainly from gating events not due to the 1.55-MeV transition. This transition comprises only 21% of all the events in the window.

In Figure 31 is shown the distribution in coincidence with gating events selected with a broad window covering the range 2.0 - 2.2 MeV. As in the case of the 1.55-MeV coincidence spectrum, the 1.25-MeV line is strongly enhanced, confirming the 1.25 - 2.19 MeV coincidence relation. The 0.645-MeV line is mainly the result of 2.06 - 0.645 MeV coincidences. In calculating the coincidence quotients, analysis of the contributions to the window was based on the single crystal and coincidence data. The gating fractions for the gamma rays of interest are $D_{2.06} = 0.25$, $D_{2.14} = 0.06$ and $D_{2.19} = 0.18$. The corrections for Compton interference were made analytically. In addition, an estimate of the interference was obtained experimentally by comparing this spectrum with the spectrum in coincidence with the window set at 2.5 MeV. The appearance of the 0.898- and 1.55-MeV transitions is further evidence for the coincidence relationships 0.898 - 2.14 MeV and 1.55 - 2.14 MeV.

FIGURE 30

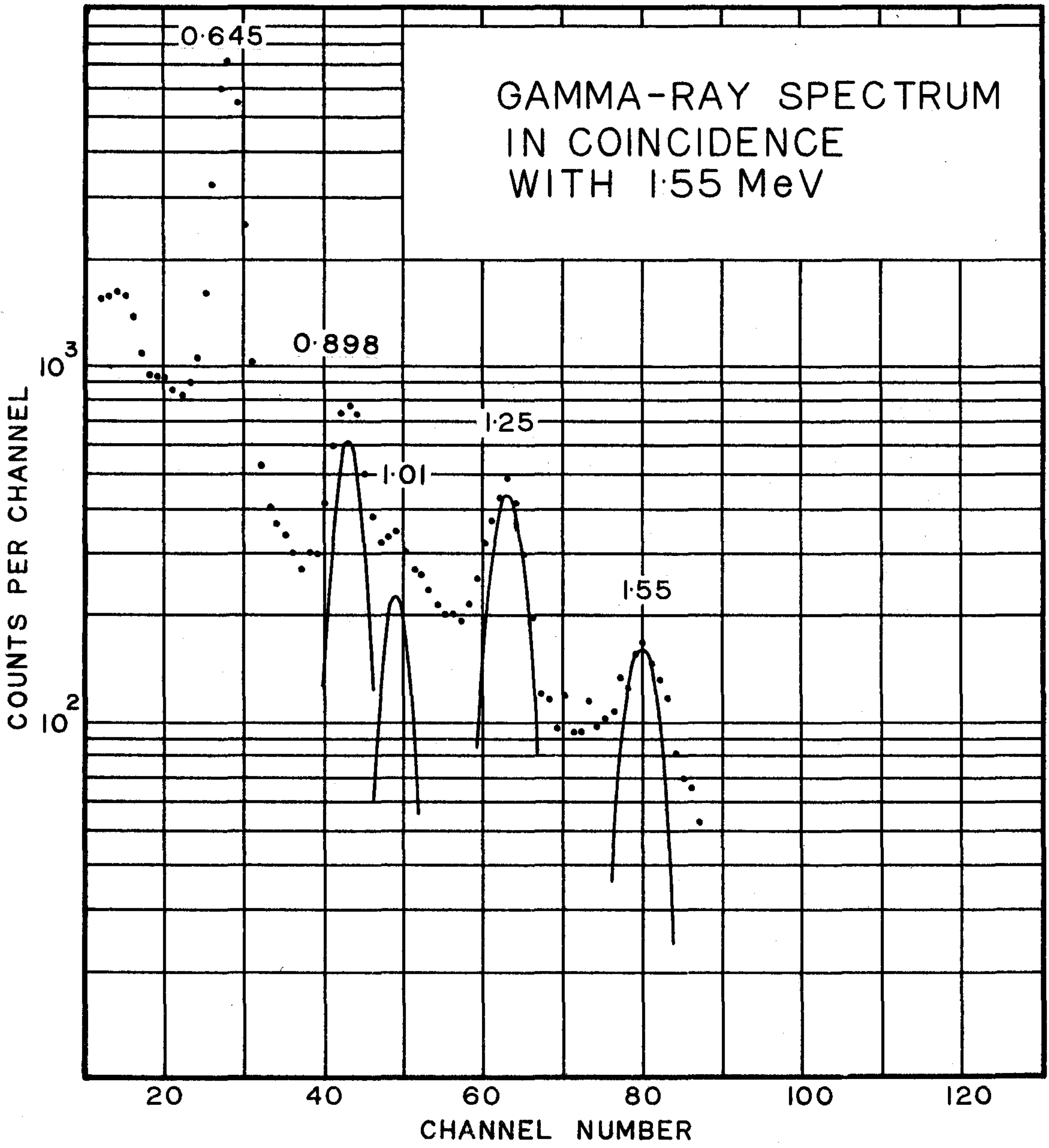
GAMMA-RAY SPECTRUM
IN COINCIDENCE
WITH 1·55 MeV
0·645
0·898
1·01
1·25
1·55
10^3
10^2
COUNTS PER CHANNEL
20
40
60
80
100
120
CHANNEL NUMBER

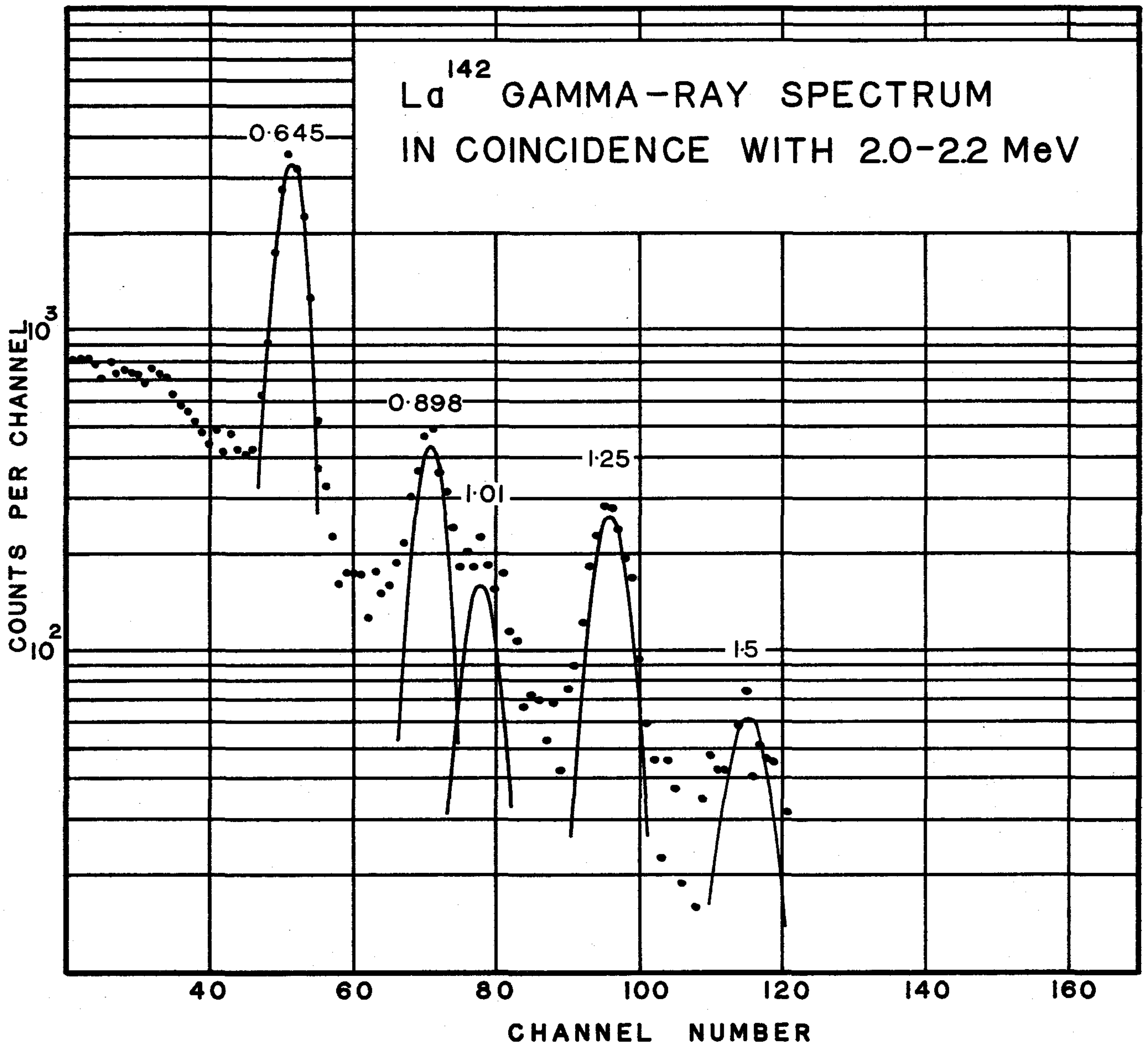
La^{142} GAMMA-RAY SPECTRUM
IN COINCIDENCE WITH 2.0-2.2 MeV
0·645
0·898
1·01
1·25
1·5
COUNTS PER CHANNEL
10^3
10^2
40
60
80
100
120
140
160
CHANNEL NUMBER

[illegible]

With windows set at the energies 1.74, 1.91, 2.67 and 2.99 MeV, only coincidences with the 0.645-MeV line were identified. The coincidence quotients are given in Table V. The results indicate that these transitions are in coincidence with the 0.645-MeV gamma ray with full intensity to within the expected accuracy of 15%, except in the case of the 2.67-MeV experiment. The errors might be larger than normal in this case since this line is of low intensity and the Compton interference in the window is large.

The low-energy region, 0.5 - 1.5 MeV, of the spectrum was also measured using the two-dimensional analyzer. In addition to confirming the corresponding results obtained with the fast-slow coincidence spectrometer, the data was also used to obtain the coincidence spectrum correlated with the 1.16-MeV gamma ray. The results confirm the coincidence relationships between the 1.16 - 0.645 MeV and 1.16 - 0.898 MeV gamma rays. Other two-dimensional spectra were obtained using various analyzer configurations. The average coincidence-quotient matrix is given in Table V. The summary of relative-intensity measurements based on this matrix and the proposed decay scheme is given in Table IV.

The intensity values obtained from the coincidence data are in relatively good agreement with the values obtained by other methods. The results are expected to have large errors in many instances. The method of coincidence-quotient analysis, because of the successive subtractions involved, tends to accumulate errors. In addition, the higher levels of interference mentioned previously in Section 4.5 lead to a large uncertainty in the results. The average values which combine measurements derived from spectra observed under several different conditions are generally considered to be accurate to 15%.

TABLE V

La^{142} Coincidence Quotient Matrix

	Energy of "Gating" Ray (MeV)														
E$_\gamma$(MeV)	0.645	0.86	0.898	1.03	1.16	1.25	1.37	1.55	1.74	1.91	2.06	2.14	2.19	2.67	2.99
0.645			1.05	0.95	0.86	0.63	0.89	0.85	1.2	1.1	0.78			0.62	0.85
0.86	0.04		0.26												
0.898	0.17	1.07		0.03	0.75	0.28		0.24				0.42			
1.01	0.06		0.03	0.97				0.09			0.06				
1.06	0.05		0.02	0.76											
1.16	0.052		0.26												
1.25						0.02		0.39					0.35		
1.37	0.063														
1.55	0.059	0.2				0.47		0.14				0.01			
1.66							0.11								
1.74	0.10														
1.91	0.15														
2.06	0.11		0.08	0.32											
2.14	0.09		0.12												
2.19						0.79									
2.67	0.030														
2.80	0.039														
2.99	0.091														

6.3 Sum Coincidence Studies

The sum-coincidence spectrum was obtained at a source-to-detector distance of 3 cm. The prominent sum peaks observed in the spectrum are listed in Table VI. The individual components of the sum peaks, also given in the table, were determined experimentally. Both the one-dimensional analyzer and pulse-height selector and the two-dimensional analyzer systems were used. When the component sum-coincidence spectra were determined using the two-dimensional analyzer, the sum distribution was assigned to one-dimension and the component spectra to the other. In Figure 32 is shown the component distribution corresponding to the 1.54-MeV sum peak. The spectrum is seen to consist essentially of only 0.645- and 0.898 MeV components. Interference from the 0.860-MeV transition is reduced as compared to the normal 0.645-MeV coincidence spectrum because of the more selective sum condition. The decay configuration relevant to this sum is also shown in the figure.

Figure 32 also illustrates the component spectrum obtained when a sum energy of 2.06 MeV is selected. In general, the component spectra corresponding to a given sum energy must be comprised of an even number of components. The result shown in Figure 32 thus confirms the existence of the cascades 0.898 - 1.16 MeV and 1.01 - 1.06 MeV, the latter forming a coincidence doublet. The same type of result was obtained for the 0.861 - 0.898 MeV doublet cascade. In this case the component spectrum consisted of only one peak at an energy of approximately 0.87 MeV when the sum-energy 1.74 MeV was selected. These examples suffice to indicate the simplification of the spectra obtained using the sum-

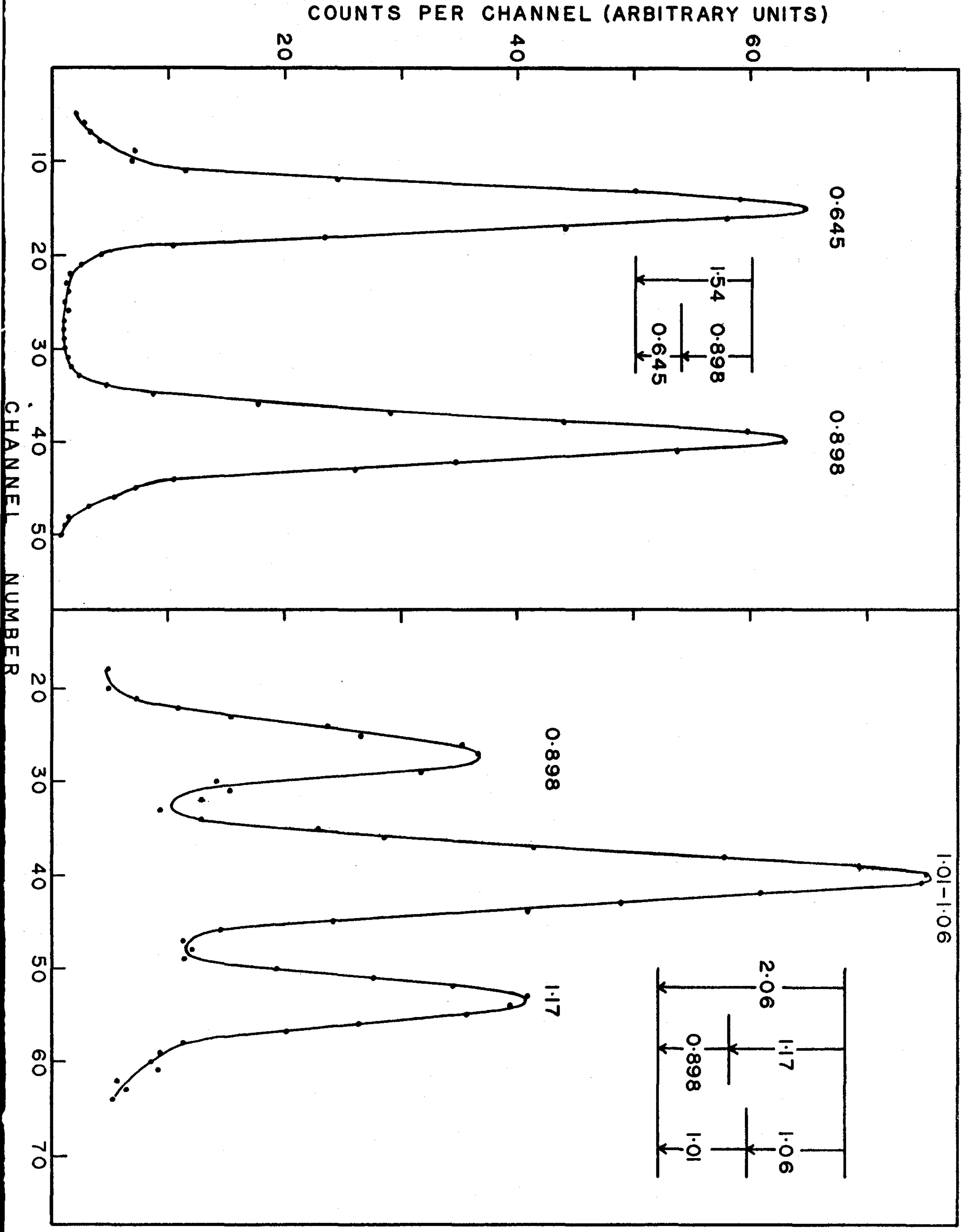
COUNTS PER CHANNEL (ARBITRARY UNITS)
20
40
60
CHANNEL NUMBER
10
20
30
40
50
20
30
40
50
60
70
0·645
0·898
1·54
0·898
0·645
0·898
1·01–1·06
1·17
2·06
1·17
0·898
1·06
1·01

FIGURE 32

TABLE VI

La^{142} Summary of Sum-Coincidence Results

Sum Energy (MeV)	Component Energy (MeV)
1.54	0.645 + 0.898
1.72	0.645 + 1.01, 1.06; 0.898 + 0.86
2.06	0.898 + 1.16; 1.01 + 1.06
2.4	0.645 + 1.74
2.6	0.645 + 1.91; 0.645 + 2.06
3.65	0.645 + 2.99

coincidence method. A summary of the sum-coincidence results is given in Table VI.

6.4 Beta Transitions

The beta radiations emitted in the decay of La^{142} were studied using the beta-ray scintillation spectrometer discussed in Section 4.5. Each spectrum obtained using this method was corrected for the finite response of the spectrometer. In addition, the single-crystal spectrum was measured with an anti-coincidence spectrometer (51) for which only the Gaussian resolution correction was required. Coincidence spectra were measured using the plastic scintillator and a three-inch NaI(Tl) gamma-ray detector in conjunction with the two-dimensional analyzer.

In Figure 33 is shown the single-crystal beta spectrum in the region above 2.5 MeV. The energy calibration was determined using as standard beta sources Cl^{38} (4.81 MeV), Ru^{106} - Rh^{106} (3.53 MeV), Ce^{144} - Pr^{144} (2.98 MeV) and Sr^{90} - Y^{90} (2.23 MeV). The Kurie analysis of the spectrum, assuming an allowed shape for each component, revealed the existence of beta groups at 4.5 and 3.9 MeV. The experiment was repeated several times using both the anti-coincidence spectrometer and the single-crystal arrangement. The spectrum given in Figure 33 is a composite of the spectra obtained with both methods. As mentioned in Section 4.5, it was considered preferable to combine the results from several runs in those cases where insufficient counting statistics were obtained rather than to use increased source strength for which significant contributions from random summing occur. Each run was calibrated independently and the channel numbers were converted to

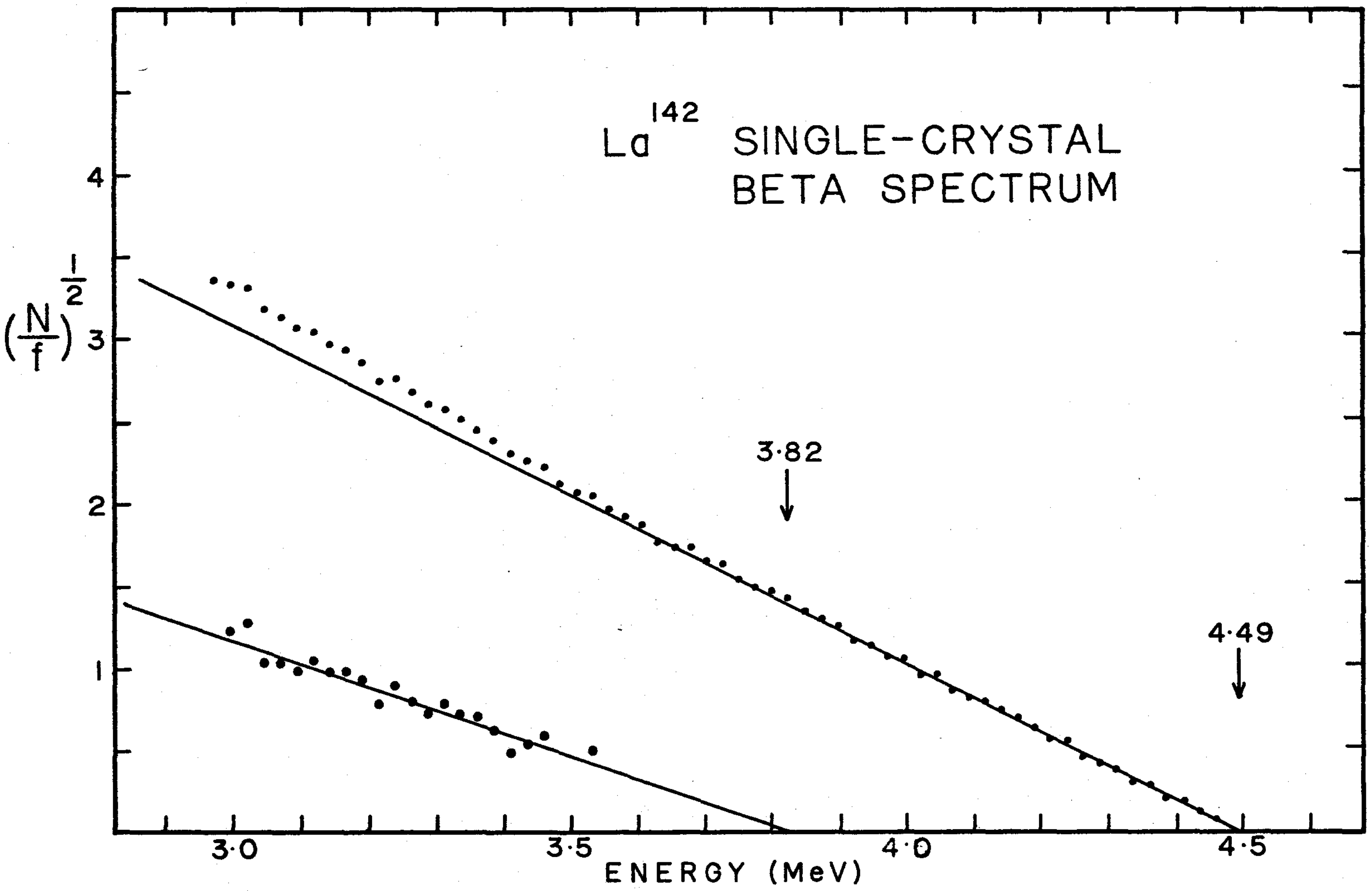
La^{142} SINGLE-CRYSTAL BETA SPECTRUM
$\left(\frac{N}{f}\right)^{\frac{1}{2}}$
1
2
3
4
3·0
3·5
4·0
4·5
ENERGY (MeV)
3·82
4·49

FIGURE 33

energy values. The single-crystal spectra were corrected for finite response. The results were averaged by adding together all the counts in a given energy increment.

A graphical analysis of one entire spectrum obtained with the anti-coincidence annulus revealed the existence of the inner groups given in Table VII, as well as a group at 2.41 MeV identified as the ground-state transition of La^{141} (24). The coincidence results to be discussed below indicate that not all the groups were revealed in the analysis. In particular, it is believed that the group at 1.8 MeV is in reality an unresolved doublet consisting of the groups β_6 and β_7 and the group at 1.2 MeV is similarly a combination of groups with end-point energy 1.1 and 1.23 MeV respectively. The relative intensities of groups revealed in the analysis were obtained by integrating the component spectra. The intensities of the combined groups at 1.8 and 1.2 MeV were assumed to represent the sum of the intensities of the individual components.

In Figure 34 is shown the beta spectrum in coincidence with events detected in the gamma-ray counter in the energy region corresponding to the 0.645-MeV photopeak. The spectrum shown is a composite of several experiments. The analysis revealed the existence of beta groups with end-point energies of 3.85, 3.05 and 2.15 MeV. In order to obtain the relative intensities of these groups, it was necessary to make use of the gamma-ray branching ratios and the proposed decay scheme. If r_i is the ratio of the areas of the group β_i to the 3.85 MeV group in the coincidence spectrum, then the branching ratio b_i is given by

$$b_i = r_i \left\{ \frac{\sum f_r}{f_i(1 + x)} \right\}$$

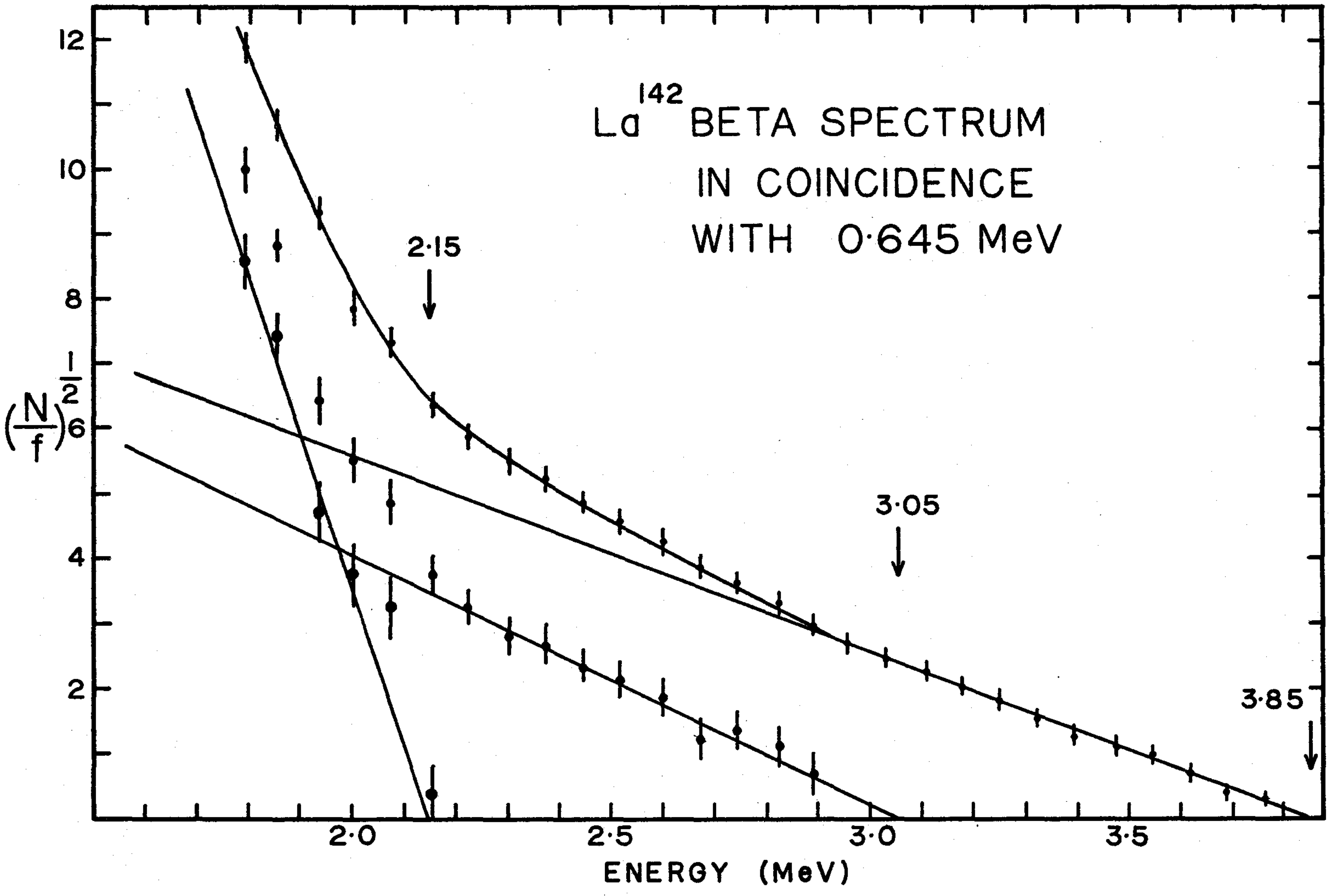
La^{142} BETA SPECTRUM
IN COINCIDENCE
WITH 0·645 MeV
2·15
3·05
3·85
12
10
8
6
4
2
$\left(\frac{N}{f}\right)^{\frac{1}{2}}$
2·0
2·5
3·0
3·5
ENERGY (MeV)

FIGURE 34

TABLE VII

Summary of La^{142} Beta Groups

	Singles	0.645	0.898	1.74	1.91	2.06	2.19	2.41	2.55	3.0 - 3.7	3.65	E	Q_β
β_1	4.49											4.49	4.49 ± 0.04
β_2	3.8	3.85										3.85	4.50 ± 0.05
β_3		3.05	2.97									2.98	4.52 ± 0.05
β_4							2.31					2.31	4.50 ± 0.09
β_5	2.1	2.15	2.10	2.12				2.08				2.11	4.52 ± 0.03
β_6	1.8				1.98				1.96			1.97	4.53 ± 0.06
β_7			1.7			1.84						1.79	4.50 ± 0.03
β_8	1.2									1.23		1.23	4.54 ± 0.09
β_9	0.9									0.86	0.88	0.87	4.52 ± 0.06

$\bar{Q}_\beta = 4.51 \pm 0.03$ MeV

where the f_r are the relevant gamma-ray branching ratios and x is a first order correction for Compton interference. In this way the analysis leads to the relative intensities of groups β_2, β_3 and β_5.

In Figure 35 is shown the spectrum of beta particles in coincidence with events corresponding to the 0.862 - 0.898 MeV photopeak. Graphical analysis of this composite spectrum reveals the existence of groups at 2.97, 2.1 and 1.7 MeV, identified as groups β_3, β_5 and β_7. The relative intensities of these three groups was determined in the same manner as in the case of the 0.645-MeV coincidence spectrum. For both these spectra the end point of the single-crystal spectrum was used as one calibration point instead of the Cl^{38} source.

In Figure 36 is shown the beta spectrum in coincidence with events in the 1.91-MeV photopeak. The spectrum was corrected for Compton interference by subtracting the distribution in coincidence with events in the region corresponding to the valley between the 1.91- and 2 MeV photopeaks. The spectrum in this region corresponds to a single group with end-point energy 1.98 MeV. The energy calibration was determined using the Compton edges from Mn^{54} and Zn^{65} as well as the standard beta sources. In Figure 36 is also illustrated the beta spectrum in coincidence with events corresponding to the 2.06 - 2.19 MeV photopeaks corrected for Compton interference. The analysis reveals groups with end-point energies 2.31 MeV and 1.84 MeV identified as groups β_4 and β_6 respectively. This spectrum provides the only evidence for the existence of the β_4 group. On the basis of the energies, the β_4 group was assumed to be in coincidence with the 2.19 MeV gamma ray and the β_6 group assigned to be correlated with the 2.06-MeV transition. In Figure 37 are illustrated the spectra in coincidence

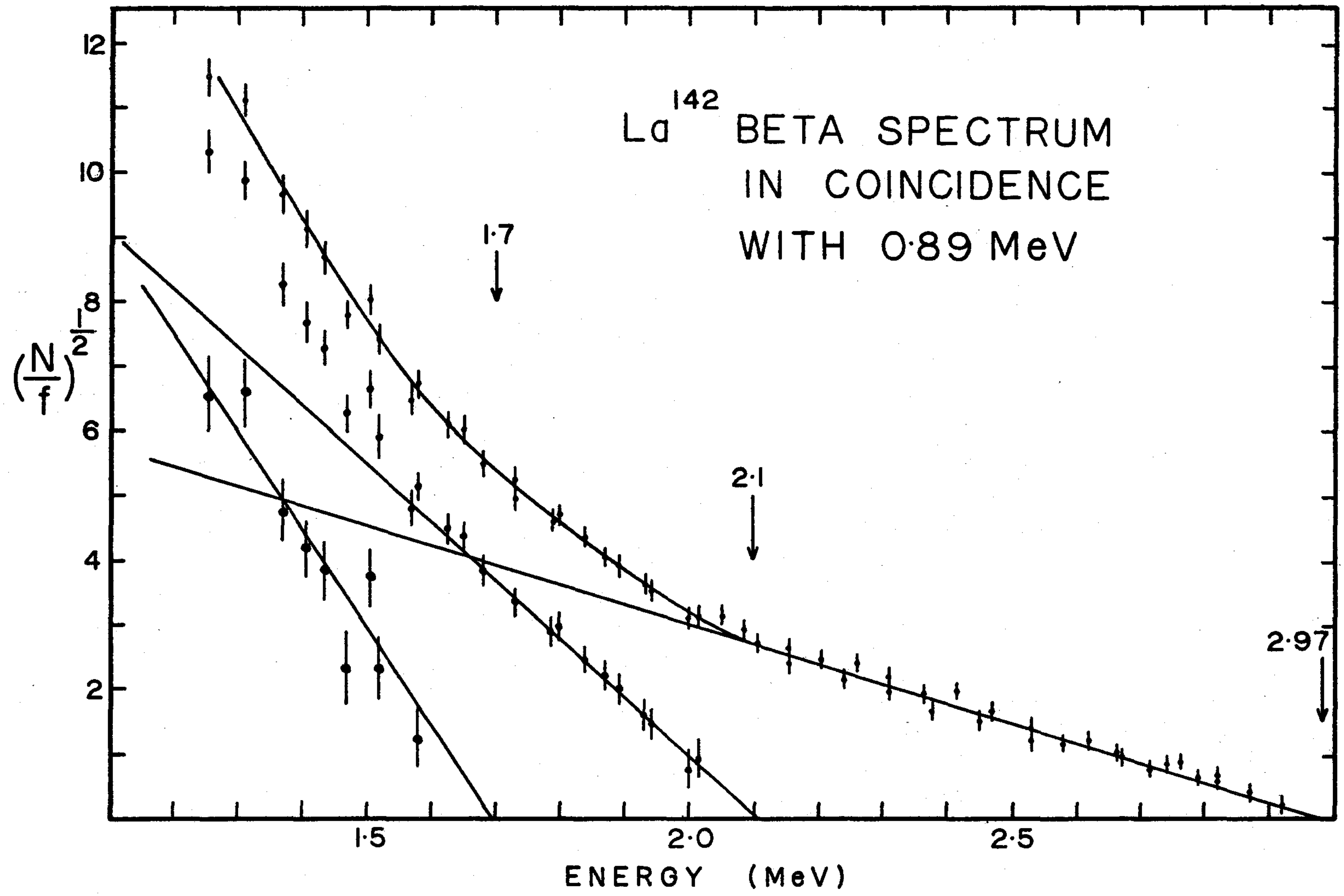
La^{142} BETA SPECTRUM
IN COINCIDENCE
WITH 0·89 MeV
1·7
2·1
2·97
$\left(\frac{N}{f}\right)^{\frac{1}{2}}$
12
10
8
6
4
2
1·5
2·0
2·5
ENERGY (MeV)

FIGURE 35

FIGURE 36

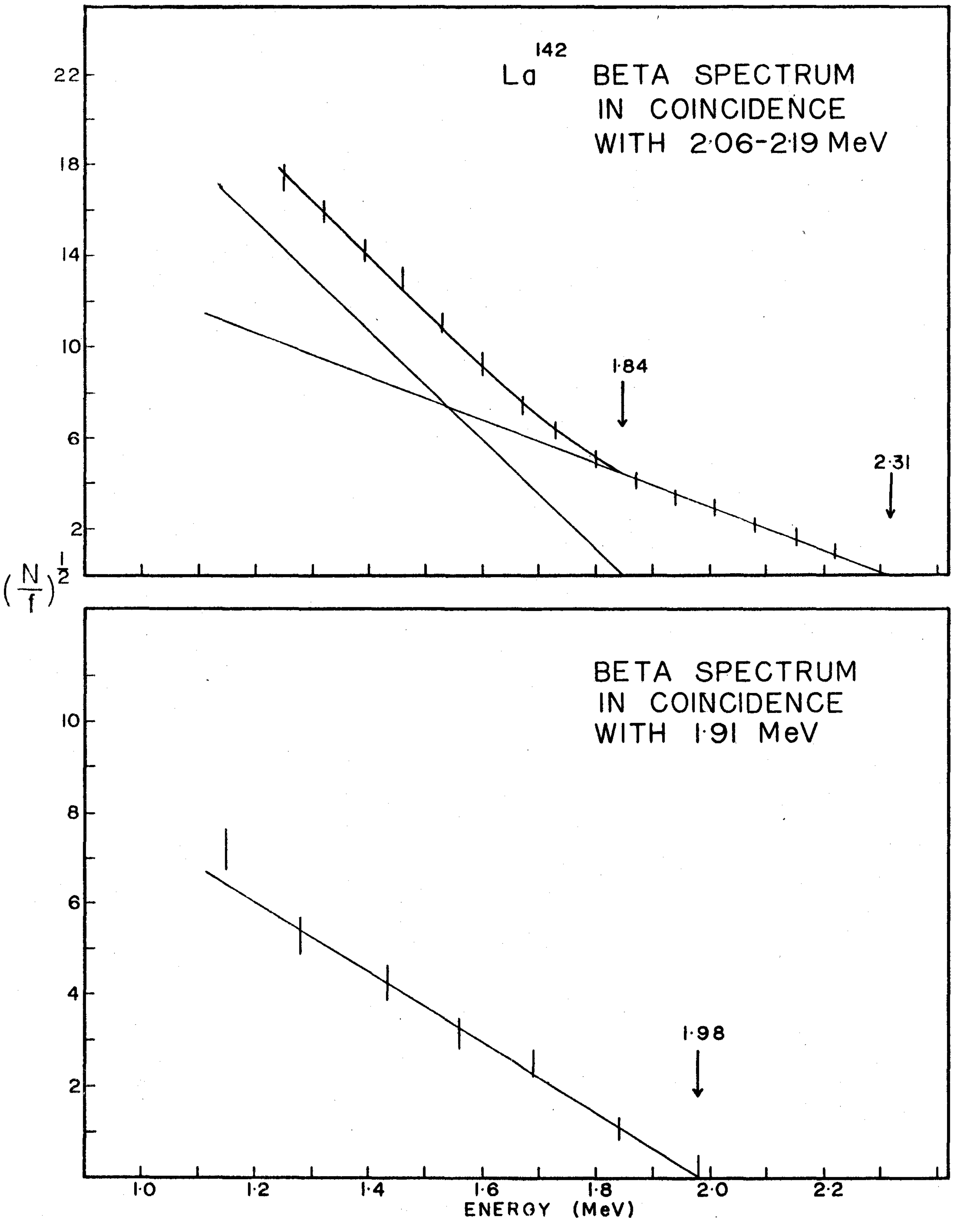
La^{142} BETA SPECTRUM IN COINCIDENCE WITH 2·06-2·19 MeV
1·84
2·31
BETA SPECTRUM IN COINCIDENCE WITH 1·91 MeV
1·98
$(\frac{N}{f})^{\frac{1}{2}}$
22
18
14
10
6
2
10
8
6
4
2
1·0
1·2
1·4
1·6
1·8
2·0
2·2
ENERGY (MeV)

FIGURE 37

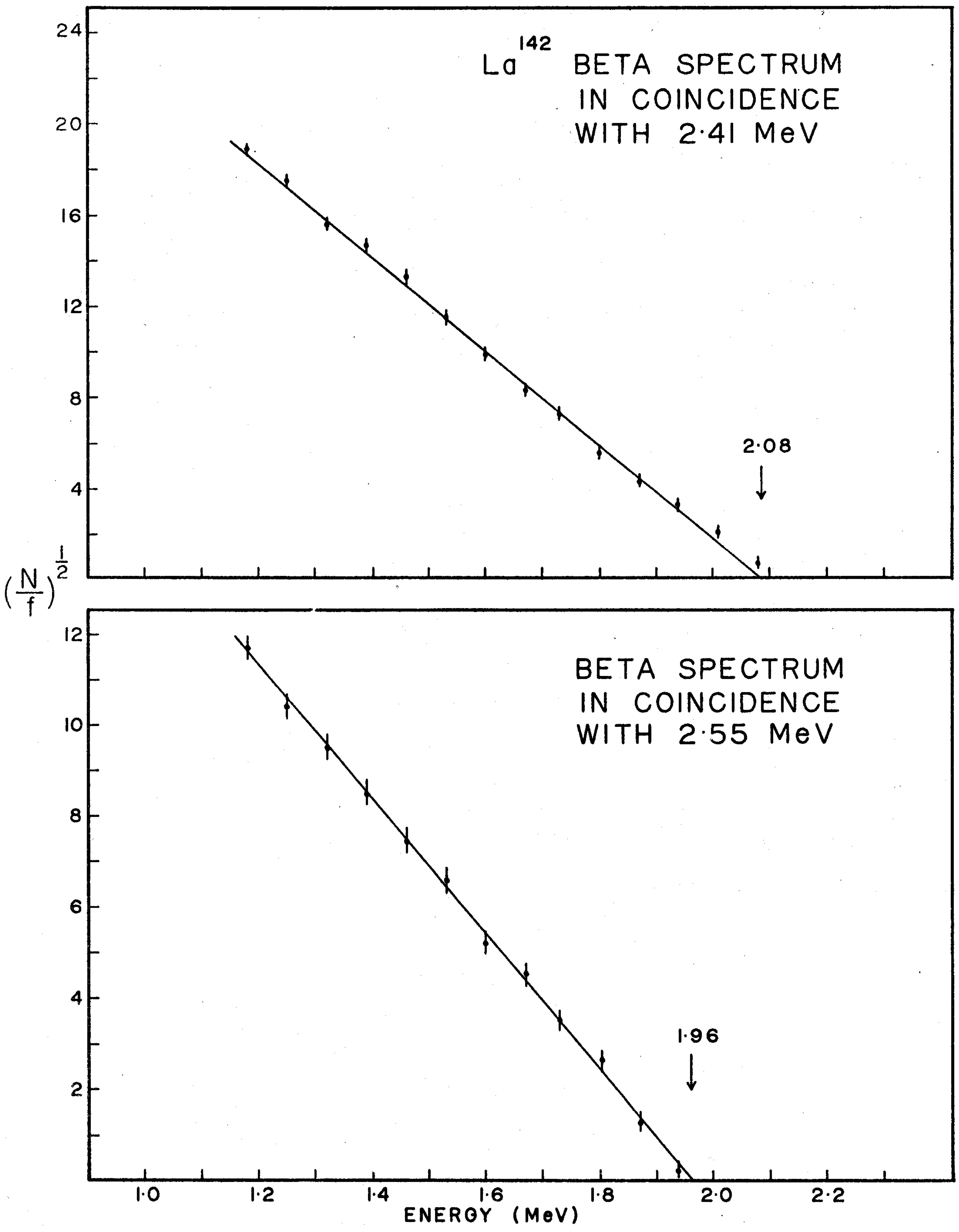

La^{142} BETA SPECTRUM IN COINCIDENCE WITH 2·41 MeV
2·08
24
20
16
12
8
4
$\left(\frac{N}{f}\right)^{\frac{1}{2}}$
BETA SPECTRUM IN COINCIDENCE WITH 2·55 MeV
1·96
12
10
8
6
4
2
1·0
1·2
1·4
1·6
1·8
2·0
2·2
ENERGY (MeV)

with the 2.41- and 2.55-MeV gamma rays. These spectra consist of single components with end-point energies of 2.08 and 1.96 MeV identified as groups β_5 and β_6 respectively. The spectrum in coincidence with the 1.74-MeV gamma ray also consisted of a single group of end-point energy 2.12 MeV corresponding to group β_5. The spectra illustrated in Figure 36 and Figure 37 result from cuts through the two-dimensional distribution of beta-gamma coincidences and are therefore obtained at exactly the same gain and geometry. For this reason the relatively small energy differences between the end points of the spectra are not masked by uncertainties in the calibration.

In Figure 38 is shown the beta spectra in coincidence with 3.65-MeV and $>$ 3.0-MeV events detected in the gamma channel. These spectra indicate the existence of beta transitions with maximum energies of 0.87 and 1.23 MeV. On the basis of the energies and coincidence relations of the gamma-ray transitions, it is believed that the 1.23-MeV group shown in Figure 38 is in reality an unresolved doublet corresponding to groups with end-point energies 1.23 and $\sim$ 1.1 MeV.

A summary of the evidence for the existence of the nine beta groups observed is given in Table VII. The average value of the end point for each group was determined in those cases for which more than one energy measurement was involved. The value obtained from the end point of an inner group revealed by graphical analysis was given less weight in the average than the value obtained under coincidence conditions for which the group under consideration corresponded to the highest energy component. In the case of the beta groups with end-point energies less than 2.1 MeV, the energy values obtained from the

FIGURE 38

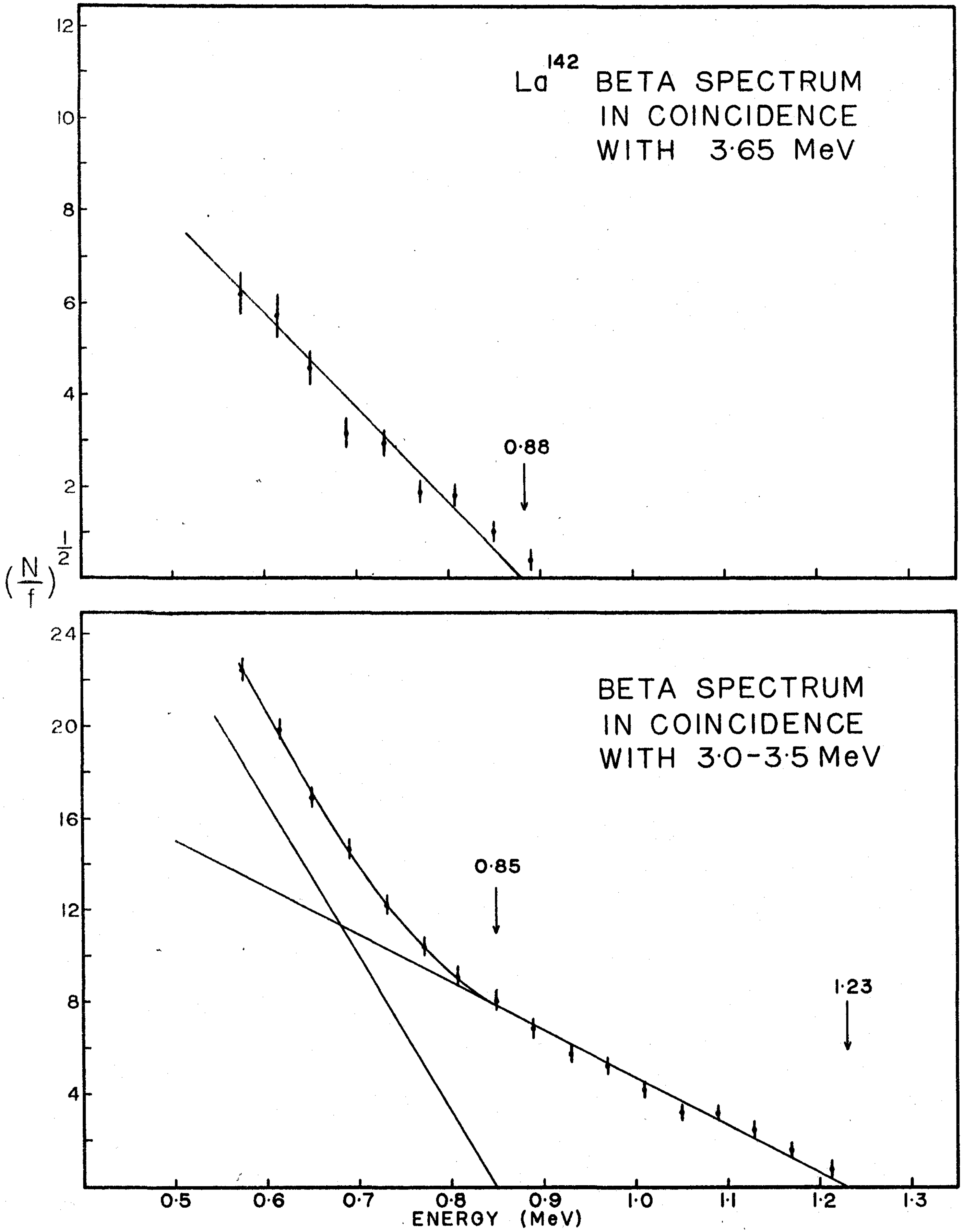

La^{142} BETA SPECTRUM
IN COINCIDENCE
WITH 3·65 MeV
0·88
12
10
8
6
4
2
$\left(\frac{N}{f}\right)^{\frac{1}{2}}$
BETA SPECTRUM
IN COINCIDENCE
WITH 3·0–3·5 MeV
0·85
1·23
24
20
16
12
8
4
0·5
0·6
0·7
0·8
0·9
1·0
1·1
1·2
1·3
ENERGY (MeV)

single-crystal spectrum were not included in the average. Also presented in Table VII are the values of the total energy release Q_β. These values are obtained from the energy of the beta group β_i and the average value of the energy of the corresponding level E_i in the proposed decay scheme, based on the gamma-ray energies. The final estimate of Q_β was obtained from the weighted average of the individual measurements.

In Table VIII is presented the intensities of the beta transitions present in the decay of La^{142} and observed in this work. The relative intensity of the 1.99-MeV group was obtained from the difference between the relative intensities of the combined group revealed in the single-crystal spectrum at 1.8 MeV (31%) and the relative intensity of the 1.79-MeV group obtained from the 0.89-MeV coincidence experiment (11%). The value of the relative intensity for the combined group of 1.2 MeV in the single-crystal spectrum corresponded to 10%. The intensities of the component groups β_8, β_{10} was obtained from the values of the relative gamma ray intensities <u>viz</u>

$$\frac{I(\beta_8)}{I(\beta_{10})} = \frac{f_{3.31} + f_{2.67}}{f_{3.45} + f_{2.80}} .$$

This formula is based on the proposed decay scheme. The branching ratios were obtained from the relative intensities assuming that these ten groups accounted for 100% of the decays.

These values are compared with the branching ratios obtained directly from the decay scheme and the relative gamma-ray intensities. The values obtained from this method were normalized to those determined from the beta spectra by requiring that the sum of the intensities of the beta groups with end-point energies less than or equal to 2.1 MeV

TABLE VIII

Intensity of La^{142} Beta Transitions

Transition	E_β (MeV)	Intensity (%)		Average	Log ft
		Beta Measurement	Gamma Measurement		
β_1	4.49 ± 0.05	13	12	12.5	8.9
β_2	3.85 ± 0.04	2.4	< 3	2.4	9.3
β_3	2.98 ± 0.03	1.7	< 4	1.7	9.0
	2.5*		~ 1	~ 1	~ 9
β_4	2.31 ± 0.05		6.7	6.7	7.9
β_5	2.11 ± 0.03	26	22	24	7.1
β_6	1.98 ± 0.04	20	19	19.5	7.2
β_7	1.79 ± 0.03	11	11	11	7.2
β_8	1.23 ± 0.06	4.4	5.4	4.9	6.9
	1.1*	5.6	6.1	5.8	6.8
β_9	0.87 ± 0.03	15	11	13	6.0

*The energy of these groups was inferred from the decay scheme.

be the same in both measurements. The branching ratio for the ground-state transition is in this case the difference between the normalized gamma ray intensities and 100%. The intensities of the groups β_2 and β_3 obtained from the gamma-ray measurements are rather inaccurate since they involve the difference between several gamma-ray intensities. For instance, the intensity of the beta group β_2 results from the difference between the sum of the intensities of ten gamma rays which are believed to populate the relevant level and the intensity of the 0.645-MeV gamma ray.

In principle, a check of the balance between the beta intensities and the intensities of the gamma radiations provides a sensitive test of the validity of a decay scheme. However, the intensities obtained in this work from both beta- and gamma-radiation measurements are not entirely independent. In addition, there is no absolute measurement involved which would verify the assumption that these transitions amount to 100%. The values obtained from both methods do indicate that there is internal consistency in the data within the expected accuracy of the measurements. The final estimates of the branching ratios were obtained by averaging the results obtained from both methods and renormalizing to 100%. In the case of groups β_2 and β_3 the values obtained from the beta measurements alone were taken because of the large uncertainty in the values resulting from the gamma-ray intensities.

The value of log ft for groups β_1,β_2 and β_3 indicates that these transitions are probably first forbidden. The beta spectrum corresponding to the class of first-forbidden transitions for which there is a spin change of two units is known to have a unique shape.

In this case, the Kurie plot is no longer linear but given by

$$y = \frac{N}{p^2}^{1/2} = \sqrt{C_1}\, k(E_o - E)$$

where $C_1 = (E^2 + 2E) + (E_o - E)^2$ is the energy-dependent shape factor. The first-forbidden unique shape of the Y^{90} beta spectrum was revealed in the scintillation-spectrometer data when corrections were made for finite response. However, the shape of the La^{142} beta spectrum is obscured by the presence of transition β_2 with end-point energy 3.85 MeV. In this case only approximately the highest 17% energy region of the spectrum is free from interference. The scintillation spectrum corrected for finite response is not sufficiently accurate to reveal definite information about details of the spectral shapes under these conditions. The La^{142} beta spectrum in the region above 2.7 MeV was therefore investigated in detail using a magnetic spectrometer.

A Gerholm (64) spectrometer, adjusted for approximately 3% resolution and 3% transmission was used for this purpose. The spectrometer was calibrated using the externally converted electrons from the 2.76-MeV Na^{24} gamma ray incident on a Th radiator. The beta spectrum obtained for La^{142} is shown in Figure 39. This spectrum represents the sum of ten separate scans obtained with five sources. As can be seen from the figure, it is still not possible to directly distinguish between the allowed or forbidden shape. However, indirect evidence indicating that the group β_1 has a unique shape results from a comparison of the energy of the β_2 group obtained from analysis of this spectrum based on the two possible shapes of the β_1 group assumed.

Assuming an allowed shape, the Kurie plot in the region above 3.85 MeV is represented by $y = \alpha(E_o - E)$. The best values of "α" and

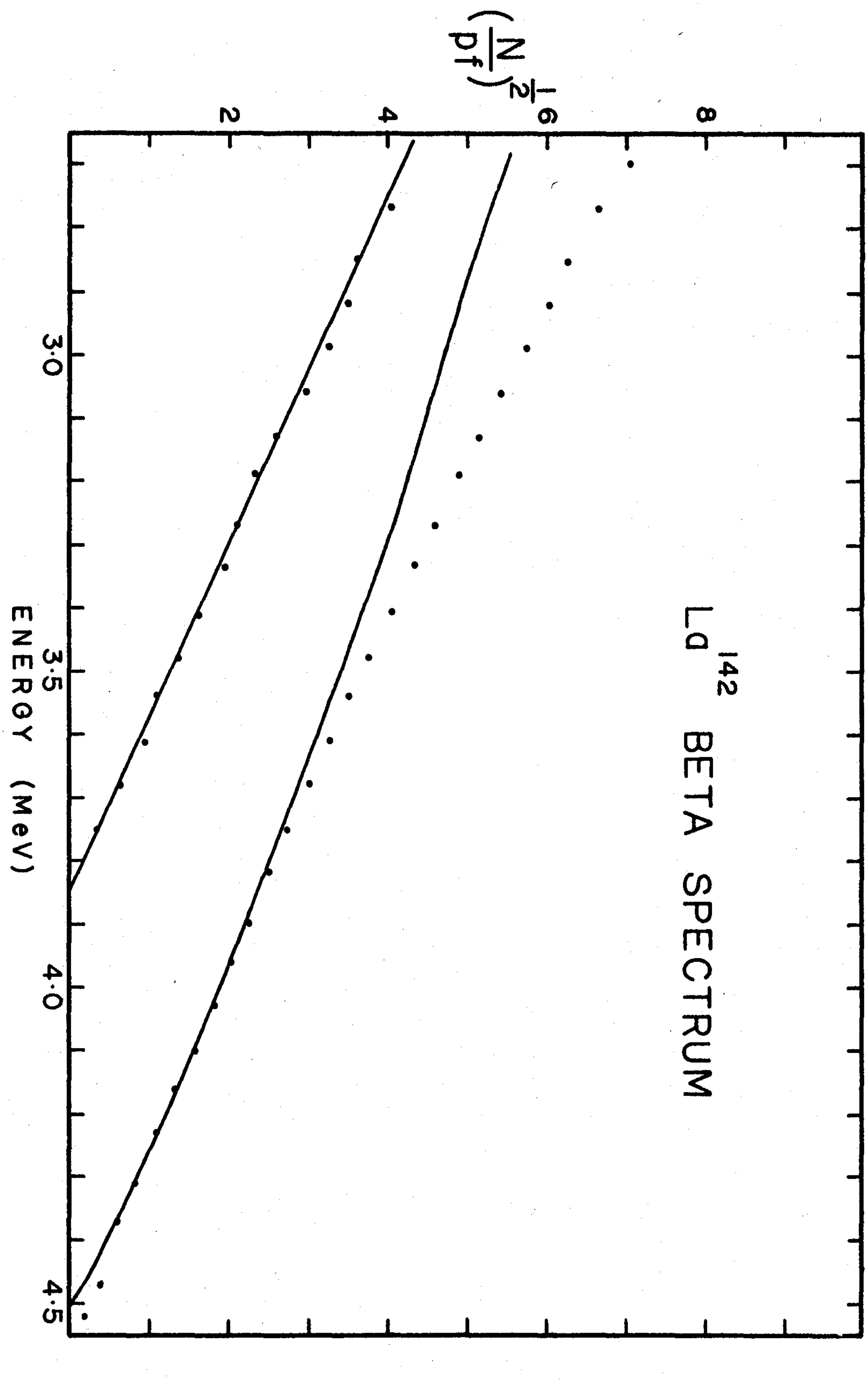
La142 BETA SPECTRUM
$\left(\frac{N}{pf}\right)^{\frac{1}{2}}$
2
4
6
8
3·0
3·5
4·0
4·5
ENERGY (MeV)

FIGURE 39

E_o were determined by the method of least squares based upon the points above 3.85 MeV. The values of the regression curve were then used to obtain the contribution to the total spectrum corresponding to the β_1 group. The difference spectrum was then analyzed in a similar manner in order to obtain the least squares estimate for the end point of the first inner group. The results are shown in Table IX.

The analysis was repeated assuming a unique shape for the β_1 component and an allowed shape for β_2. The results of the two analyses are compared in Table IX, together with the results based on the scintillation beta- and gamma-ray measurements. As a further test an independent measurement of the end-point energy of the β_2 group was made, using the Gerholm spectrometer together with a two-inch NaI(Tl) gamma detector and a coincidence-gated analyzer. The energy value of the β_2 end point obtained with the Gerholm spectrometer is in excellent agreement with the scintillator results. The errors quoted for the least-squares estimates are the standard deviations obtained solely on the basis of the statistics of the data. The uncertainty in the absolute values is estimated to be 0.5%. The difference in the energies of group β_1 obtained assuming either an allowed or unique shape agree with the average Q_β value within the expected accuracy although the mean value based on the forbidden shape agrees more closely.

The statistical error in Δ must be combined with a possible systematic uncertainty of 0.5%, or approximately 4 keV. The value of Δ obtained when a forbidden shape is assumed for β_1 is in agreement with the gamma-ray energy within the standard deviation. When an allowed shape is assumed for β_1, the value of Δ is in disagreement with the gamma-ray energy by nearly 3 standard deviations. On this

TABLE IX

Summary of Evidence for a Unique Shape in the La^{142} Ground State Beta Transition

E(MeV)	Allowed	Forbidden	Other Evidence
β_1	4.546 ± 0.006	4.517 ± 0.006	4.51 ± 0.03 (average Q-value)
β_2	3.707 ± 0.06	3.852 ± 0.02	3.85 ± 0.03 (scintillator) 3.85 ± 0.02 (magnetic)
Δ	0.839 ± 0.07	0.665 ± 0.02	0.645 ± 0.006 (gamma ray scintillation)

basis it is possible to assign values for the likelihood that β_1 has an allowed or forbidden shape of approximately 0.02 and 0.64 respectively.

Obviously, the evidence for the possible unique shape of the ground-state transition beta spectrum presented here is much weaker than a direct observation of the shape. However, it can be said that the data is more consistent with the results obtained from other measurements when analyzed on the basis that the β_1 group corresponds to a unique first-forbidden transition.

6.5 Angular Correlation Studies

The study of the angular correlation between cascade gamma rays in La^{142} is made difficult both because the counting period is limited by the half life of 92.6 min and because the gamma-ray spectrum is complex so that there is a relatively large amount of interference in the region of the full-energy peaks of interest. The limitation in counting period necessitated the use of many sources in determining the correlation function. The value of the correlation function was determined for five angles in one ninety-degree quadrant and for each angle a new source was prepared and counted. Thus each determination of the correlation function required five sources. Each point was normalized to the same single crystal counting rate.

The correlations involving the 0.645-MeV transition were measured both with the fast-slow coincidence system and the two-dimensional sum-coincidence system. Since the experimental conditions are quite different in these two systems, it is unlikely that interference would affect the correlation functions in the same way. No statistically significant differences were observed in the comparison between the correlation functions obtained using both methods. A summary of the results of a least-squares analysis of the correlation functions measured is given in Table X.

In Figure 40 is shown the angular-correlation function obtained for the 0.898 - 0.645 MeV cascade. The final values shown are the averages of the fast-slow and sum-coincidence results. The curve shown is the least-squares curve. In the case of the former method, interference from the 0.86-MeV component of the doublet, the intensity of which is approximately one-quarter that of the 0.898-MeV component, was minimized by integrating only the high-energy side of the doublet full-energy peak. Similarly, in the sum-coincidence experiment, only the high-energy portion of the peak in the sum dimension was included in the analysis. A comparison of Figure 25 and Figure 32 indicate the advantages of the sum-coincidence method insofar as simplification of analysis is concerned. In the sum-component spectrum the 0.645-MeV and 0.898-MeV lines are prominent whereas the spectrum of events coincident with pulses in the 0.645-MeV window is complex and the correction for Compton interference under the 0.898-MeV peak is sizeable. Nevertheless, the results obtained from both methods agreed within the statistical accuracy. This is quite possibly due to the strong angular correlation between these two transitions so that any remnant interference has little effect.

There is plentiful evidence to be cited in the next chapter that the 0.645-MeV transition results from de-excitation of a 2+ level leading to the 0+ ground state. This transition is therefore pure electric quadrupole (E2). The 0.645-0.898 MeV results can be

La^{142} ANGULAR CORRELATIONS

FIGURE 40

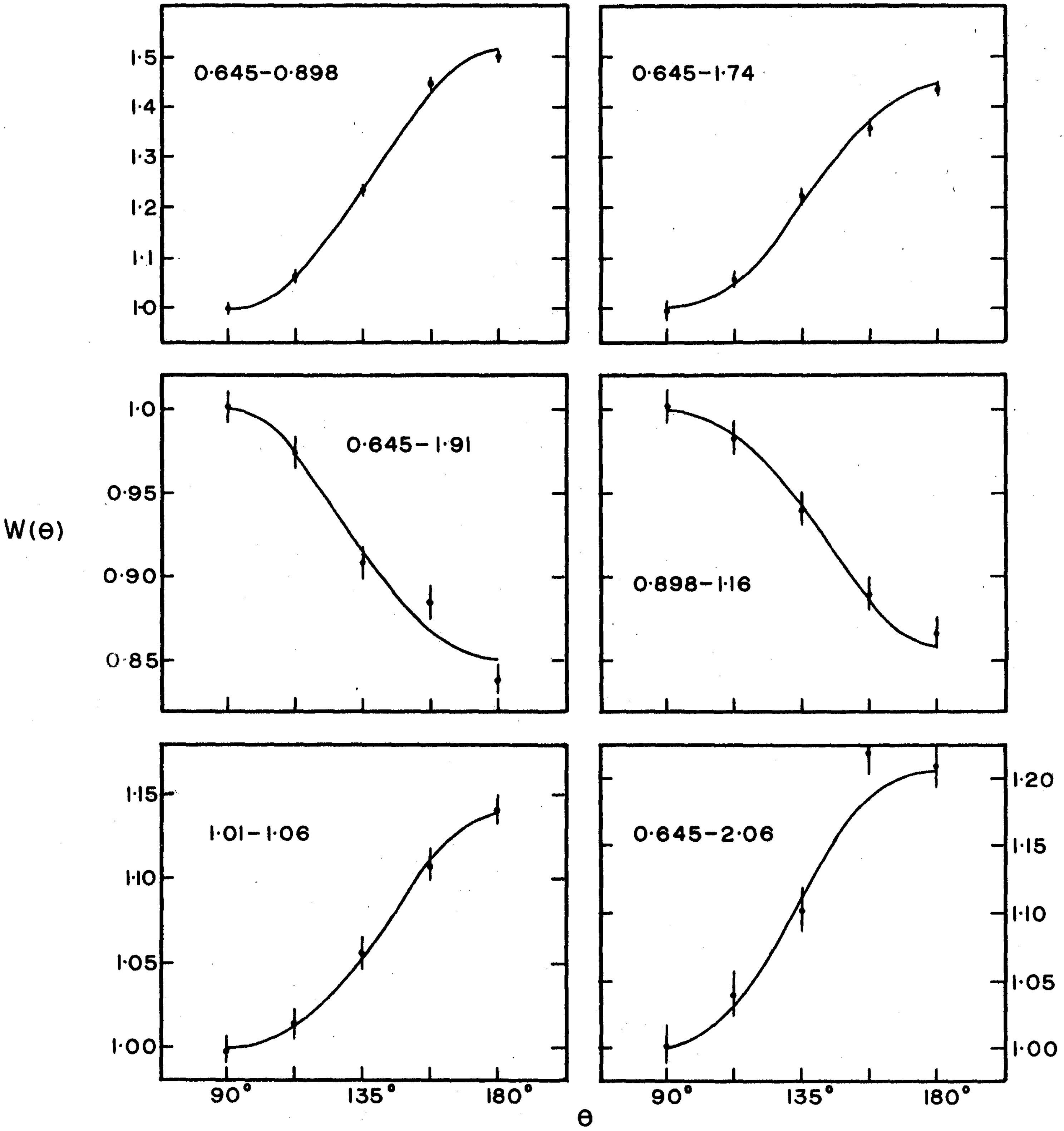

TABLE X

Summary of Angular Correlation Results

Cascade (MeV)	A_2	A_4	Assignment	Mixing
0.645 - 0.898	0.306 ± 0.02	0.016 ± 0.03	2(D,Q) 2(Q)0	$\delta = 0.08 \pm 0.03$
0.645 - 1.74	0.277 ± 0.02	0.016 ± 0.03	2(D) 2(0)	$\delta = 0.04 \pm 0.03$
0.645 - 1.91	-0.118 ± 0.03	0.011 ± 0.03	1(D,Q) 2(Q)0 3(D,Q) 2(Q)0 4(Q,0) 2(Q)0	$\delta = 0.1 \pm 0.02$ $\delta = 0.06 \pm 0.03$ $\delta = 0.35 \pm 0.05$
0.645 - 2.06	0.152 ± 0.02	0.001 ± 0.03	2(D,Q) 2(Q)0 3(D,Q) 2(Q)0 4(Q,0) 2(Q)0	$\delta = -0.1 \pm 0.05$ $\delta = -0.3 \pm 0.05$ $\delta = -0.09 \pm 0.05$
0.645 - 1.01 - 1.06	0.038 ± 0.03	0.036 ± 0.04		
0.898 - 0.86	0.055 ± 0.02	-0.018 ± 0.03		
0.898 - 1.16	-0.101 ± 0.006	-0.017 ± 0.01		
1.01 - 1.06	0.090 ± 0.004	0.021 ± 0.006		

unambiguously identified with a 2(D,Q) 2(Q)0 sequence. A comparison of the measured values with the theoretical coefficients is illustrated in Figure 41.

The correlation of the 0.645 - 1.01 MeV cascade could not be observed without interference from the 1.06-MeV transition. In this case, both components of the 1.01 - 1.06 MeV doublet are approximately equal in intensity. By integrating over the entire doublet the correlation corresponding to the three-member cascade 0.645 - 1.01 - 1.05 MeV was obtained. This correlation by itself contains insufficient information for a unique interpretation.

The angular correlation between the 0.645- and 1.74-MeV transitions is similar to the 0.645 - 0.898 MeV correlation. The values for this function were also obtained from the average of fast-slow and sum-coincidence results. The experimental curve is illustrated in Figure 40. The correlation leads to an unambiguous assignment of 2(D,Q) 2(Q)0 for the spin sequence in the 0.645 - 1.74 MeV cascade as illustrated in Figure 41. The values of the coefficients indicate that the 1.74-MeV gamma ray is a relatively pure dipole transition.

The 0.645 - 1.91 MeV angular-correlation results shown in Figure 40 do not lead to a unique assignment for the spin sequence. The coefficients are consistent with 1(D,Q) 2(Q)0, 3(D,Q) 2(Q)0 and 4(Q,O) 2(Q)0 sequences, as illustrated in Figure 41. For the spin 3 sequence the value of the mixing ratio is smaller than that required for agreement with the measured values of the coefficients when the 1-2-0 or 4-2-0 sequences are assumed.

The 0.645 - 2.06 MeV correlation function was determined using the fast-slow coincidence arrangement. The correlation may be disturbed

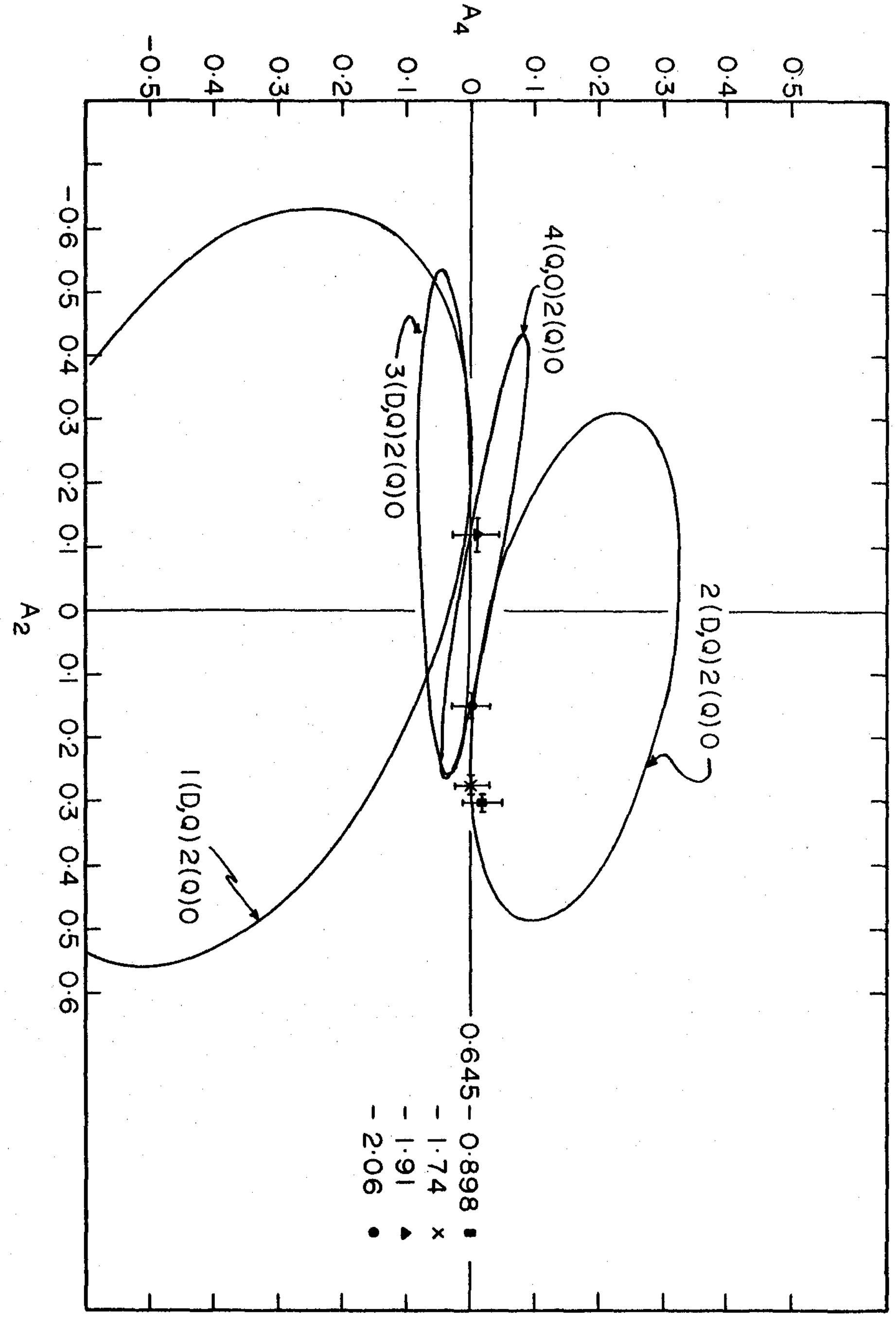

FIGURE 41

COMPARISON OF ANGULAR CORRELATION COEFFICIENTS WITH THEORETICAL VALUES to a certain extent by interference from the 2.14-MeV gamma ray. Only the low-energy portion of the 2.06-MeV photopeak was included in the analysis in order that this interference be kept to a minimum. The coefficients are consistent with an initial spin of 2, 3 or 4 so that the assignment in this case is ambiguous. For the case of 2 or 3, the A_2 coefficient is consistent with relatively pure dipole order for the 2.06-MeV transition, while the spin 4 correlation is consistent with nearly pure quadrupole.

The 0.898 - 1.17 MeV and 1.01 - 1.06 MeV correlations were studied by means of a two-dimensional sum-coincidence arrangement. One dimension was assigned to the sum distribution in the region from 1.5 to 2.2 MeV and the other dimension to the component distribution in the region from 0.6 - 1.3 MeV. The determination of the spin sequences from these correlations requires additional information to that contained in the correlation function since both the spins and mixing ratios of both components are unknown. The interpretation of these correlations can only be made within the context of the decay scheme and will be discussed in the next chapter.

CHAPTER VII

DISCUSSION OF RESULTS

7.1 Decay Scheme of La^{142}

In Figure 42 is shown a proposed decay scheme for 92.6-min La^{142} constructed on the basis of the experimental results. This decay scheme is consistent with the energies, intensities and coincidence relationships of the beta and gamma radiations observed in this work to within the accuracy of the results. It is believed to account for the prominent de-excitation modes of the $La^{142} - Ce^{142}$ beta decay. Observed coincidence relations are denoted by a full circle, the standard notation of the Nuclear Data Group (65). The average energy and relative intensity of each gamma ray is given with the intensity in brackets below the energy. The energy and log ft value for each beta group are similarly indicated.

The evidence for the first state at 0.645 MeV is conclusive. The 0.645-MeV gamma ray is the transition with the greatest intensity. There are six pairs of gamma transitions, 3.65 - 2.99 MeV, 3.45 - 2.80 MeV, 3.31 - 2.67 MeV, 2.55 - 1.91 MeV, 2.41 - 1.74 MeV and 2.19 - 1.54 MeV with energy differences of approximately 0.65 MeV for which the lower energy members were observed to be in coincidence with the 0.645 - MeV transition. Finally, the energy difference between the maximum energy

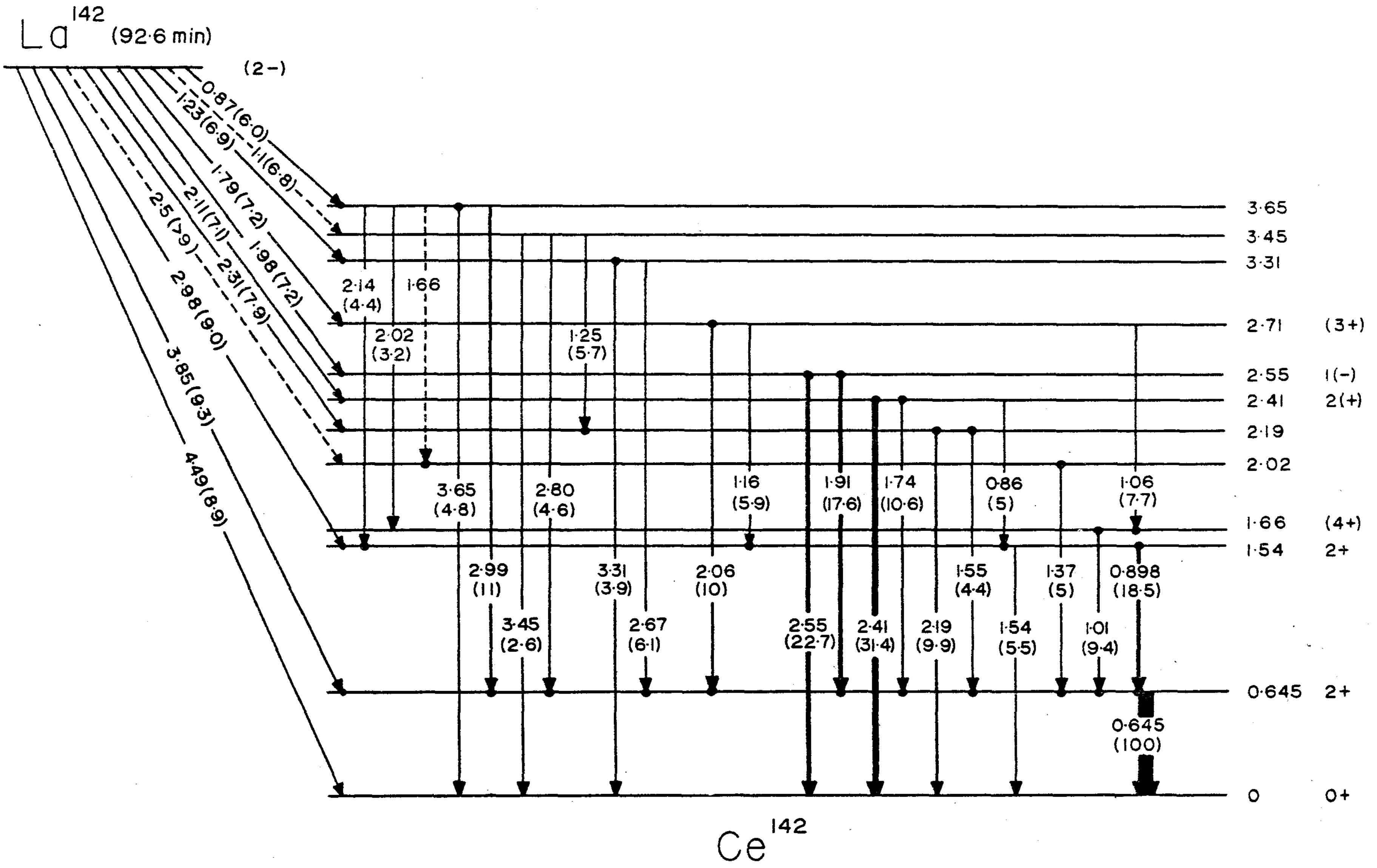
La^{142} (92·6 min)
(2−)
0·87(6·0)
1·1(6·8)
1·23(6·9)
1·79(7·2)
1·98(7·2)
2·11(7·1)
2·31(7·9)
2·5(>9)
2·98(9·0)
3·85(9·3)
4·49(8·9)
2·14
(4·4)
1·66
2·02
(3·2)
1·25
(5·7)
3·65
(4·8)
2·80
(4·6)
1·16
(5·9)
1·91
(17·6)
1·74
(10·6)
0·86
(5)
1·06
(7·7)
2·99
(11)
3·45
(2·6)
3·31
(3·9)
2·67
(6·1)
2·06
(10)
2·55
(22·7)
2·41
(31·4)
2·19
(9·9)
1·55
(4·4)
1·54
(5·5)
1·37
(5)
1·01
(9·4)
0·898
(18·5)
0·645
(100)
3·65
3·45
3·31
2·71 (3+)
2·55 1(−)
2·41 2(+)
2·19
2·02
1·66 (4+)
1·54 2+
0·645 2+
0 0+
Ce^{142}

FIGURE 42

beta group observed in coincidence with the 0.645-MeV gamma ray and the ground state beta transition is approximately 0.65 MeV.

The evidence for the existence of the 1.54-MeV level is based on the strong 0.645 - 0.898 MeV coincidence and the energy difference between beta groups β_1 and β_3 of approximately 1.5 MeV. The energy of the 1.54-MeV gamma ray indicates that this could be the transition corresponding to de-excitation of this level directly to the ground state. The value of the coincidence quotients $q_{0.645,1.54}$ and $q_{1.54,0.645}$ indicate that approximately half the transitions of this energy occur in coincidence with the 0.645-MeV gamma ray. For this reason the intensity of the 1.54-MeV cross-over transition is only about one-half the single-crystal value.

On the basis of energies, previous researchers (23,24) assigned the 1.01-MeV gamma ray to correspond to a transition between the states at 2.55 and 1.54 MeV. However, the coincidence results obtained in this work give very small coincidence quotients for a 0.898 - 1.01 MeV time correlation, indicating that these transitions are not in coincidence to the extent required for this interpretation. The strong 0.645 - 1.01, 1.06 MeV coincidence requires, therefore, that there be a level at 1.66 MeV. The order of the 1.01 - 1.06 MeV gamma rays is based on the greater intensity of the lower energy component of the doublet. No beta transition to this level was observed, indicating that it is predominantly populated from the de-excitation of higher energy Ce^{142} states.

The 1.37-MeV gamma transition exhibits coincidence relationships only with the 0.645-MeV gamma ray and a weak 1.66-MeV transition not observed in the single-crystal spectrum. The 0.645 - 1.37 MeV coincidence was also observed by previous researchers (24). The 2.02-MeV level included on the basis of this evidence appears to be the only explanation consistent with these results. The evidence for this level is not conclusive, so that it must be considered tentative. No beta group was observed which would correspond to a transition directly to this level.

The relatively strong beta transition with end-point energy of approximately 2.3 MeV observed in coincidence with gamma rays in the energy region 2.0 - 2.2 MeV indicates the existence of a level at approximately 2.2 MeV. This interpretation is strengthened by the existence of a 2.19-MeV gamma ray and the observation of the 0.645 - 1.54 MeV coincidence relation. This coincidence was reported earlier (24); since the existence of the 2.19-MeV gamma ray and the 2.3-MeV beta group was not revealed in the earlier work, it was previously not possible to interpret this coincidence relationship.

The level at 2.41 MeV is required to explain several experimental results. The relatively strong gamma transition at 2.41 MeV exhibits no coincidence relations with other gamma rays. The 0.645 - 1.74 MeV cascade is then interpreted as resulting from the transition between this level and the first state. Since both the 2.41- and 1.74-MeV gamma rays are in coincidence with the same beta group with end-point energy 2.1 MeV, the interpretation is consistent with the beta-gamma coincidence results. Finally, the existence of the 0.86 - 0.898 MeV doublet and the appearance of the β_5 group in coincidence with gamma rays in the region of 0.645 and 0.898 MeV requires that the 0.86-MeV gamma ray correspond to the transition between the 2.41-MeV level and the second state.

The evidence for the existence of the 2.55-MeV level is based on the appearance of the 2.55-MeV gamma ray uncorrelated with any other transition. This property indicates that the transition results from a de-excitation leading directly to the ground state. The 0.645 - 1.91 MeV coincidence indicates that the 1.91-MeV gamma ray corresponds to the transition between the 2.55-MeV level and the first state. This interpretation is confirmed by the fact that both the 2.55-MeV and 1.91-MeV gamma rays are in coincidence with the β_6 group and therefore de-populate a common level at approximately 2.6 MeV. The coincidence quotients for a possible 0.898 - 1.01 MeV cascade indicate that if a transition exists between this level and the second state, it can represent at most a 2% branching ratio for the de-excitation of the 2.55-MeV level.

The presence of the 1.8-MeV beta group indicates the existence of a level at approximately 2.7 MeV. This group appears in coincidence with gamma rays in the region of 2.0 MeV. This result, together with the fact that there exists a 2.06-MeV gamma ray in coincidence with the 0.645-MeV gamma ray is consistent with the interpretation that the 2.06-MeV gamma ray corresponds to the transition from the 2.7-MeV level to the first state. The 0.898 - 1.17 MeV and 1.01 - 1.05 MeV cascades appear as components of the 2.06-MeV sum-coincidence peak so that the 2.06-MeV transition is interpreted as the cross-over transition for these cascades. Finally, the observed coincidence relationship between the 0.898-MeV gamma ray and the β_7 group indicates that the 1.17-MeV gamma ray corresponds to the de-excitation of this level leading to the second state. No transition from this level to the ground state was observed. It is estimated on the basis of the regression analysis of the single-crystal spectrum that the branching ratio for such a transition must be less than 3%.

The level at 3.31 MeV is based upon the identification of a 3.31-MeV gamma ray exhibiting no coincidences with other gamma rays and a 1.2-MeV beta group observed in coincidence with a gamma ray of energy greater than 3 MeV. The observed 2.67 - 0.645 MeV coincidence is consistent with the identification of the 2.67-MeV gamma ray as corresponding to the transition between this level and the first state. No other de-excitation modes for this level were positively identified.

The existence of a level at 3.45 MeV is required by the observed properties of the 3.45- and 2.8-MeV gamma rays. The 2.8-MeV gamma ray was observed to be in coincidence with the 0.645-MeV transition. In addition, the 2.19 - 1.25 MeV and 1.54 - 1.25 MeV coincidences are consistent with the identification of the 1.25-MeV gamma ray with the transition between the 3.45- and 2.19-MeV levels. The beta group corresponding to the population of the level following the decay of the La^{142} ground state was not observed. It is felt that the energy of this group of approximately 1.1 MeV is sufficiently close to that of the 1.2-MeV group so that under the counting conditions used in this study these two groups were not resolved. The existence of this group was inferred from consideration of the relative gamma-ray intensities. As in the case of the 3.31-MeV level, no transitions leading to levels other than those indicated were positively identified.

The highest energy gamma ray observed in the La^{142} spectrum at 3.65 MeV is in coincidence with the lowest energy beta group identified at approximately 0.9 MeV. Since this gamma ray was not observed in coincidence with any other transition, it may be interpreted as the ground-state transition of a level at 3.65 MeV. This interpretation is consistent with the beta-gamma coincidence results and with the relatively strong 0.645 - 2.99 MeV coincidence. The 0.898 - 2.14 MeV and 1.03 - 2.02 MeV coincidences indicate that these two gamma rays at approximately 2 MeV correspond to de-excitation modes for which the final levels are the 1.54- and 1.66-MeV levels respectively.

The decay scheme presented accounts for all the beta and gamma transitions and their inter-relations. The residual which occurs in some coincidence spectra may indicate that other de-excitation modes of low probability occur in the beta decay of La^{142} in addition to those identified in this study.

On the basis of the relative gamma-ray intensities and the branching ratios of the beta groups, the absolute intensity of the 0.645-MeV gamma ray was calculated to be 50 ± 5%. This value is in reasonable agreement with that measured by Schuman et al (24) of approximately 55%. No error is quoted by these authors.

The average value obtained for the total energy release, 4.51 ± 0.03 MeV, is consistent with the systematics of disintegration energies in this mass region (65) and is in good agreement with the previously measured value of approximately 4.4 MeV (24). No estimate of the accuracy of the previous measurement is given by the authors, but an arbitrary error of ~ 0.3 MeV was assigned by the Nuclear Data Group (65).

The values predicted by the semi-empirical mass formula of Seeger (66) and Cameron (67) are 5.157 MeV and 4.969 MeV respectively, in disagreement with the experimental value by approximately 10%. Such disagreements are typical. The concept of a semi-empirical mass law assumes a relatively smooth dependence of mass on neutron and proton numbers in an isobaric chain for a given nuclear classification (even N, even Z, etc.). The actual values, reviewed by the Nuclear Data Group (65) appear to display a subtle, irregular, fine structure superimposed upon a more or less regular variation.

7.2 Spin and Parity Assignments

A completely unambiguous description of the spin-parity structure of Ce^{142} requires extensive observation of the angular and polarization direction correlations of all the gamma-ray cascades which result from the beta decay of La^{142}. It is possible on the basis of those angular correlation results obtained in this work to assign definite spins to some of the levels. In addition, general arguments based upon the relative intensities of the lepton and electromagnetic disintegration modes may be used to decide upon the most probable spin and parity of several of the levels.

It is a well-established fact that the ground state and first excited state of even A nuclei are of even parity and have angular momentum 0 and 2 respectively. All angular correlation results which involve the 0.645-MeV gamma ray are consistent with these spin assignments. Furthermore, Coulomb excitation studies (68) have confirmed the fact that the 0.645-MeV gamma ray is electric quadrupole.

Since the log ft values of the β_1 and β_2 groups most likely correspond to first-forbidden transitions, the parity of the La^{142} ground state is odd. The experimental investigation of the shape of the ground state beta transition indicates that this transition is probably first-forbidden unique, in which case the spin and parity of the La^{142} is 2^-. The fact that the 0+ Ce^{142} ground state transition occurs with the observed intensity definitely requires that the La^{142} spin cannot exceed 2.

The log ft value for the β_3 component also most likely corresponds to a forbidden transition so that the 1.54 MeV level is required to have even parity. The 0.645 - 0.898 MeV angular correlation can be positively identified as corresponding to a 2(D,Q) 2(Q)0 spin sequence. The small mixing ratio indicates that the 0.898 MeV gamma ray is predominantly a magnetic dipole transition.

The spin of the 2.41 MeV level can also be unambiguously identified as 2 on the basis of the 0.645 - 1.74 MeV angular correlation data. This result also indicates that the 1.74 MeV gamma ray is predominantly dipole. A parity assignment cannot be definitely made for this level. The distribution of log ft values for beta transitions from odd-odd nuclei leading to even-even nuclei with neutron numbers from $N = 84$ to 86 are shown in Figure 43. It can be seen from this figure that the distributions for allowed and first-forbidden transitions are only slightly displaced as regards the range of log ft values. The 0.898 - 0.862 MeV correlation is consistent with the 2-2-2 spin sequence requiring that the 0.862-MeV gamma ray be dipole with a slight quadrupole admixture (4 ± 4%).

The 0.645 - 1.91 MeV angular-correlation results are consistent with a spin assignment of 1,3 or 4 for the 2.55-MeV level. The strong 2.55-MeV ground-state gamma transition leads to an unambiguous assignment of 1 for this level. No definite parity assignments can be made since the log ft value of 7.2 can be interpreted as corresponding to either a first-forbidden or allowed transition.

FIGURE 43

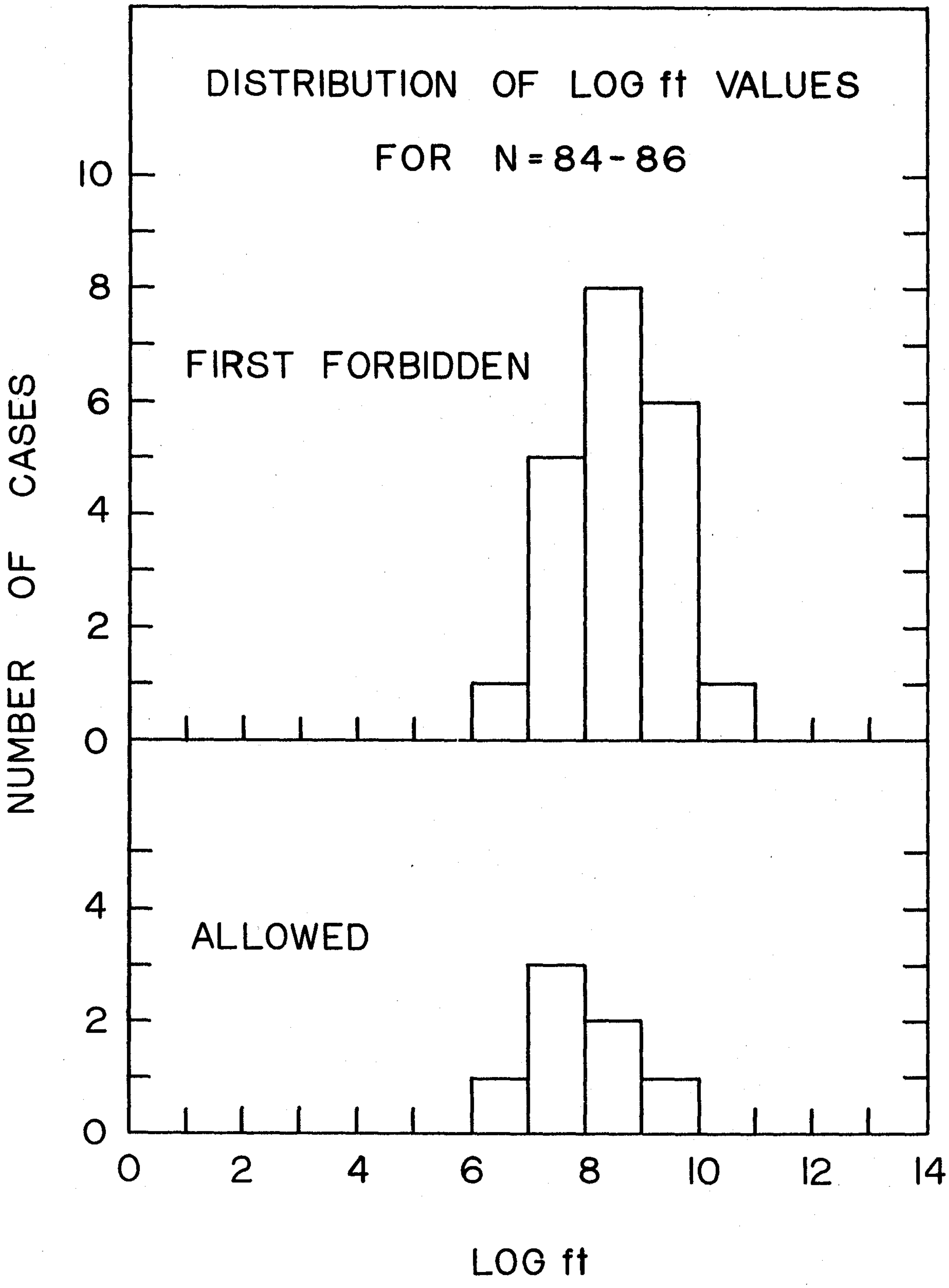
DISTRIBUTION OF LOG ft VALUES
FOR N=84-86
FIRST FORBIDDEN
ALLOWED
NUMBER OF CASES
0
2
4
6
8
10
0
2
4
0
2
4
6
8
10
12
14
LOG ft

The absence of a ground state gamma transition for the 2.71 MeV level indicates that the spin of this state is greater than 2, while the log ft value of 7.2 for the beta transition β_7 requires that the spin be less than 5. A spin of either 3 or 4 is consistent with the 0.645 - 2.06 MeV angular correlation. The 0.898 - 1.17 MeV correlation can be interpreted on the basis of a 3-2-2 and 4-2-2-spin sequence. If a spin of 4 is assumed for the 2.71 MeV level, then the values of the A_2 and A_4 coefficients are $A_2 = 0.0736$ and $A_4 = 0.00017$ for the case of the 1.17 MeV gamma ray being pure quadrupole. In order to obtain agreement with the measured correlation, a large admixture of octupole radiation is required. In the case of the 3-2-2-spin sequence, the coefficients are $A_2 = -0.093$ and $A_4 = -0.001$ for a multipolarity of the 1.17 MeV gamma ray of 99% quadrupole, 1% dipole. It is felt that the spin 3 interpretation is the most likely since quadrupole-dipole competition occurs frequently. Strong competition between quadrupole and octupole radiation would be more likely in the case of M2(E3) than E2(M3). This would require that the 2.71 MeV level be 4-, in which case the beta transition β_7 would be second forbidden and the log ft value would be much higher than 7.2. It should be noted that even with the spin 3 interpretation, the theoretical value of the A_4 coefficient is in disagreement with the measured value by 1.5 standard deviations.

It is necessary to conclude, therefore, that the 0.898 - 1.17 MeV correlation data contains a systematic error most probably due to residual interference from Compton-Compton adding. The magnitude of the theoretical A_4 coefficient (-0.001) is sufficiently small as to indicate that the measured value would be substantially altered by any interference. The much larger A_2 coefficient would not be as sensitive to any extraneous contribution to the correlation.

The fact that the 1.17 MeV gamma ray is almost pure quadrupole for this spin sequence requires that this level have even parity. In summary, the interpretation of 3+ for the spin and parity of the 2.71 MeV level is the most consistent with the angular correlation measurements together with the branching ratios of the beta and gamma de-excitation modes.

Since the 1.66 MeV level does not decay to the ground state, the spin of this level must be either 0 or greater than 2. The population of this level by the 1.06 MeV gamma ray corresponding to de-excitation of the 2.71 MeV level indicates that the assignment of spin zero is unlikely. The 1.01 - 1.06 MeV correlation was analyzed on the basis of spin sequences 3-3-2 and 3-4-2. Only the 3-4-2 spin sequence can account for this correlation and requires that the 1.06 MeV gamma ray be approximately 99.5% quadrupole and the 1.01 MeV gamma ray be approximately 97% quadrupole and 3% octupole. On the basis of these facts, a spin and parity of 4+ is proposed for the 1.66 MeV level.

The spins of the 2.71 MeV and 1.66 MeV levels are shown in brackets in the decay scheme. Although these values are consistent with the data, it is felt that they are not adequately proven. The possibility of residual interference in the sum coincidence data introduces an uncertainty in the interpretation of the data. In addition, in order to remove ambiguities of interpretation in the case of the 1.01 - 1.06 MeV correlation, only spin sequences which appear physically reasonable were considered.

On the basis of these spin and parity assignments and the systematics of log ft values in this region, the most likely degree of forbiddenness of the beta transitions observed is given in Table XI. Similarly the multipolarity of the gamma transitions identified is summarized in Table XII.

7.3 Interpretation of the Results

Some properties of the Ce^{142} nucleus may be understood within the context of the considerations outlined in Chapter I. It must be stressed that this interpretation is at best only semi-quantitative. Since the information about this nucleus in particular and about this mass region in general is not complete, perhaps this is all that is justified at this time. The (N,Z) configuration for Ce^{142} is (84,58) so that there are one pair of neutrons and four proton pairs outside the respective closed shells. In this discussion we will ignore any possible interaction between extra-core neutrons and protons. Sheline (69) has published a recent survey of nuclear deformations; from the systematics presented, it would appear that collective deformations do not occur until the neutron number exceeds 88. The transition from spherical to deformed nuclei is reflected rather dramatically in the level structures of ${}_{64}Gd^{152}_{88}$ and ${}_{62}Sm^{152}_{90}$ (70). The evidence suggests that the equilibrium shape of ${}_{58}Ce^{142}_{84}$ is spherical. Such an interpretation is consistent with the remarks of Belyaev (17) and Mottelson (15) and indicates that the stabilizing influence of the pairing correlation is greater than the polarization effects for this nucleus.

The magnitude of the pair binding for neutrons and protons, Δ_n and Δ_p respectively, can be estimated from the A = 142 mass

TABLE IX

Probable Character of La^{142} Beta Transitions

Beta Group	E_β(MeV)	Type
β_1	4.49	First-Forbidden **(Unique)**
β_2	3.85	First-Forbidden
β_3	2.98	First-Forbidden
β_4	2.31	First-Forbidden (Allowed)
β_5	2.11	First-Forbidden (Allowed)
β_6	1.98	Allowed (First-Forbidden)
β_7	1.79	First-Forbidden (Allowed)
β_8	1.23	Allowed (First-Forbidden)
β_9	0.87	Allowed

TABLE XII

Probable Character of Prominent La^{142} Gamma Transitions

E_γ (MeV)	Multipolarity	Type
0.645	Quadrupole	Electric
0.898	Dipole (Quadrupole)	Magnetic (Electric)
1.01	Quadrupole (Dipole)	Electric (Magnetic)
1.06	Quadrupole (Dipole)	Electric (Magnetic)
1.16	Quadrupole (Dipole)	Electric (Magnetic)
1.74	Dipole	(Magnetic)
1.91	Dipole	(Electric)
2.06	Dipole	(Magnetic)
2.41	Quadrupole	(Magnetic)
2.55	Dipole	(Electric)

systematics as presented by Dewdney (5) and from the deuteron stripping results of Fulmer et al (71). The separation between the odd-odd and even-even mass parabolas for a given even A isobaric system, ΔE_e, is the sum of the neutron and proton pairing energies.

$$\Delta E_e = \Delta_n + \Delta_p. \tag{1}$$

The odd-A masses also tend to lie on two slightly displaced parabolas. If the proton pairing energy is larger than the neutron pairing energy, the masses of the odd-neutron nuclides lie on the lower parabola, while if the neutron pairing energy is the larger, the odd-proton nuclides lie on the lower parabola. In this case the separation is

$$\Delta E_o = \Delta_p - \Delta_n \tag{2}$$

As pointed out by Dewdney (5), ΔE_o increases in the A = 90 and A = 142 region, indicating a reduction in neutron pairing energy with respect to proton pairing energy. For A = 142, his results give $\Delta E_e = 2.22 \pm 0.06$ MeV and for A = 143, $\Delta E_o = 0.479 \pm 0.02$. This leads from (1) and (2) to pairing energies of approximately $\Delta_p = 1.4$ and $\Delta_n = 0.87$ MeV.

As discussed by Cohen (72), the cross sections for (d,p) and (d,t) reactions are closely related to the U_j^2 and V_j^2 defined in Chapter I. The probability for the capture of a neutron with final state (j,m) is proportional to the probability that the orbital be unoccupied, ie. U_j^2. The investigations of Cohen lead to information about the position of the single-particle states $\mathcal{E}_j - \lambda$, and the distribution coefficients U_j^2 and V_j^2. From these values and the equation relating them to Δ given in Chapter I, Cohen obtains $\Delta_n = 0.72$ MeV. This value is reasonably consistent with the estimates based on the A = 142 and 143 mass systematics. Since it has been obtained from a specific study of this nucleus, the value of $\Delta_n =$ 0.72 MeV is probably more applicable to this discussion. This would imply that $\Delta_p \gtrsim 1.5$ to maintain consistency with the A = 142 mass data.

From these results, one can conclude that the energy gap for intrinsic neutron excitations is approximately 1.44 MeV, while that for proton excitations is approximately 3.00 MeV in Ce^{142}. It is therefore to be expected that most of the particle levels populated in the beta decay will correspond to intrinsic neutron excitations. Since Ce^{142} is apparently a spherical nucleus, a description of the particle motions based upon the shell-model orbitals is appropriate. Recently, Cohen (73) has published an extensive survey of the relative positions of the single-particle neutron states. Kisslinger and Sorensen (74) have also obtained evidence for the relative spacings of proton levels. The results for this region are indicated in Figure 44. The single-particle neutron states are based on the results for Ce^{141}.

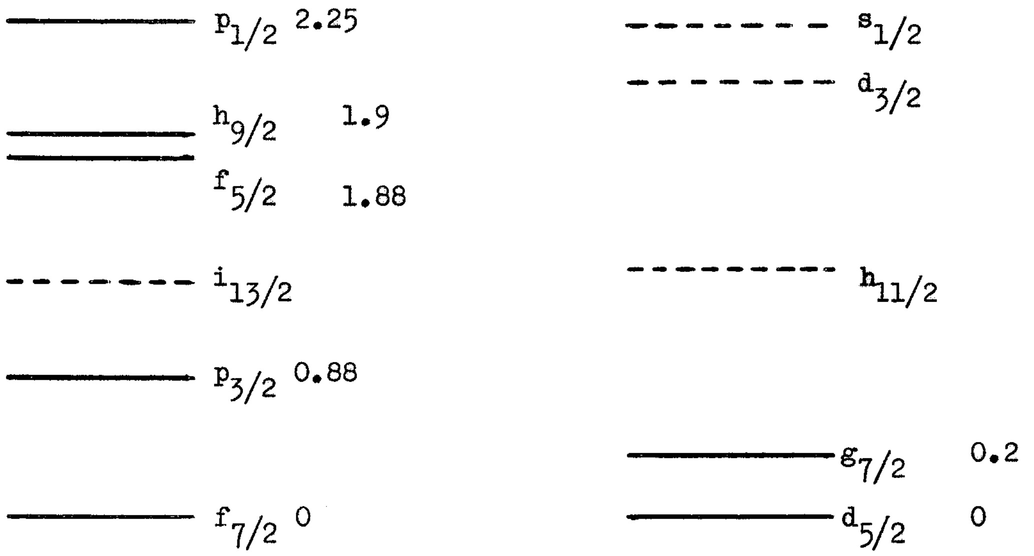

Neutron States (Ce^{141}) FIGURE 44 Proton States (Pr^{141})

There is no evidence on the $i_{13/2}$ state in this region. This state is predicted from the shell model to lie near the middle of the N = 82 and N = 126 closed shells. The only definite information on single-particle proton states is that the $g_{7/2}$ and $d_{5/2}$ states are closely spaced.

The residual interactions, in particular the pairing correlation, lead to considerable configuration mixing so that the actual nuclear states are distributed over the shell model states. Cohen (71) has determined the ground state wave function for Ce^{142} to be

$$(Ce^{142}) = (0.73)^{1/2} f^2_{7/2} + (0.11)^{1/2} p^2_{3/2} + (0.05)^{1/2} f^2_{5/2} + (0.017)^{1/2} p^2_{1/2} + (0.087)^{1/2} h^2_{9/2}$$

for the neutron configuration. The proton configuration might be expected to be an admixture of $(g_{7/2})$ and $d_{5/2}$ configurations. Because of the greater proton pair binding, it is felt that proton excitations will not play a significant role in the low-energy level structure. The intrinsic neutron excitations give rise to a level spectrum somewhat as indicated in Figure 45. The configurations designated as, for example, $f_{7/2}\ p_{3/2}$, indicate only the states with largest distribution coefficients V_j^2.

Of course, the actual energies of the intrinsic levels will be perturbed by the quadrupole interaction. In addition, when the vibrational energies $h\omega_2$ and $h\omega_3$ are of the same order as Δ_n, then the separation of collective and intrinsic motions is no longer a good approximation. The levels must be interpreted as hybridizations in which the collective levels are distributed over the intrinsic states.

FIGURE 45

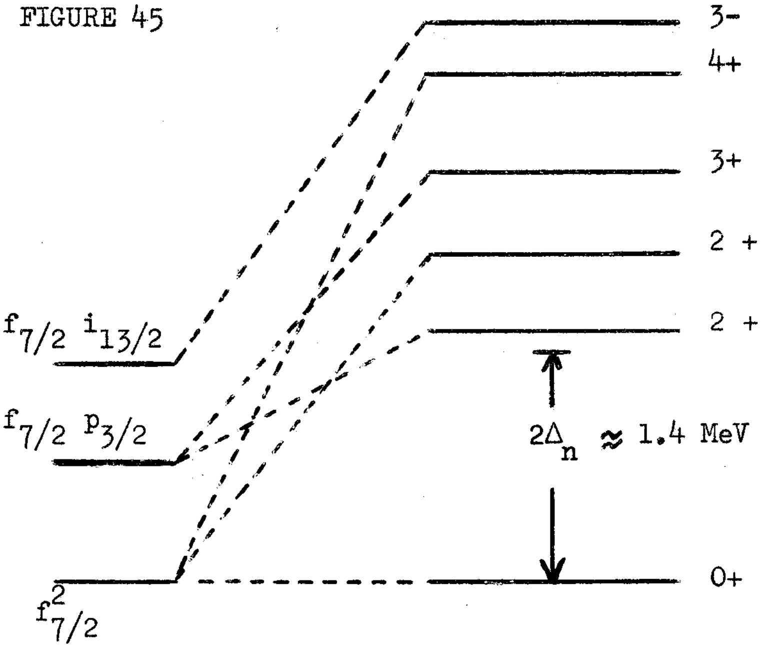

The 2^1+ state at 0.645 MeV can be interpreted as the one-phonon quadrupole vibrational state. This level appears well below the energy gap and can only correspond to a collective mode. Such an interpretation is confirmed by the Coulomb excitation results (75). These results show that the reduced matrix element $B(E2;2^1 \rightarrow 0)$ is enhanced by a factor of ten over the single-particle estimate which can be explained as arising from collective effects.

The second 2^2+ state at 1.54 MeV can possibly be connected with three distinct excitations; the two-phonon quadrupole vibration, the intrinsic excitation with configuration $(f_{7/2})^2$ in which the angular moment are coupled to a value of 2, or the $f_{7/2}\ p_{3/2}$ configuration, for which the lowest energy state is expected to be 2+. Some conclusions regarding the nature of this state may be drawn from its de-excitation properties. The angular correlation results indicate that the $2^2 \rightarrow 2^1$, 0.898 MeV transition is almost pure M1. The two-phonon state would de-excite primarily by an E2 transition. Coulomb excitation studies (68,75) have been carried out for incident energies sufficient to excite this level with negative results. It is therefore extremely likely that this level is different in intrinsic structure from the ground state. In terms of the shell-model orbitals, the M1 selection rule requires that the initial and final states have the same orbital angular momentum, while for E2 transitions, $\Delta l = 2$. If it is assumed that the 2^2-state is primarily $f_{7/2}\ p_{3/2}$, then the $2^2 \rightarrow 2^1$ transition arises mainly from the change in state of the $p_{3/2}$ neutron. The transition elements are outlined in the scheme shown in Figure 46. It is assumed that the intrinsic states for the collective level are the same as for the ground state

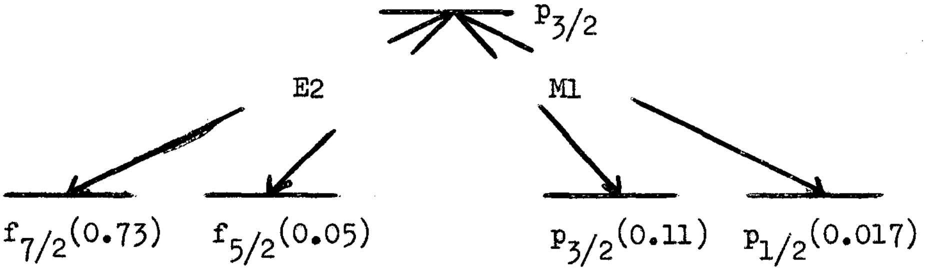

FIGURE 46

The mixing ratio is given approximately by

$$\delta^2 = \frac{(V^2_{7/2} + V^2_{5/2})}{(V^2_{5/2} + V^2_{1/2})}\ \frac{T_{sp}(E2)}{T_{sp}(M1)}$$

where T_{sp} are the single-particle transition probabilities. This equation gives a value of 0.009 compared to the single-particle estimate of 0.0015 and the collective estimate of 40-60. The measured value is 0.0064 ± 0.002. The systematics of M1-E2 mixing ratios for the $2^2 \rightarrow 2^1$ transitions has been reviewed recently by several authors (76,77,78). Potnis (78) observes that the mixing ratios lie near the collective estimates near the central regions between neutron closed shells and decrease rapidly towards the single-particle estimate at the closed shells. In this mass region the reduction in δ begins at approximately $N = 90$. This assumes significance when it is realized that this is the critical nucleon number at which spherical equilibrium becomes unstable. In the context of this discussion, it is interesting to attempt to explain the variation. It would appear that for the transition nuclei, the 2^2 level is a mixture of the 2-phonon state and an intrinsic state. The degree of hybridization increases with neutron number and the state changes from mainly particle structure near the closed-shell to mainly collective structure at the critical neutron number. The increase in δ with neutron number over the transition region could result from alterations in the V_j^2 as collective effects become more pronounced.

The ratio of reduced matrix elements for the 0.898-MeV and 1.54-MeV transitions can be calculated from the mixing ratios and relative intensities.

$$\frac{B(E2;2^2 \longrightarrow 2^1)}{B(E2;2^2 \longrightarrow 0)} = 0.38$$

On the very simple assumption that the 2^1 and ground state have the same intrinsic structure and that there are no collective matrix elements $2^2 \longrightarrow 2^1$, one would expect this ratio to be unity. In the extreme case of the 2^2 double phonon state, this ratio is infinite since $2^2 \longrightarrow 0$ is forbidden. The measured ratio appears to confirm the interpretation of the 2^2 state at 1.54 MeV as a predominantly intrinsic excitation mode with properties not unlike that of an $f_{7/2}\,p_{3/2}$ configuration. This interpretation, to be completely consistent, requires that the effective energy of the $p_{3/2}$ single-particle state be reduced to 0.41 MeV in Ce^{142} as compared to 0.88 MeV in Ce^{141}.

The situation surrounding the 1.66 MeV level is interesting. Quite recently the Coulomb excitation of this level was reported by Hansen and Nathan (73). These authors were unable to determine the angular correlation between the incident alpha-particles and the 1.01 MeV gamma ray and so could not give a definite spin assignment. They also performed experiments on several other nuclides throughout this region in which they could make definite spin assignments. The final states populated in this region were found to have spins of either 3 or 4, corresponding either to the one-phonon, 3-octupole vibration or the 2-phonon 4+ quadrupole vibration. On the basis of the energy systematics, they give a tentative assignment of 3- to this level. The angular correlation results of this study require that the spin be 4 and that the level be identified quite possibly as the second quadrupole vibrational state. Purely from considerations of spin and parity, this level could also be interpreted as an intrinsic excitation, probably resulting from a change in coupling of angular momenta in either the $(f_{7/2})^2$ or $f_{7/2}\ p_{3/2}$ configurations. On the other hand, the Coulomb excitation of this level can be considered as evidence that there is considerable collective structure in this state. With increasing energy, one would expect that the structure of the states could become relatively complicated. The vibrational energies are of the same order of magnitude as the particle energies so that the levels might display both collective and intrinsic properties to a varying degree. The only possible intrinsic structures that can explain the level with spin 1 at 2.55 MeV are the $f_{7/2}$ $f_{5/2}$ and $f_{7/2}$ $h_{9/2}$ configurations. Such an interpretation would require that the energy of either the $f_{5/2}$ or $h_{9/2}$ states be approximately 1.7 MeV as compared to 1.9 MeV in Ce^{141}, and that the parity of the 2.55 MeV state be positive. There is some evidence that the 3+ level at 2.71 MeV corresponds partly to the three-phonon quadrupole vibration, since it de-excites to the 1.54 MeV and 1.66 MeV levels by E2 radiation.

The ground-state spin for La^{142} of 2(-) is consistent with an ${f_{7/2}}_n$ ${d_{5/2}}_p$ configuration for the odd nucleons. The increased binding for pairs in higher angular momentum states would account for a reversal in the order of filling of the proton states $g_{7/2}$ and $d_{5/2}$ which are so closely spaced. The proton ground state configuration is probably $(g_{7/2})^6$ $d_{5/2}$. The $f_{7/2}$ $d_{5/2}$ configuration in Pr^{142} has as its lowest state the 2(-) configuration.

REFERENCES

1. V. F. Weisskopf, Phys. Rev. 83, 1073 (1951).

2. D. H. Wilkinson, Nuclear Spectroscopy, B, 852, Academic Press (1960).

3. L. C. Biedenharn, Nuclear Spectroscopy, B, 732, Academic Press (1960).

4. M. Ferentz and N. Rosenzweig, Table of F-Coefficients, Argonne National Laboratory Report ANL - 5234 (1953).

5. J. W. Dewdney, Nuclear Phys. 43, 303 (1963).

6. L. C. Gomes, J. D. Walecka and V. F. Weisskopf, Ann. Phys. 3, 241 (1958).

7. K. A. Brueckner and C. A. Levinson, Phys. Rev. 97, 1344 (1955).

8. K. A. Brueckner, A. M. Lockett and M. Rotenberg, Phys. Rev. 121, 255 (1961).

9. D. H. Wilkinson, Proc. Int. Conf. Nuclear Structure, 20, Univ. of Toronto Press (1960).

10. D. Pines, The Many-Body Problem, Benjamin Press (1961).

11. A. B. Migdal, Nuclear Phys. 13, 655 (1959).

12. J. Bardeen, L. N. Cooper and R. Schrieffer, Phys. Rev. 108, 1175 (1957).

13. A. Bohr, B. R. Mottelson and D. Pines, Phys. Rev. 110, 936 (1958).

14. G. Racah, Proc. Rehevoth Conf. Nuclear Structure, 155, North Holland Publishing Co. (1958).

15. B. R. Mottelson, Proc. Int. Conf. Nuclear Structure, 525, Univ. of Toronto Press (1960).

16. M. G. Mayer and J. H. D. Jensen, Elementary Theory of Nuclear Shell Structure, Wiley and Sons, Inc. (1955).

17. S. T. Belyaev, K. Danske Vidensk. Selsk. Mat.-fys. Medd. 31, No. 11 (1959).

18. G. E. Brown, J. A. Evans and D. J. Thouless, Nuclear Phys. 24, 1 (1961).

19. T. Huus, Proc. Scnd. Accelerator Conf. Amsterdam, 19, North Holland Publishing Co. (1960).

20. R. K. Sheline, Rev. Modern Phys. 32, 1 (1960).

21. O. Hahn and F. Strassmann, Naturwiss 30, 324 (1942).

22. S. Katcoff, Radiochemical Studies: The Fission Products, NNES9, 1147, McGraw-Hill (1951).

23. H. Ryde and C. J. Herrlander, Arkiv Fysik 13, 177 (1958).

24. R. P. Schuman, E. H. Turk and R. L. Heath, Phys. Rev. 115, 185 (1958).

25. K. Fritze and T. J. Kennett, Phys. Rev. 127, 1262 (1962).

26. M. G. Inghram, R. T. Hayden and D. C. Hess, Jr., Phys. Rev. 72, 967 (1947).

27. Nuclear Data Sheets, Mass 140, Nat. Acad. Sci., N.R.C. (U.S. Gov't. Printing Office, Washington, D.C.).

28. W. Riezler and G. Kauw, Z. Naturforsch 12a, 655 (1957).

29. W. H. Johnson, Jr. and A. O. Nier, Phys. Rev. 105, 1014 (1957).

30. R. Sher, J. Halpern and A. K. Mann, Phys. Rev. 84, 347 (1951).

31. A. Vanden Bosch, Physica 19, 374 (1953).

32. Nuclear Data Sheets, Mass 142, Nat. Acad. Sci., N.R.C. (U.S. Gov't. Printing Office, Washington, D.C.).

33. D. R. Nethaway, Thesis, Washington University, St. Louis (1959).

34. E. L. Bahn, Jr., Thesis, Washington University, St. Louis (1962).

35. H. Jung, P. H. Panussi and J. Jänecke, Nucl. Instr. and Meth. 9, 121 (1960).

36. P. R. Bell, R. C. Davis and W. Bernstein, Rev. Sci. Instr. 26, 726 (1955).

37. V. P. Guinn and J. E. Lasch, App. of Computers to Nuclear and Radiochemistry, NAS - NS - 3107, 243, Office of Tech. Services, Dept. of Commerce, Washington, D.C. (1962).

38. R. E. Bell, R. L. Graham and H. E. Petch, Can. J. Phys. 30, 35 (1950).

39. E. Fairstein, Rev. Sci. Instr. 27, 475 (1956).

40. R. L. Chase and V. Svelto, Brookhaven National Laboratory, BNL-5350 (1960).

41. E. Fairstein, T. A. Love and R. W. Peele, Proc. Sixth Tripartite Inst. Conf., Chalk River, AECL-804, 117 (1959).

42. R. L. Chase, Rev. Sci. Instr. 31, 945 (1960).

43. R. L. Heath, I. R. E. Trans. Nucl. Sci., NS-9(3), 294 (1962).

44. D. Engelkemeir, Rev. Sci. Instr. 27, 589 (1956).

45. W. C. Kaiser, I. R. E. Trans. Nucl. Sci., NS-9(3), 22 (1962).

46. R. W. Peele and T. A. Love, Appl. Nucl. Phys. Progress Report ORNL-2389, 249 (1957).

47. A. M. Hoogenboom, Nucl. Instr. and Meth. 3, 57 (1958).

48. J. E. Draper and A. A. Fleischer, Nucl. Instr. and Meth. 9, 67 (1960).

49. N. R. Johnson, E. Eichler, G. D. O'Kelley, J. W. Chase and J. T. Wasson, Phys. Rev. 122, 1546 (1961).

50. R. E. Segle, Bull. Am. Phys. Soc. 7, 48 (1962).

51. T. J. Kennett and G. L. Keech, To Be Published, Nucl. Instr. and Meth. (1963).

52. R. D. Birkhoff, Oak Ridge National Laboratory Report ORNL-2806, 153 (1959).

53. D. G. Maeder, Proc. Symp. on Advances in Fast-Pulse Techniques, UCRL-8706, 63 (1959).

54. C. D. Goodman, G. D. O'Kelley and D. A. Bromley, Proc. Symp. on Nucl. Instr. Harwell, Academic Press (1962).

55. G. D. O'Kelley, C. D. Goodman and D. A. Bromley, Oak Ridge National Laboratory Report ORNL-3176, 9 (1961).

56. L. Grodzins, Scnd. U.N. Int. Conf. Peaceful Uses of Atomic Energy, Geneva, 14, 351 (1958).

57. N. E. Scofield, App. of Computers to Nuclear and Radiochemistry, NAS-NS-3107, 108 (1962).

58. N. R. Johnson and G. D. O'Kelley, Phys. Rev. 108, 85 (1957).

59. M. S. Freedman, T. B. Novey, F. T. Porter and F. Wagner, Jr., Rev. Sci. Inst. 27, 716 (1956).

60. M. E. Rose, Phys. Rev. 91, 610 (1953).

61. J. S. Lauson, Jr. and H. Frauenfelder, Phys. Rev. 91, 649 (1953).

62. J. B. Marion, Nuclear Data Tables, Part 3, 72, Nat. Acad. Sci., N.R.C. (U.S. Gov't. Printing Office, Washington, D.C.) (1960).

63. R. L. Heath, Scintillation Spectrometry Gamma-Ray Spectrum Catalogue AEC Report IDO - 16408 (1957).

64. T. R. Gerholm, Arkiv für Fysik 11, 55 (1956).

65. Nuclear Data Group, N.A.S., N.R.C., Washington, D.C.

66. P. A. Seeger, Nuclear Phys. 25, 1 (1961).

67. A. G. W. Cameron, Can. J. Phys. 35, 1021 (1957).

68. O. Nathan and V. I. Popov, Nuclear Phys. 21, 631 (1960).

69. E. Marshalek, L. N. Person and R. K. Sheline, Revs. Mod. Phys. 35, 108 (1963).

70. J. Burde, A. Catz and S. Palti, Nuclear Phys. 44, 212 (1963).

71. R. H. Fulmer, A. L. McCarthy and B. L. Cohen, Phys. Rev. 128, 1302 (1962).

72. B. L. Cohen and R. E. Price, Phys. Rev. 121, 1441 (1961).

73. B. L. Cohen, R. H. Fulmer, A. L. McCarthy and P. Mukherjee, Revs. Mod. Phys. 35, 332 (1963).

74. L. S. Kisslinger and R. A. Sorensen, K. Danske Vidensk. Selsk. Mat.-fys. Medd. 32, 9 (1960).

75. O. Hansen and O. Nathan, Nuclear Phys. 42, 197 (1963).

76. D. M. Van Patter, Nuclear Phys. 14, 42 (1959).

77. D. P. Grechukhen, Nuclear Phys. 40, 422 (1963).

78. V. R. Potnis and G. N. Rao, Nuclear Phys. 42, 620 (1963).